2015

BIOCORROSION RATE AND MECHANISM OF METALLIC MAGNESIUM IN MODEL ARTERIAL ENVIRONMENTS

Patrick Bowen
pkbowen@mtu.edu

BIOCORROSION RATE AND MECHANISM OF METALLIC MAGNESIUM IN MODEL ARTERIAL ENVIRONMENTS

By

Patrick K. Bowen

A DISSERTATION

Submitted in partial fulfillment of the requirements for the degree of

DOCTOR OF PHILOSOPHY

In Materials Science and Engineering

MICHIGAN TECHNOLOGICAL UNIVERSITY

2015

This dissertation has been approved in partial fulfillment of the requirements for the Degree of DOCTOR OF PHILOSOPHY in Materials Science and Engineering.

Department of Materials Science and Engineering

Dissertation Advisor:	*Jaroslaw W. Drelich, Ph.D.*
Committee Member:	*Calvin L. White, Ph.D.*
Committee Member:	*Stephen A. Hackney, Ph.D.*
Committee Member:	*Jeremy Goldman, Ph.D.*
Committee Member:	*Feng Zhao, Ph.D.*
Department Chair:	*Stephen L. Kampe, Ph.D.*

This is dedicated to Lanora Schutz,

to the memory of Gale Schutz,

and to the memory of Ray and Emma Bowen.

Table of Contents

Preface

This doctoral thesis is a compendium of six articles that were accepted for publication in peer-reviewed journals between 2012 and 2015. They are organized into three over-arching, interdependent topics related to the arterial bioabsorption of magnesium. The full references for the six articles presented herein are listed below. Permission for reusing these previously published materials was granted by the publisher of each paper.

The majority of experimental work and nearly all writing were performed by Patrick K. Bowen with advice from Prof. Jaroslaw W. Drelich and Prof. Jeremy Goldman. Prof. Jeremy Goldman performed all animal implantations, sacrifices, and material retrieval operations. Contributions of co-authors unique to each article are stated below. Undergraduate researchers, staff, and colleagues who contributed to multiple projects are named in the Acknowledgements section. Individual acknowledgements are also included for each article immediately before the references.

1. P. K. Bowen, J. A. Gelbaugh, P. J. Mercier, J. Goldman, and J. Drelich. "Tensile testing as a novel method for quantitatively evaluating bioabsorbable material degradation." *J. Biomed. Mater. Res. Part B*, 100B(8) 2101-2113 (2012), doi: 10.1002/jbm.b.32775.

   The tensile testing technique was co-developed and proof-of-concept data acquired with Jesse A. Gelbaugh in 2010 and 2011. Further *in vitro* corrosion experiments were performed in 2011 by Phillip J. Mercier, who, at the time, was an undergraduate researcher.

2. P. K. Bowen, J. Drelich, R. E. Buxbaum, R. M. Rajachar, and J. Goldman. "New approaches in evaluating metallic candidates for bioabsorbable stents." *Emerging Mater. Res.* 1(5) 237-255 (2012), doi: 10.1680/emr.12.00017.

   This manuscript included results from a hot-rolled "A9" magnesium alloy provided by Robert E. Buxbaum, Ph.D. Calcium phosphate resorption data were courtesy of Prof. Rupak M. Rajachar. Prof. Jaroslaw W. Drelich also contributed written material to the introductory portion of this article.

3. P. K. Bowen, J. Drelich, and J. Goldman. "A new *in vitro-in vivo* correlation for bioabsorbable magnesium stents from mechanical behavior." *Mater. Sci. Eng. C* 33(8) 5064-5070 (2013), doi: 10.1016/j.msec.2013.08.042.

4. P. K. Bowen, A. Drelich, J. Drelich, and J. Goldman. "Rates of *in vivo* (arterial) and *in vitro* biocorrosion for pure magnesium." *J. Biomed. Mater. Res. A* 103(1) 341-349 (2015), doi: 10.1002/jbm.a.35179.

   Adam Drelich performed *in vitro* corrosion experiments and assisted in producing metallographic cross-sections for analysis in this study.

5. P. K. Bowen, J. Drelich, and J. Goldman. "Magnesium in the murine artery: probing the products of corrosion." *Acta Biomater.* 10(3) 1475-1483 (2014), doi: 10.1016/j.actbio.2013.11.021.

6. P. K. Bowen, C. T. McNamara, O. P. Mills, J. W. Drelich, and J. Goldman. “FIB-TEM study of magnesium corrosion products after 14 days in the murine artery.” *ACS Biomater. Sci. Eng.* 1(10) 919-926 (2015), doi: 10.1021/acsbiomaterials.5b00044.

   Cameron T. McNamara helped operate the TEM, interpret bright field, dark field, and SAED data, and infer MgO growth patterns. Owen P. Mills performed FIB liftout and foil thinning operations.

Acknowledgements

The research accomplishments presented in this dissertation, as well as those omitted from this document, would have been impossible without the patient guidance, encouragement, and ideas from Prof. Jaroslaw W. Drelich. The enthusiastic collaboration (and steady surgeon's hand) of Prof. Jeremy Goldman was also critical to this project's success.

My parents, Kim and Sandra Bowen; my sister, Mary Bowen; and my best friend and partner Emily Shearier have all supported me in innumerable ways during this long undertaking.

The Department of Materials Science and Engineering at Michigan Tech, the DeVlieg Foundation, and the American Heart Association are all acknowledged for providing financial support at various points. Boston Scientific Co. is also acknowledged for sponsoring the student project upon which this project nucleated.

Many friends and colleagues have contributed directly and indirectly to this dissertation. Some of the most important direct contributors over the last five years (in no particular order; some are co-authors, but others are not) have been Roger Guillory, Cam McNamara, Owen Mills, Jon Stinson, Jake Edick, Adam Drelich, Jacob Braykovich, Connor McCarthy, Jesse Gelbaugh, Shan Zhao, Boyi Hao, Phill Mercier, Mike Warhus, Mick Small, Felicia Nip, Paul Fraley, Matt Tianen, Jan Seitz, Jeff Brookins, Leslie

LaLonde, Nick Verhun, Jessica Rhadigan, Becky Franke, Ellen Pokorney, and Aaron Tauscher.

There are plenty of other students, staff, and faculty that did not necessarily contribute data or ideas to the material presented in this dissertation, but still had a large influence on my development as a researcher. To recognize some of those people, I'd like to thank Dr. Andrew Baker, Dr. Joe Licavoli, Dr. Dan Seguin, Helen Rau, Rafael Gil Figueroa, Prof. Stephen Kampe, Dr. Ashim Chakravarty, Dr. Wim Sillekens, Prof. Norbert Hort, Prof. Petra Maier, Dr. Ed Laitila, Dr. Moshe Einav, Prof. Tim Scarlett, and Sean Hopkins.

I would finally like to thank my committee members—Prof. Calvin White, Prof. Stephen Hackney, and Prof. Feng Zhao—for the time and mental energy spent helping to shape and evaluate my dissertation.

Abstract

A new paradigm in biomedical engineering calls for biologically active implants that are absorbed by the body over time. One popular application for this concept is in the engineering of endovascular stents that are delivered concurrently with balloon angioplasty. These devices enable the injured vessels to remain patent during healing, but are not needed for more than a few months after the procedure. Early studies of iron- and magnesium-based stents have concluded that magnesium is a potentially suitable base material for such a device; alloys can achieve acceptable mechanical properties and do not seem to harm the artery during degradation.

Research done up to the onset of research contained in this dissertation, for the most part, failed to define realistic physiological corrosion mechanisms, and failed to correlate degradation rates between *in vitro* and *in vivo* environments. Six previously published works form the basis of this dissertation. The topics of these papers include (1) a method by which tensile testing may be applied to evaluate biomaterial degradation; (2) a suite of approaches that can be used to screen candidate absorbable magnesium biomaterials; (3) *in vivo-in vitro* environmental correlations based on mechanical behavior; (4) a similar correlation on the basis of penetration rate; (5) a mid-to-late stage physiological corrosion mechanism for magnesium in an arterial environment; and (6) the identification of corrosion products in degradable magnesium using transmission electron microscopy.

Introduction

During a coronary angioplasty, a blocked vessel is widened by deploying a balloon within the artery by way of a catheter inserted in the femoral artery. In the United States, Western Europe, and increasingly in Asia, it is common to provide mechanical support for the wounded artery via a small, tube-shaped wire mesh, called a vascular stent. Up until now, stents have been designed to remain inert in the body. This corrosion resistance is intended to prevent catastrophic failure of the stent in the arterial wall, though a small minority of cases still experience late-stage complications that can require invasive surgery to correct. A new paradigm in biomaterials has recently emerged and shifted the focus to active materials, which react with the physiological environment, as opposed to the passive materials, which do not. The new generation of vascular stents will be absorbed and metabolized by the body after completing their task as vascular scaffolding. Because of this behavior, these materials are said to be bioabsorbable, bioresorbable, or biodegradable in nature.

The first bioabsorbable stents were made of degradable polymers such as poly-L-lactic acid (PLLA). Because of this, the field of bioabsorbable polymers is now quite advanced, with numerous candidates having completed limited clinical trials. However, the relatively low strengths of polymeric materials require quite large stent sizes, leading to either protrusion of the stent struts into the artery or increased vascular injury if the stents are pushed fully into the arterial wall.

Due to the challenges inherent to polymer stent engineering and deployment, metallic materials that can safely degrade in the physiological environment are desirable for this application. Most traditional biocompatible base metals, such as tantalum, titanium, niobium, etc. do not degrade at an appreciable rate in the body and thus would not be absorbed in a reasonable amount of time. Furthermore, such extraphysiological elements—those that do not play a well-defined biological role—would not be metabolized by the body, but would rather have to proceed directly to excretion. Conversely, elements that are already known to play physiological roles in the human body are generally biocompatible in their metallic forms and therefore are suitable materials for constructing bioabsorbable stents. Many biologically important materials, such as calcium or sodium, would degrade much too quickly (or violently) if placed in a physiological environment, and so the more reactive metals are not suitable. This exclusion is also based on the bioabsorption criterion. Magnesium (Mg), iron (Fe), and more recently zinc (Zn), have been proposed to hold promise for use in cardiac stents.

Fe-based materials were of special interest in the early days of bioabsorbable stents. Fe was not a suitable material *per se*, as it lasted much too long in the body to be absorbed in a reasonable amount of time. Researchers were ultimately successful in alloying efforts aimed at producing Fe-based materials with highly tunable degradation times. By this time, however, it was also found that Fe corrosion resulted in corrosion products that appeared to be neither metabolized nor excreted. This result ruled out the application of Fe-based bioabsorbable alloys in cardiac stents.

The previous results with iron and the dubious efficacy of polymeric stents and harmful degradation of Fe have led researchers in the direction of bioabsorbable Mg alloys. However, there remains a lack of understanding regarding the fundamental corrosion behavior of Mg in the physiological environment. Such an understanding is a crucial step to tailoring alloys with low rates of corrosion in the biological environment.

Some attempts have been made to clarify the mechanism that governs Mg degradation in a pseudophysiological environment and to identify the factors that distinguish *in vivo* corrosion from conventional Mg corrosion in simple salt solutions. In this instance, tests using a "real" system—the *in vivo* environment—are far superior to benchtop tests using simulated body fluids. To date, relatively few reports have been published on the behavior of materials *in vivo* in comparison to the body of literature that has grown on bioabsorbable cardiac stent materials corroded *in vitro*. This is largely because *in vivo* evaluations of interventional cardiology devices are more often conducted by industrial labs than by academic investigators, and involve large animals such as pigs.

Alternative murine and porcine arterial corrosion models have been used successfully in the past, including a so-called "wall implant" in the murine model that was developed at Michigan Tech. The advent of this technique provided a new tool with which degradable biometals could be evaluated with a higher number of replicates and/or time points.

Using results from this model as a benchmark, the development of complementary methods for *in vivo* and *in vitro* material testing, as well as quantitative treatment of corroded samples, became an early focus of research and is the focus of Chapter 1. It

was recognized early on that correlating *in vitro* and *in vivo* corrosion was crucial to predicting implant behavior, though early attempts using conventional electrochemical and immersion tests failed to produce a correlation. Using the *in vivo* and *in vitro* methods reviewed and developed in Chapter 1, corroded samples were evaluated mechanically and in cross-section in order to draw correlations between the two environments. As a result, Chapter 2 catalogues the pursuit of an *in vitro-in vivo* correlation. Despite the successful development a quantitative *in vitro-in vivo* corrosion correlations, portions of the *in vivo* mechanism of degradation remained a mystery. In Chapter 3 the focus is shifted to the development, composition, and physical structure of the corrosion products developed in the biological environment on pure Mg. The mechanisms uncovered in Chapter 3 enable a more advanced interpretation of the corrosion kinetics described in Chapter 2.

Chapter 1 Introduction

A method of evaluating bioabsorbable materials corroded *in vivo* and *in vitro* was desired which takes into account the material's strength in addition to large defects, cracks, and localized corrosion. Such a measurement would more-or-less reflect the implant's behavior in service. To meet this challenge, a method of mechanical evaluation based on tensile testing, which drew upon methods commonly used to evaluate polymeric nanofibers was developed. This technique, its strengths and weaknesses, and the proper interpretation of the mechanical data are discussed in detail in Section 1.1. This was the author's first foray into the bioabsorbable materials literature.

Following the publication of this analysis technique, a suite of *in vitro* and *in vivo* analysis methods are introduced in Section 1.2. This section is partially experimental and partially review-oriented. The experimental aspects involve both *in vitro* and *in vivo* methodologies, qualitative characterization, and quantification of material degradation through mechanical behavior. A thorough review of literature at the time of publication is also presented, in addition to an argument for a "suite" of degradation techniques based, in part, on the *in vivo* corrosion and tensile testing capabilities developed at Michigan Tech.

Chapter 2 Introduction

The development of an *in vivo-in vitro* corrosion rate relationship is a critical issue in absorbable biometals research and standardization. Extensive investigation with various *in vitro* methods has produced discordant quantitative results—such as corrosion rates—and animal studies are considered the "gold standard" to this day. If an alternative to animal-based methods could be devised and shown to have a consistent relationship with benchmark *in vivo* outcomes, the use of live subjects could be reduced or—to an extent—replaced. The first approach to deriving an *in vivo-in vitro* relationship, presented in Section 2.1, used the previously reported tensile testing method. Similar to the previously developed tensile testing technique, this study measured and correlated the actual, in-service mechanical properties of pure Mg over its degradation lifetime. While ultimately non-predictive, new insights were gained into the structural properties of

corroded Mg implants. The technique and correlation, properly applied, could theoretically predict in-service mechanical properties and structural component lifetimes.

As a follow-on to the results from the mechanical behavior study, Section 2.2 catalogues the process by which corrosion rates at various times were used as a metric by which comparisons between environments could be drawn. As opposed to focusing on the mechanical performance of the degrading material, this technique emphasized the amount of remaining material *in vivo* and *in vitro*. The results of these studies pointed to still more discrepancies between the two environments at different stages of corrosion.

Chapter 3 Introduction

Up until this point, discussion has been relatively engineering-oriented: how best to simulate and measure material degradation, how fast degradation occurs in various environments, and how to relate the kinetics of *in vivo* and *in vitro* corrosion. In Section 3.1, the focus is shifted to the development, composition, and physical structure of the corrosion products developed in the biological environment on pure Mg. Characterization of the *in vivo* degradation of Mg focused on the use of conventional methods of characterization to extract the maximum amount of information from the samples used in the study. Optical, electron, and infrared techniques were utilized, and shed light on possible surface modification and corrosion mechanisms at work *in vivo*.

The electron microscopy and infrared spectroscopy work in Section 3.1 yielded interesting new mechanistic insights, but was not capable of uncovering what product(s)

exist in the inner corrosion layer adjacent to the metallic Mg. The last experimental section in this document, Section 3.2, contains the details of a transmission electron microscopy-based study of this corrosion layer. The structure of the inner corrosion layer had implications for the mechanism of corrosion as well as mass transport during corrosion.

1 Corrosion and analysis method development

1.1 Tensile testing as a novel method for quantitatively evaluating bioabsorbable material degradation[1]

1.1.1 Abstract

Bioabsorbable metallic materials have become a topic of interest in the field of interventional cardiology because of their potential application in stents. A well-defined, quantitative method for evaluating the degradation rate of candidate materials is currently needed in this area. In this study, biodegradation of 0.25 mm iron and magnesium wires was simulated *in vitro* through immersion in cell culture medium with and without a fibrin coating (meant to imitate the neointima). The immersed samples were corroded under physiological conditions (37°C, 5% CO_2). Iron degraded in a highly localized manner, producing voluminous corrosion product while magnesium degraded more uniformly. To estimate the degradation rate in a quantitative manner, both raw and corroded samples underwent tensile testing using a protocol similar to that used on polymeric nanofibers. The effective ultimate tensile stress (tensile stress holding constant cross sectional area) was determined to be the mechanical metric that exhibited the

[1] The material in Section 1.1 was previously published in the *Journal of Biomedical Materials Research Part B* and is reproduced here with permission.

P. K. Bowen, J. A. Gelbaugh, P. J. Mercier, J. Goldman, and J. Drelich. "Tensile testing as a novel method for quantitatively evaluating bioabsorbable material degradation." *J. Biomed. Mater. Res. Part B*, 100B(8) 2101-2113 (2012), doi: 10.1002/jbm.b.32775.

References in Section 1.1 follow the *Journal of Biomedical Materials Research Part B* author guidelines.

smallest amount of variability. When the effective tensile stress data were aggregated, a statistically significant downward, linear trend in strength was observed in both materials (Fe and Mg) with and without the fibrin coating. It was also demonstrated that tensile testing is able to distinguish between the higher degradation rate of the bare wires and the lower degradation rate of the fibrin-coated wires with confidence.

1.1.2 Introduction

Coronary arteries frequently stenose due to progressive intimal hyperplasia during atherosclerosis. Narrowed arteries are commonly repaired by angioplasty in conjunction with stent deployment, in which the vessel is mechanically widened by the balloon and mechanically reinforced by the scaffold. Although stents provide requisite mechanical support—and in many newer stents there is short-term drug release from polymer coatings—they are no longer thought to be needed following reendothelialization and wall repair. Subsequent to the acute repair period, the foreign stent material may contribute to long-term complications such as chronic inflammation, late stage thrombosis, and vessel size mismatch [1]. Bioabsorbable stents hold potential as alternatives for vascular stabilization and repair that may circumvent many of the current, long-term health risks by dissolving after arterial stabilization [2,3]. A stent that retains its mechanical properties for approximately 6 months and is then harmlessly eliminated from the body may allow the vessel to heal and remodel without incurring the long-term complications seen with permanent implants [4].

Magnesium (Mg) and iron (Fe) hold promise as bioabsorbable materials due to their mechanical properties and biocompatibility [5,6,7,8]. However, Mg and many of its commercially available alloys prematurely corrode within 2-3 months following implantation [4] with an associated evolution of hydrogen gas [9] that has raised concerns of cytotoxicity and systemic toxicity [10]. Magnesium alloys containing rare earth elements, such as AE- and WE-series alloys [11], have become one focus in biocorrosion investigations. They have been found to exhibit reduced corrosion rates relative to other, more common magnesium alloys [12,13]. In contrast to Mg, Fe corrodes too slowly to be used by itself as a bioabsorbable stent material [14]. Current research efforts have concentrated on either accelerating or decelerating the corrosion rate of Fe and Mg, respectively. These goals are believed to be achievable through alloying, thermal treatment, chemical treatment, and/or coating of these metals. Unfortunately, the large number of potential Mg- and Fe-based alloys and hybrid materials and the time-consuming and costly evaluations that would be required to assess them have slowed progress in identifying viable bioabsorbable materials for vascular stents.

When evaluating a material for a bioabsorbable metal stent, it is important to determine the corrosion rate and acquire knowledge of the corrosion mechanism *in vivo*. The mechanisms and reaction kinetics depend on parameters including composition of the alloy, metallurgical treatments, surface treatment, composition of the interacting electrolytes, chemistry and biology of the environment, and the transport and metabolic phenomena associated with the reactants and the products of the corrosion reaction [15]. In order to screen and test various bioabsorbable material candidates for vascular stent

applications in a short time, the authors have recently developed a simple and cost-effective *in vivo* model. Using this method, candidate materials are formed into a wire of 0.2–0.3 mm diameter (similar to that of a deployable stent strut) and are then implanted into a rat artery lumen or artery wall [16]. This model allows for detailed investigations at the interface between the candidate metal and the arterial blood or wall matrix.

The authors have also developed an *in vitro* testing method in which Fe and Mg wires are encapsulated in a fibrin coating intended to mimic the tissue present in the vascular neointima during atherosclerosis and the scar tissue that envelops a deployed stent. Other wires are left bare to mimic the unencapsulated state early in implantation. The use of fibrin is advantageous in that it is a naturally occurring, highly cross-linked biopolymer that allows for diffusion of corrosion products similar to the tightly networked extracellular matrix of vascular tissue *in vivo*. Evaluation of explanted wires from the *in vivo* model will be presented in future contributions.

These corrosion protocols are useful in gathering observational data *in vivo* and *in vitro*, but inclusion of a quantitative test component is critical in both cases. A common, quantitative practice in the field is to submerge candidate materials in phosphate buffered saline or other physiological solutions (e.g. Dulbecco's Modified Eagle Medium (DMEM), Hank's solution, and simulated body fluid) and monitor the change in sample mass [17,18,19], current density (an electrochemical technique) [20,21], and/or hydrogen evolution [22]. Unfortunately, these *in vitro* testing methods are difficult or impossible to implement in evaluation of *in vivo* specimens. Mass loss methods generally do not yield

valid results, since explanted wires retain a significant amount of tissue [16]. Electrochemical and hydrogen techniques are nearly impossible to implement *in vivo* in their current forms. In addition, few contributions include a quantitative method for characterizing the mechanical properties of the bioabsorbable materials, even though stents are valued primarily for their mechanical stability during vascular repair.

A method of evaluating bioabsorbable materials corroded *in vivo* and *in vitro* is desired which takes into account the material's strength in addition to large defects, cracks, and localized corrosion. To meet this challenge, a method of mechanical evaluation based on tensile testing which draws upon methods commonly used to evaluate polymeric nanofibers [23] is developed and thoroughly analyzed in this contribution. The tensile testing of wires corroded using vascular implantation and by way of *in vitro* benchtop testing will allow us to quantify and directly compare the corrosion rates of candidate materials in various environments.

1.1.3 Materials and Methods

1.1.3.1 Materials and coating protocol

Iron and magnesium wires with a diameter of 0.25 mm (±10% per manufacturer's specification) and 99.9%+ purity (Goodfellow; Oakdale, PA) were cut into 30 mm pieces. Wires of each type underwent tensile strength tests before and after corrosion. Magnesium of this purity level was specified by the manufacturer to have a typical iron content of 100 ppm, which put it over the commonly accepted tolerance limit of 50 ppm [24].

To produce fibrin-coated wires, wires were placed in a homemade mold to which an unpolymerized fibrinogen-thrombin solution was injected. The mold is pictured in Figure 1.1, along with a schematic of the wire with fibrin encapsulation, showing the approximate distribution of fibrin on all sides. Fibrin was produced by combining fibrinogen and thrombin solutions, allowing the thrombin to crosslink the fibrinogen monomer and form a fibrin matrix. Thrombin (Sigma-Aldrich; St. Louis, MO) was dissolved in 40 mM $CaCl_2$ in a concentration of 2.5 U/mL to create the crosslinking solution. Fibrinogen (Sigma-Aldrich; St. Louis, MO) was dissolved in 0.9 wt% NaCl with gentle agitation on an incubated shaker table to produce a 100 mg/mL fibrinogen solution. The two solutions were mixed in equal volumes to yield a pre-polymerization solution with a concentration of 50 mg/mL fibrinogen.

The fibrinogen was pipetted over the wire in a mold, which was constructed to mimic the type of encapsulation that one would expect in a mammalian aorta, with a large amount of mock-tissue on three sides and a thin layer of mock-neointimal tissue on the side facing the fluid. The aluminum mold was covered with Parafilm to prevent adhesion of the fibrin to any machining marks or other features on the metallic surface. The wires were often somewhat bowed in the molds (Figure 1.1), which effectively shifted the wire position left-to-right, so the corresponding dimension is omitted on the Figure 1.1 schematic. The mold containing the wires and liquid fibrinogen-thrombin solution was placed in the incubator for at least one hour to allow sufficient time for cross-linking.

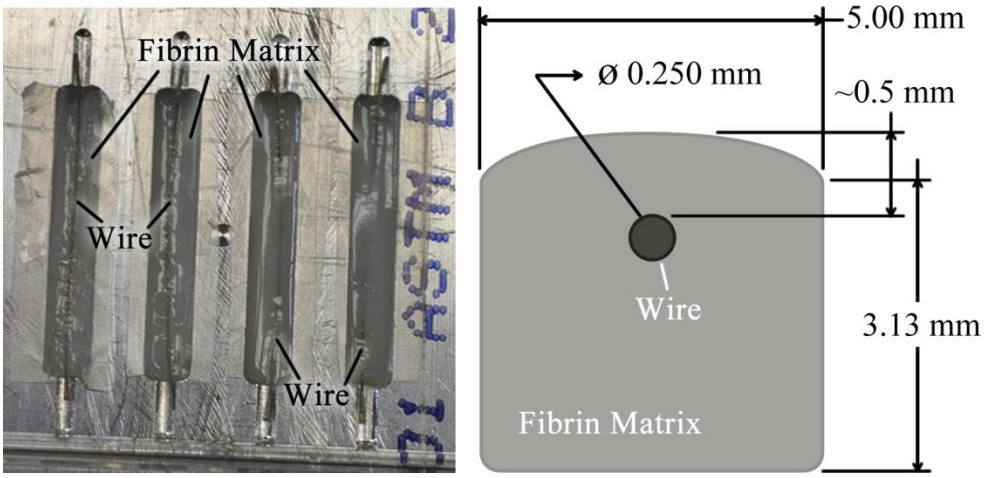

Figure 1.1 – Picture of the fibrin mold during the encapsulation process (left) and a dimensioned schematic of a wire after being encapsulated in a fibrin casting (right). The wire is often not perfectly centered in the fibrin, so that dimension is neglected on this schematic.

1.1.3.2 Corrosion protocol

Corrosion was carried out in DMEM (Invitrogen; Carlsbad, CA) under static conditions (wires were submerged in DMEM without stirring or pumping the fluid) on both bare wires and wires coated with fibrin. The former submersion method is termed "static bare wire testing" and the latter—the method which involved a fibrin coating—is termed "static coated wire testing." For magnesium, static bare wire testing was conducted for intervals of 1 to 10 days for a total of 12 samples, while static coated wire testing comprised samples corroded for 3.5 to 21 days for a total of 24 samples. For iron, static bare wire testing was conducted for 14 to 42 days for a total of 7 samples, while static coated wire testing had test intervals of 7 to 49 days for a total of 24 samples.

Submersion took place in six-well, sterile well plates (Becton Dickinson; Franklin Lakes, NJ), where the wires were covered with approximately 10 mL of DMEM (liquid volume

of approx. 5 mL). The well plates containing the encapsulated wires and DMEM were placed in an incubator at 37°C and 5% CO_2 atmosphere.

After corrosion testing, wires were removed from the DMEM and the fibrin coating was stripped off the wires. In the case of iron wires, the fibrin had to be removed mechanically with fine-tipped tweezers under a microscope due to a strong adhesion of fibrin to the wire surface. The samples were placed in fresh well plates in the low-humidity environment of a desiccator to prevent secondary oxidation or reaction with airborne moisture over time.

1.1.3.3 Sample imaging

Optical imaging was conducted with a Wild Heerbrugg M5a stereomicroscope using a Leica EC3 camera and bundled software (Leica Microsystems; Wetzlar, Germany). Images were acquired with low gain and high exposure times with white, vertical illumination and a small amount of oblique, yellow illumination on some samples to emphasize relief or luster.

Analysis of samples using scanning electron microscopy (SEM) was conducted with the JEOL JSM 6400 SEM (Peabody, MA) using 20 kV accelerating voltage for iron samples and 10 kV for magnesium samples. Elemental analysis was carried out with energy dispersive spectroscopy (EDS) using an Advanced Analysis Technologies X-ray detection system (Dane, Wisconsin). The X-ray information from the detector was

analyzed using Revolution X-ray Microanalysis software (4pi Analysis Inc.; Durham, NC). All scans were run with a dead time between 20% and 30% and a live time of 60 s.

1.1.3.4 Tensile stress testing

A schematic representation of the sample preparation protocol is shown in Figure 1.2. Before mounting, the end sections (~5 mm) of iron wires required roughening by 120-grit SiC sandpaper to improve their bonding to the epoxy and prevent sample pullout. Magnesium wires required no pretreatment due to their comparatively low strengths. Ends of all uncorroded wires were bent into a "D" shape to enhance the grip of the epoxy (Figure 1.3).

Bent wires were mounted on two pieces of roughened polycarbonate (PC) holders (30–40 mm wide × 60–80 mm long) placed approximately 10 mm apart to allow for a gauge section of that size (Figure 1.2). Stability and distance between PC holders was maintained by two toothpicks taped to them. The wire to be tested was mounted in between the toothpicks and each side of the wire was fixed with Loctite General Purpose epoxy (Henkel Corporation; Westlake, OH). Curing of epoxy was allowed for at least 24 h. Inadequate mixing of the two-part epoxy was the single most common mode of failure of this testing method, resulting in incompletely cured epoxy mounts.

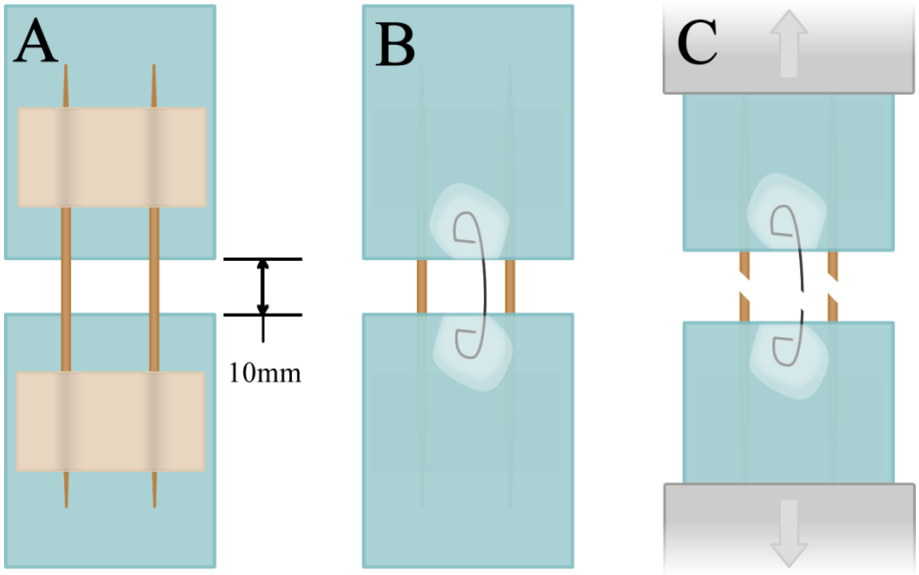

Figure 1.2 – Schematic representation of the tensile testing protocol. The PC substrate is separated by the size of the gauge section (10 mm) and secured with toothpicks and masking tape (A); the substrate is flipped over and the wire is affixed to the substrate with epoxy (B); and the sample is mounted, the toothpicks are cut, and the gauge section of the wire is loaded in tension (C).

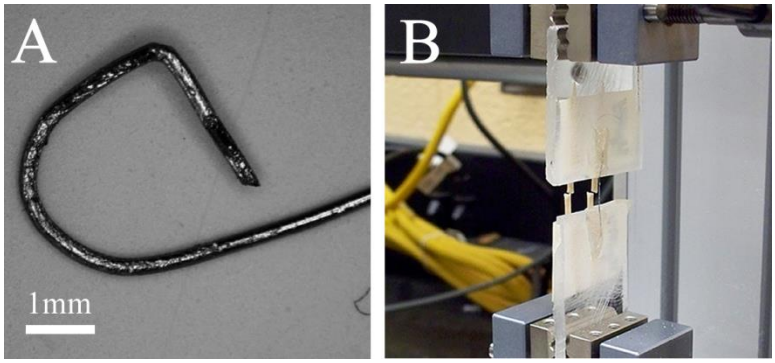

Figure 1.3 – Photographs taken of the samples during preparation and testing: A) the roughened, bent end of an uncorroded iron wire before epoxy encapsulation is presented and B) the mounted wire being loaded in tension with the masking tape and clipped supports visible on the reverse side.

After curing, the samples were tested using a Test Resources 100-Series Modular Test System (Shakopee, MN) equipped with a 250 lb_f (1.1 kN) load cell. The frame was

outfitted with soft tissue grips, which worked well for holding the two halves of the polycarbonate substrate. While loading the sample, the grips were aligned to ensure that the gauge section of the wire was well aligned with respect to the axis of motion. After the grips were hand-tightened, the toothpicks were cut cleanly in half [Figure 1.3(B)]. To avoid inadvertent breakage of heavily corroded samples, the two halves of the substrate were gently held in place while clipping the toothpicks. Tests were performed using a strain rate of 0.2 mm/min and ran until fracture.

Data exported from the Test Resources instrument was corrected for machine and epoxy compliance using a custom MATLAB script which allowed a user to select a linear portion of the load-elongation curve—corresponding to the linear-elastic region of the curve—and output a corrected load-elongation curve from which a stress-strain curve was calculated. Mechanical metrics including compliance, elastic modulus, yield stress, and tensile stress were calculated from the stress-strain curves.

1.1.4 Results and Discussion

1.1.4.1 Examination via optical microscopy

Corrosion was monitored during degradation, and several important observations were made regarding *in situ* sample behavior. No gas evolution was evident on the surface of the Fe wires, unlike the Mg wires which displayed obvious gas evolution consistent with the standard hydrogen reduction reaction [24]. On the Fe wires, the fibrin sheath typically began to degrade after approximately two weeks due to what the authors suspect is depolymerization and dissolution of the fibrin components. However, a coherent fibrin

layer remained on the Fe wires for as long as 7 weeks. The Mg wires' fibrin coating also began to degrade after about 14 days' time in the DMEM in the same apparent manner (dissolution). Near the end of the tests (3 weeks), only a fraction of a millimeter of fibrin typically remained intact on the wire surface. It has been shown by open-circuit potential measurements that corrosion is dominated (limited) by diffusion through the corrosion layer at times as early as two days in SBF [19]. Because of this, the authors expect long-term reduction in fibrin coverage to have little effect on the calculated degradation rates.

Post-corrosion optical examination of the wires revealed the type of corrosion that was predicted to occur in each system. In the iron system, it was observed—both visually and under the stereomicroscope—that highly localized corrosion was occurring at sites randomly distributed on the sample (Figure 1.4). While still submerged in DMEM, it was observed that voluminous corrosion products began to develop as early as one week into testing, while the rest of the wire remained relatively untouched. On closer inspection, the iron wire showed some signs of corrosion all over the wire surface [Figure 1.4(A)]. However, the dominant mode of corrosion was the localized corrosion, which was observed at various locations in all bare and coated samples at all time points. Examples of localized corrosion for two, four, and six-week tests are presented in Figure 1.4(B), (C), and (D), respectively. All of these had a "ball" of voluminous, orange product which, when removed, revealed a region of severe corrosion where the diameter was significantly reduced from 0.25 mm to nearly zero in some samples.

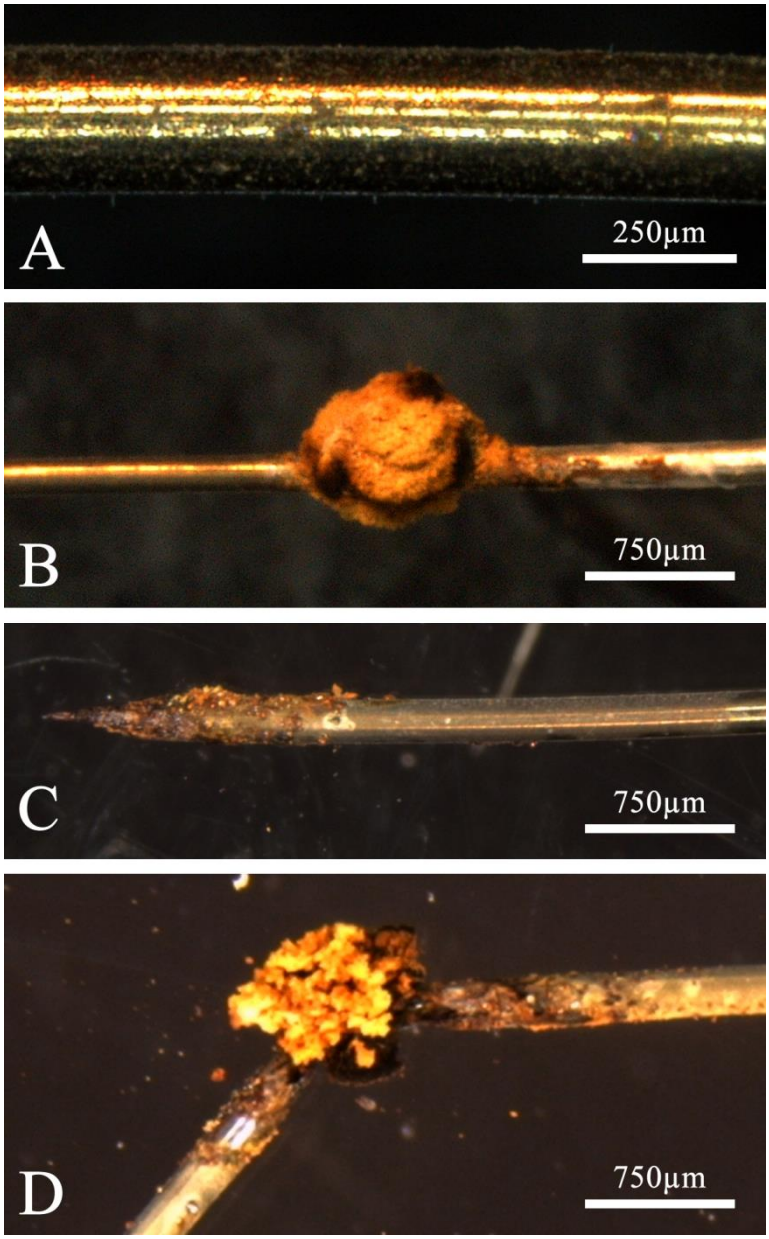

Figure 1.4 - Progression of bare iron wire corrosion in DMEM. Shown, in order, are a close-up of a typical section of an iron wire after 2 weeks showing minor pitting (A); a ball of voluminous corrosion product observed on an iron wire after 2 weeks, under which the cross section is reduced significantly (B); at the former site of a voluminous corrosion product, an iron wire was corroded completely through after 4 weeks (C); and corrosion product hiding a site at which the wire is nearly corroded through after 6 weeks (D).

Magnesium wires, on the other hand, exhibited very little to no localized corrosion and showed no evidence of voluminous product evolution. Instead, the progression appeared to be very clear and controlled over the material's corrosion lifecycle (Figure 1.5). At the earliest stages, usually in the first day of submersion, the magnesium developed a dark gray layer, which eventually evolved to a white/brown product that covered its silvery, metallic interior. The wires consistently displayed a thick layer of white corrosion product on the fracture face after prolonged corrosion. This progression from gray to blue to white dominant products was consistent between wires as well as between methods, although only micrographs of uncoated wires are presented in this communication.

The corrosion sequence observed in magnesium wires followed a well-defined, reaction-controlled corrosion mechanism which predictably reduced the cross sectional area of the material. This is in contrast to the iron corrosion observations which comprised pseudo-random evolution of patches of voluminous corrosion and associated localized reductions in the cross sectional area. These differences in corrosion inferred from stereomicroscopy are supported by the tensile testing data discussed later.

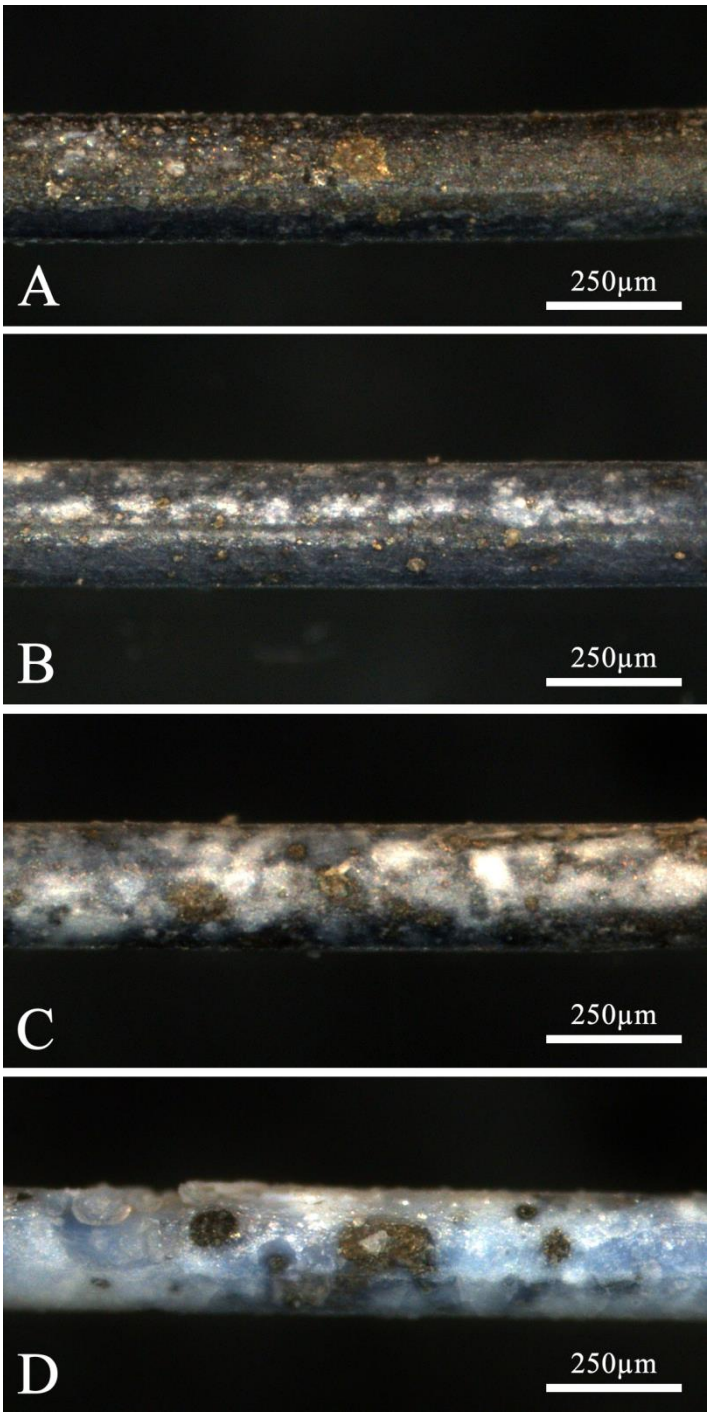

Figure 1.5 – Progression of bare magnesium corrosion through examination of typical corroded surfaces after 1 day (A), 2 days (B), 6 days (C), and 10 days (D) in DMEM.

1.1.4.2 Examination via scanning electron microscopy

Iron and magnesium wires' fracture surfaces were examined by scanning electron microscopy to evaluate their approximate morphologies and draw conclusions about their fracture behavior ex post. Images of two different iron wires are presented in Figure 1.6. The first iron wire [Figure 1.6 (A) and (B)] is an example of a wire that experienced significant, localized corrosion in its gauge section such as that presented in Figure 1.4, and so it fractured at that site. From the overview in Figure 1.6(A), one can see that the wire experienced a large reduction in cross sectional area at the local corrosion site, relative to the unharmed wire at the top of the micrograph. On the fracture surface close-up in Figure 1.6(B), it is apparent that the fracture surfaces has rounded edges and elongated, dimple-like features that indicate somewhat ductile behavior.

A different iron sample is pictured in Figure 1.6(C) and (D), which also failed at a site of localized corrosion. This sample was well suited for imaging the fracture surface and is representative of other iron wires. This particular specimen fractured near the epoxy, but failure did not appear to be initiated by it, as the fracture surface lies above the plane of the sample mount. A SEM image of the wire in Figure 1.6(C) shows the relatively uniform distribution of fracture features over the surface of the wire as well as the epoxy surrounding the wire.

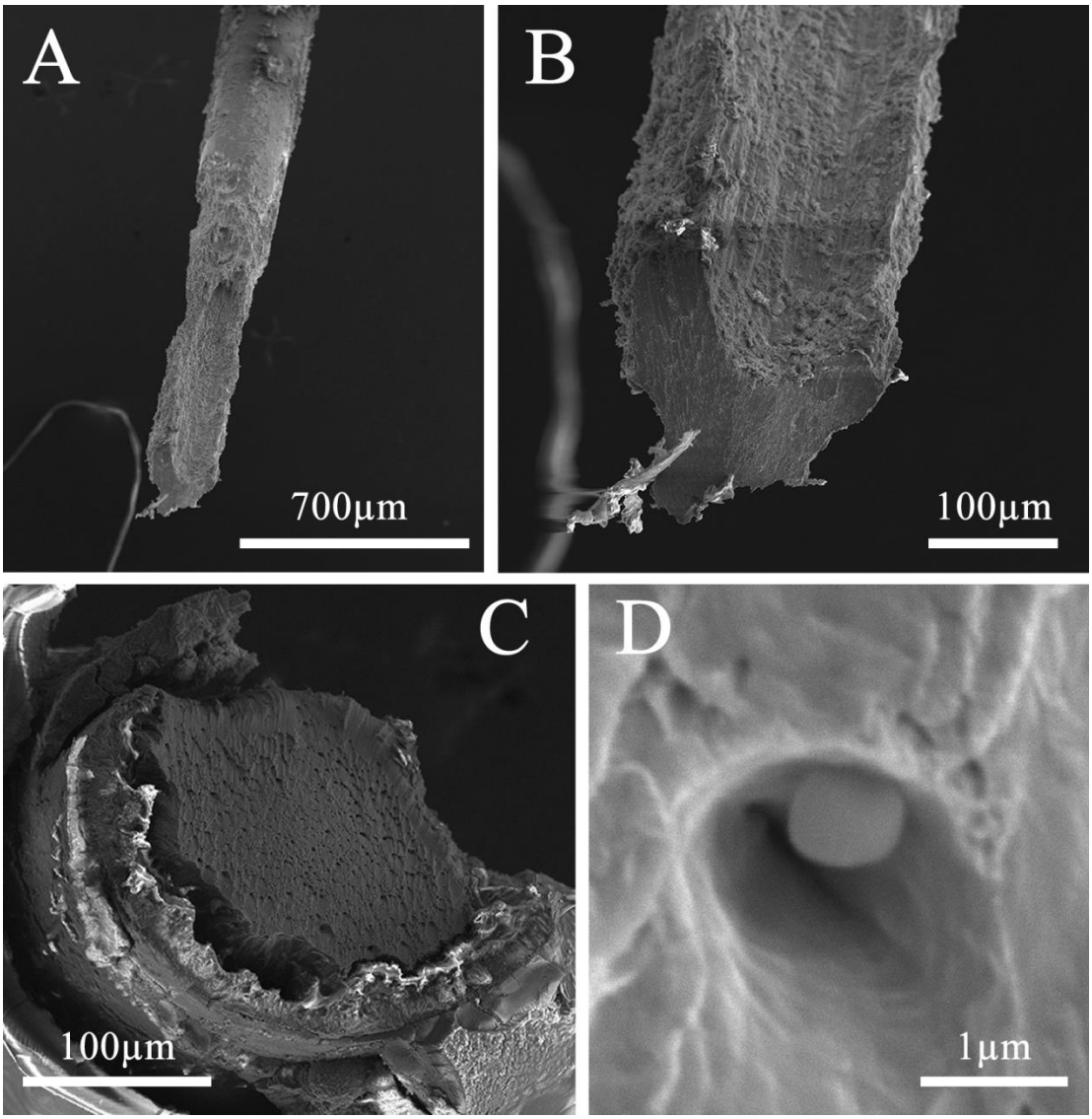

Figure 1.6 – Secondary electron images of Fe fracture surfaces. Sites examined included fracture at the site of localized corrosion (A); a close-up view of (A) showing evidence of plastic deformation (B); a top-down view of a different fracture surface which is surrounded by epoxy (C); and one of many dust particles that were visible at the bottom of the dimples on the fracture surface presented in (C) at 25,000× nominal magnification (D).

High-magnification imaging revealed that the features on the fracture surface were occupied by particles of various sizes, one of which is presented in Figure 1.6(D). This particular particle is clinging to the wall of a conical feature, while others were firmly

embedded in the bottom of the features. This leads to the conclusion that failure of the pure iron is dominated by microvoid nucleation and coalescence [25], a ductile failure mechanism where microvoids nucleate on micro- or nanoparticle (dust and/or refractory) inclusions and grow until they begin to interact and coalesce, ultimately leading to rupture.

EDS analysis performed on the surface of the severely corroded region of an iron wire indicated that the product was composed primarily of iron and oxygen with small amounts of several physiological elements (i.e. sodium, chlorine, etc.). This result is consistent with the optical observations in that there is discoloration and significant pitting, but there is not a large amount of coherent corrosion product buildup. The identification of the corrosion product as an iron oxide is also consistent with previously published data [16].

Similar images were prepared of magnesium wire corroded *in vitro*, which are presented in Figure 1.7. The optical image in Figure 1.7(A) shows the bright magnesium wire core surrounded by relatively dark corrosion product. A secondary electron image showing the magnesium fracture surface is presented in Figure 1.7(B), and it has characteristics very different from the iron wire's fracture surface in Figure 1.6(B). Primarily, the magnesium wire is surrounded by a thick layer of corrosion product, which appears as a bright area surrounding the dark Mg core—the layer is bright because it is charging in the SEM. The corrosion product layer was typically thicker on one side than on the other in samples that were coated with fibrin. This asymmetry in corrosion was likely due to

differences in mass transport rates between the media and thinly coated side and heavily coated sides of the wires. More discussion on this phenomenon will be presented in future contributions. Secondly, there appear to be some microvoid-like structures, but the fracture surface presented in Figure 1.6 has no well-defined voids or other periodic surface features. This relatively disordered fracture behavior was characteristic of the magnesium samples, and so they were not assigned a particular fracture mechanism. However, many samples did exhibit striations radiating from a point at the metal-corrosion product interface [Figure 1.7(C)], indicating that failure was initiated at this boundary in several cases.

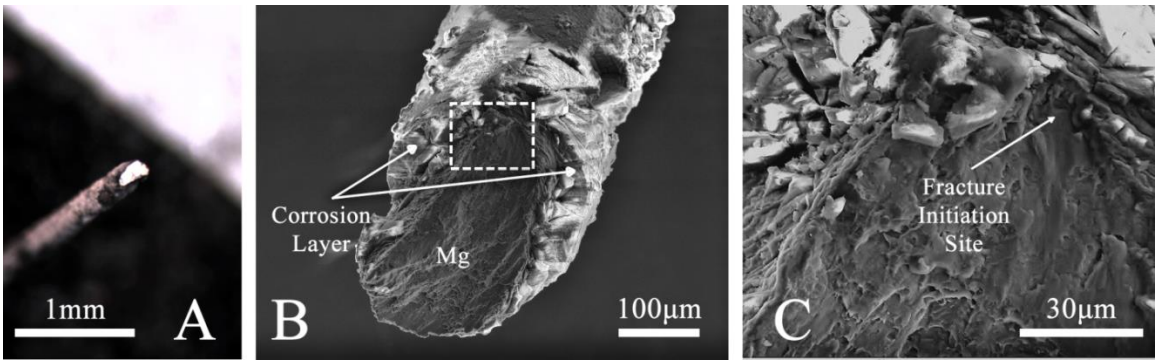

Figure 1.7– Optical and secondary electron images of magnesium fracture surfaces. The stereomicroscopic image of the fracture surface of a corroded magnesium wire (A) shows contrast between the lustrous magnesium core and the dull corrosion products. An SEI of the same fracture surface (B) showed relatively dark magnesium core surrounded by a bright (charging) corrosion layer. A close-up view (C) of the same wire (field of view marked by the dashed box in (B)) shows the suspected fracture initiation site.

EDS of the external corrosion layer on several different magnesium samples showed that the elemental makeup of the product was Mg, Ca, P, O, and trace physiological elements. This preliminary identification as a Mg/Ca phosphate (possibly mixed with a carbonate

due to the presence of a substantial carbon peak) is in good agreement with elemental analyses presented in the literature for similar experiments [26,27,14].

1.1.4.3 Mechanical testing results

1.1.4.3.1 Selection of mechanical metric

Early tests on iron and magnesium wires were compiled and various mechanical metrics compared for intersample repeatability. The purpose was to establish a basis for comparison between samples corroded for different amounts of time or by different methods. The mechanical metric should show the smallest variability possible between data that lay at the same time point. Mechanical properties that were considered included compliance, elastic modulus (Young's modulus), 0.2% offset yield stress, and ultimate tensile stress. To estimate the spread of the data for different mechanical properties, "raw" (uncorroded) wires (9 Fe and 6 Mg wires) were mechanically tested and each metric's standard deviation was taken as a fraction of the average metric value. The resulting sample standard deviation-to-mean ratios are presented in Table 1.1. It should be noted that this simple estimation requires an assumption of normality; different measures of spread may be applicable if one were to assume a different distribution such as those of a Weibull, gamma, or log-normal nature [28].

The compliance and elastic modulus showed identical spread (Table 1.1). Under the working assumption of constant cross-sectional area, the compliance and elastic modulus must consistently vary by only a simple ratio. Because of the constant area assumption,

the tensile strength was no longer truly representative of the wire being tested, but was rather relative to the nominal tensile strength of the wire. It will henceforth be referred to as the "effective tensile strength" to remind the reader that it is supposed to have precisely the same cross-sectional area as the as-received wire. The assumption of constant cross sectional area allowed for indirect measurement of the sample's effective cross sectional area at its weakest point: a critical consideration for applied bioabsorbable materials.

Table 1.1 – Comparison of variability in candidate mechanical metrics. *n* denotes the number of samples tested.

	Metric	**Iron** (n = 9)	**Magnesium** (n = 6)
St. Dev. / Mean	Compliance (N/mm)	0.134	0.328
	Elastic Modulus (GPa)	0.134	0.328
	0.2% Offset Yield Stress (MPa)	0.202	0.080
	Tensile Stress ≡ Effective Tensile Stress† (MPa)	0.103	0.075

† The ultimate tensile stress and effective tensile stress are equivalent here, as only uncorroded wires were examined.

Bearing that assumption in mind, the effective tensile strengths of the samples showed a much smaller variability (smaller standard deviation) from sample-to-sample in raw iron than did the elastic moduli or effective 0.2% offset stress values (Table 1.1). In magnesium, the yield stress and tensile strength spreads were virtually identical; there was no apparent advantage to using one metric over another. These data led to the selection of effective tensile strength as the mechanical metric of choice in this study.

1.1.4.3.2 Qualitative evaluation of tensile data

The iron and magnesium wires yielded vastly different tensile curves after the postprocessed data were plotted (Figure 1.8). Some early experiments with raw iron resulted in samples which had improperly cured epoxy. The uncured samples tended to exhibit a tensile form similar to soft thermoplastics [29], and thus were easy to distinguish from the typical iron wire form presented in Figure 1.8. These samples did not yield valid data and the results were therefore discarded.

The form of the raw iron tensile curve is what one would expect for a moderately hard material: it begins with elastic deformation, passes through a clear proportional limit and reaches a 0.2% offset yield point, but does not actually go through necking and the subsequent stress concentration. Instead, the hard material simply fractures at some point during plastic deformation. In Figure 1.8, the raw iron curve exhibits small "jumps" in the wire stress. The reason for this is likely interfacial slippage with the epoxy as the wire begins to contract radially, pulling away from the epoxy and effectively increasing the gauge length. A relatively strong material like cold-worked iron will always exhibit these types of problems, but one could easily correct for the added material by measuring the sudden drop in stress and estimating the corresponding increase in length. For purposes of analyzing the effective tensile strength of a sample, these jumps do not introduce any error, nor do they affect the measurement or calculation of stress. However, if one were interested in sample ductility or total elongation, a correction

would have to be performed. In testing, these jumps in stress are typically accompanied by audible "popping" noises emanating from the epoxy.

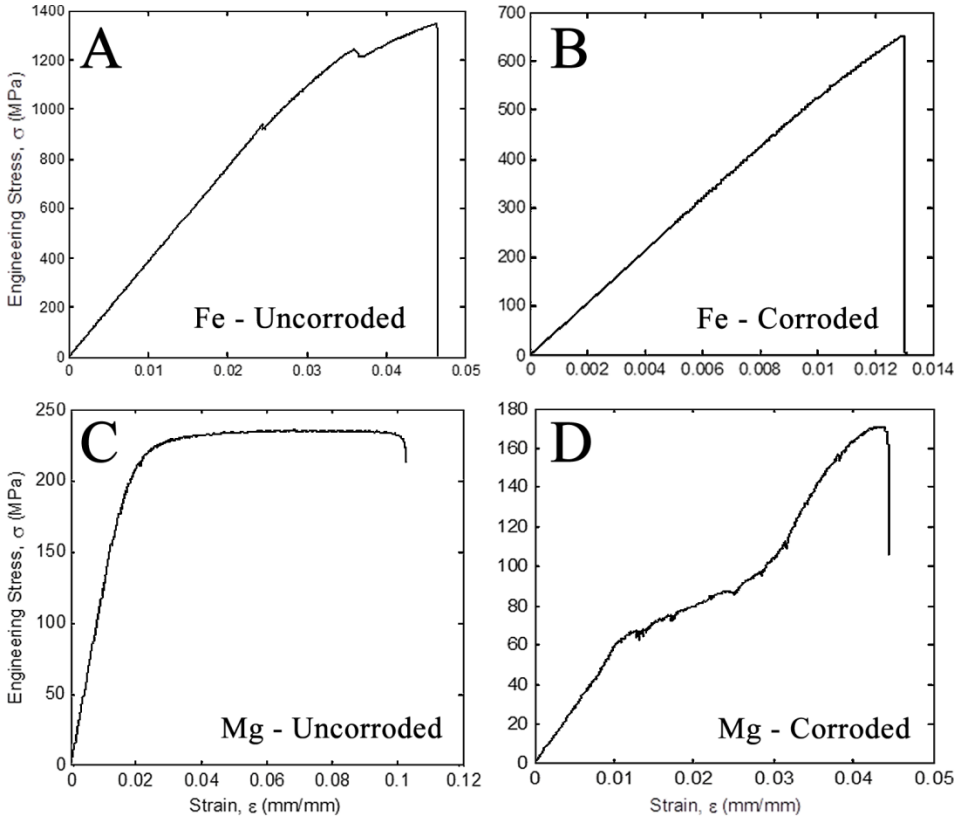

Figure 1.8 – Tensile curves characteristic of the materials examined in this study: raw iron (A); bare iron corroded for 6 weeks, which barely passes through its proportional limit before fracturing (B); raw magnesium (C); and coated magnesium corroded for 3 weeks, which has characteristics similar to brittle matrix composites evaluated in tension (D). Note the difference in scale (axes) in each plot.

The effect of corrosion on the shape of the iron tensile curve is roughly to "truncate" the tensile curve of the raw sample. This effect is observed because the natural tendency of iron in this environment is to corrode locally. When this localized corrosion occurs, the remaining iron at the corrosion site acts as a stress concentrator due to the local reduction in cross sectional area. In the case of especially intense local corrosion, the corroded area

can experience elastic deformation, plastic deformation, necking, and fracture all before the rest of the material in the gauge section even begins to deform plastically. This phenomenon can be observed by contrasting the corroded iron tensile curve in Figure 1.8, in which the sample barely passes through its proportional limit, with the observed plasticity in the highly corroded wire's fracture surface presented in Figure 1.6(B).

The raw tensile curve of magnesium was characterized by a linear-elastic region and clear transition to an extended region of plastic deformation (Figure 1.8). The magnesium exhibited relatively high ductility partially due to its small size, which limited the maximum flaw size in the material. An interesting change in the shape of the tensile curves of magnesium occurred after significant corrosion. Instead of stress concentration causing "truncation" like in the iron tensile curve, the magnesium becomes divided into two clear regions: (1) a steadily increasing, but choppy region at lower stress values, and (2) a rapidly increasing region which appears to be somewhat similar to the raw magnesium curve, which reaches the sample's effective tensile stress before fracturing. It is possible a growing corrosion layer on the exterior of the magnesium wire, such as that observed in Figure 1.5, resulted in mechanical behavior akin to a brittle matrix composite, in which the brittle material cracks until only the ductile reinforcement is bearing the load [30].

1.1.4.3.3 Compiled effective tensile stress data

After the compilation and analysis of tensile data for both uncoated and coated magnesium and iron wires, it was clear that the two materials and two treatments had

significantly different corrosion characteristics in the submersion tests. The effective tensile strengths of the two materials pointed to the following fact: the magnesium trended consistently downward with respect to corrosion time with relatively tight grouping of sample strength; the iron, on the other hand, had a large amount of scatter, but also trended generally downward. Figure 1.9 presents individual sample strengths as a function of immersion time (Mg at top left and Fe at bottom left) as well as averaged values and associated errors for each time point (Mg at top right and Fe at bottom right). After compilation and plotting, the appropriate statistical treatments were applied to these data.

1.1.4.3.4 Statistical nature of the data

The effective tensile stresses at various immersion times are plotted in Figure 1.9 in two different presentations: one set of graphs presents all experimental data (left side) and the second one shows calculated average values, combined with standard deviations as error bars (right side). The use of average values in calculations of significance was avoided for a simple reason: in corrosion testing, especially for nonuniformly corroding materials such as iron, observation of a normal distribution is not expected at each time point. Indeed, it is difficult to assign any distribution to these data with confidence. Therefore, each, individual piece of data was treated as independent from others, even those corroded in a similar manner for the same amount of time. Such a treatment preserved the statistical validity and robustness of any trend-based analyses that would otherwise be biased by reducing each time point's constituent data to a single point. A supplementary argument to support this assumption of independence is as follows: some iron samples

corroded severely at certain points and others experienced virtually no corrosion, which points to a naturally independent process, and therefore the process should be treated as independent in any attempt at statistical evaluation.

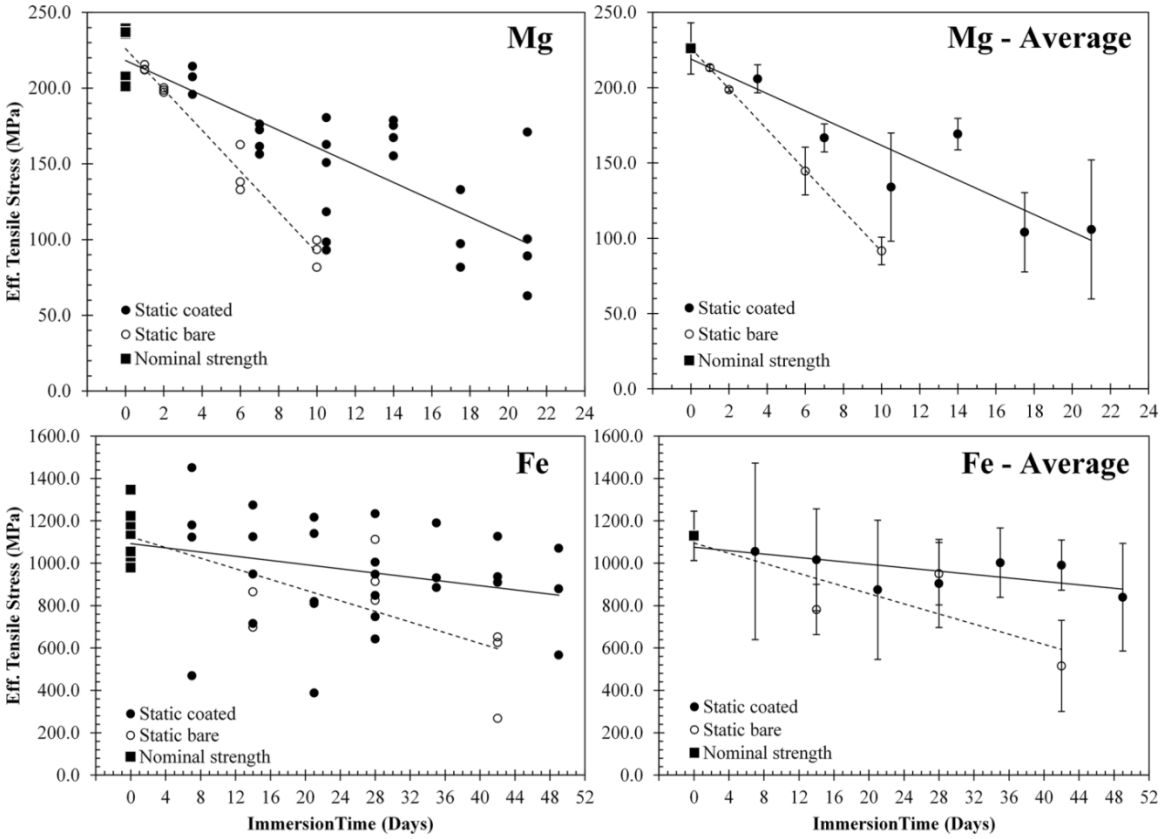

Figure 1.9 – All data for the effective tensile strengths of magnesium (top left) and iron (bottom left) "raw" (uncorroded) wires (■), static bare wires (○), and static coated wires (●). The data have associated regression lines, which include the nominal wire strengths: solid for static coated and dashed for static bare, respectively. The tensile data have also been averaged per time point, and are presented with error bars corresponding to one standard deviation for magnesium (top right) and iron (bottom right).

Regarding the above considerations of independence and non-uniformity, the issue of statistical outliers must be addressed. By simply examining the raw data presented in

Figure 1.9, one may reach the conclusion that some of the points should be disregarded, as they appear to be outliers relative to other samples that occupy the same time point. This may be true of a data set in which samples are expected to conform to a mean value (say, in testing the strength of "raw", or uncorroded, wires). However, testing for outliers in such a data set as that for corroded iron, which (as was argued before) comprises data points that are independent by their very nature, is a frivolous activity. It would work to improve the appearance of the trend, but would skew the results toward the wires that did not experience severe corrosion. Skewing of these data would have startling implications if this mechanical evaluation method were applied to real candidate materials: the estimated lifespan of a biomedical implant could be grossly overestimated leading to improper application and, consequently, sub-par performance of the implanted item. Because of these reasons, no data were eliminated simply because they appeared to be statistical outliers relative to other values in the same time period.

Very few data were discarded in this study. One of the main reasons data were discarded was a tensile curve that gave the authors a reason to believe the epoxy had not cured properly. On other occasions, the wire debonded from the epoxy before fracture (a common problem when testing iron). Rarely, fracture of uncorroded iron was initiated by the mounting epoxy resulting in lower-than-expected strengths and fracture that occurred exactly flush with the epoxy surface; these data were deemed invalid and rejected. Data were also discarded if the corresponding samples had broken before they were successfully tested, which sometimes occurred when attempting to test highly corroded magnesium at immersion times of approximately four weeks or more. On occasion, iron

corroded very severely at times as early as 2 weeks in uncoated trials, which resulted in wires like that presented in Figure 1.4(C) that exhibited through-thickness corrosion. It is possible that the exclusion of the most highly corroded samples for lack of test results resulted in lower-than-actual degradation rate estimates for both materials, though the effect is probably much larger for iron. In practice, the linear trend discussed in the next section may be considered to break down when spontaneous fracture begins to occur before or during testing.

Epoxy curing, cutting of the toothpicks before testing, and curving the wire ends have all been suggested as possible sources of error. These particular issues are of little consequence in practice. Consider the data for bare magnesium corrosion and the low associated error. The uniform nature of corrosion on the bare magnesium samples coupled with the high degree of reproducibility of the tensile testing methodology resulted in almost no error, especially at early time points. Hence, for a seasoned user of this technique, the error inherent to the method can be minimized to the point where it causes the measured values to fluctuate no more than 1-2%.

1.1.4.3.5 Comparison of corrosion rates in Mg and Fe

The tensile testing results were evaluated statistically through use of a simple regression analysis and a test for significant differences in the slopes. Though a more complex time dependence of the effective tensile strength was initially suspected to exist, the data prompted the choice of a linear model to describe the corrosion progression. Nonlinear models might be appropriate in trying to describe both *in vitro* and *in vivo* degradation

behavior, and will be considered in future work when effective strengths are available for a broader range of degradation times and materials.

The regression analysis was conducted using the data analysis package in Microsoft Excel, while treating each ordered pair (days corroded, effective tensile strength) as independent data points, as discussed previously. The resulting fit parameters are presented in Table 1.2. From these values, one can see that all of the slopes were nonzero to a degree of confidence greater than 95%. For a given corrosion method, the magnesium data had p-values a few orders of magnitude less than those for their iron counterparts. This indicates that the statistical values kept with observations: that magnesium wires corroded much more predictably (in a more controlled fashion) than iron wires.

Table 1.2 – Fit parameters for the four series of samples

Series	**Fit Intercept (MPa)**	**Fit Slope, β' (MPa/day)**	**p-value**	**Standard Error, s_β (MPa^2/day^2)**
Fe static coated	1101	-5.21	3.2×10^{-2}	2.34
Fe static bare	1139	-13.0	8.3×10^{-5}	2.44
Mg static coated	218.2	-5.74	6.1×10^{-8}	0.787
Mg static bare	226.0	-13.5	4.0×10^{-12}	0.740

In examining Table 1.2, an interesting observation is made about the slopes for the two different materials for a given corrosion method: they are very similar. Because magnesium is generally regarded as a quickly degrading material relative to iron, it is somewhat counterintuitive that the two materials should have the same rate of decrease in

their effective tensile strengths. However, it is important to take the rate of decrease in correct context by considering the fractional decrease in the effective tensile strengths with respect to test time. The fractional strength slopes for bare and coated corroded magnesium are, then, are -0.060/day and -0.026/day, respectively. The fractional slopes for bare and coated iron are -0.011/day and -0.005/day, respectively—a much lower value than for the magnesium wires. This difference in the rate of fractional decrease in the effective tensile strength is what leads to the perception of magnesium as a relatively quickly degrading material.

A linear regression analysis suggests that a drop of the effective tensile stress to zero should be achieved after approximately 20 and 90 days for uncoated Mg and Fe wires, respectively. In comparison to *in vivo* studies, the degradation rate is quite high; previous *in vivo* evaluations of magnesium suggest complete degradation in about 60–90 days [4] and previous work by the authors of this contribution points to incomplete degradation of iron wires even after 9 months *in vivo* [16].

1.1.4.3.6 Effect of fibrin coating on corrosion rate

A test for equality between the slopes of coated and uncoated samples for a given material was carried out using a T-test, which is presented in Equation 1.1 [28]. In this equation, the β_i' terms are the calculated slopes of best fit, the $1/\sum_j\left(X_{ij}-\bar{X}_i\right)^2$ term corresponds to the inverse of the sum of the squared residual values for the i^{th} data set, and the σ' term is described by Equation 1.2. $(SSE)_i$ represents error sum of squares for

the i^{th} data set and n_i is the number of terms in the i^{th} data set. The calculated T parameter has $(n_1 + n_2 - 4)$ degrees of freedom associated with it.

$$T = \frac{\beta_1' - \beta_2'}{\sigma' \sqrt{\frac{1}{\sum_j (x_{1j} - \bar{x}_1)^2} + \frac{1}{\sum_j (x_{2j} - \bar{x}_2)^2}}} \qquad \text{(Eq. 1.1)}$$

$$\sigma' = \sqrt{\frac{(SSE)_1 + (SSE)_2}{n_1 + n_2 - 4}} \qquad \text{(Eq. 1.2)}$$

Applying this treatment to the data yielded T = 2.070 with 50 degrees of freedom for the iron system and T = 4.443 with 44 degrees of freedom for the magnesium system. Translating these into p-values yields 4.4×10^{-2} and 5.9×10^{-5} for the iron slopes and magnesium slopes, respectively, pointing to a significant effect of fibrin encapsulation on the corrosion rate for both materials. The importance of this result is that it proves that this method is able to distinguish between degradation rates of the same material under different encapsulation conditions.

As was alluded to in the introduction, fibrin acts to slow ionic and gas transport between the corrosive agent (DMEM) and the metallic specimen. In the previous section, the corrosion times required for uncoated wires to achieve an effective tensile strength of zero were calculated. The effect of the fibrin encapsulation was to extend the metallic specimens' lifetimes to timespans closer to published values. Magnesium, which had an average uncoated lifespan of about 20 days *in vitro*, saw an extended lifespan of about 40 days after being coated with fibrin. This still does not match the 60–90 day corrosion

rate from the literature, but it has moved in the right direction, reducing the disagreement from a factor of three or four to a factor of approximately two. Iron also saw its average lifespan extended from about 90 days as an uncoated wire to approximately 200 days once it was coated in fibrin, which is also in better agreement with published values.

The fibrin encapsulation also altered the significance of the trends, as seen in Table 1.2. A decrease in statistical significance of three or more orders of magnitude, as observed in Table 1.2, may be indicative of increased error in the data resulting from randomness or anisotropy in the corrosion process. This phenomenon is not entirely unexpected; variability in the shortest path through the fibrin to the DMEM and supposed variability in the polymerization completion from sample-to-sample could both be factors that cause spots in some wires—or, for that matter, entire wires—to corrode more quickly than others. Though the encapsulation process is detrimental to the experimental repeatability, is does not follow that fibrin coating is a poor choice of factor to examine. In reality, fibrin encapsulation may be an effective way to estimate post-encapsulation degradation variability (variability following neointimal formation) *in vitro*.

1.1.5 Conclusions

The authors demonstrated in this study that iron and magnesium corroded in DMEM exhibit very different corrosion characteristics from one another. Iron corrodes locally and produces a large amount of voluminous corrosion product, under which there is a thin layer of brown/black iron oxide and a section of wire with a significantly reduced

cross section. Magnesium, on the other hand, corrodes more uniformly and ultimately evolves a white corrosion product which comprises Ca, Mg, P, and O—a result which is in line with the literature on physiological magnesium corrosion. The inclusion of a fibrin coating did not change the nature of corrosion for either material. Fracture of both of the wires occurred in a ductile manner, with the iron wire clearly failing through a microvoid coalescence-induced rupture mechanism.

This study has introduced and discussed at length tensile testing as a method for evaluating the corrosion rate of candidate materials for use in bioabsorbable stents. The downward, linear trends observed in effective tensile strength data for iron and magnesium wires with and without a fibrin coating were determined to be statistically significant to a confidence level of at least 95%. The authors proved that this method was also able to discriminate between an environment that promotes slower corrosion (immersion with a fibrin coating) and one which promotes faster corrosion (immersion of the bare wire) with statistical confidence. From the fractional corrosion rates, it was calculated that the time to achieve complete corrosion (to achieve a tensile stress of zero, constituting a "lifespan" for the wires) was approximately 20 and 90 days for uncoated Mg and Fe wires, respectively, and 40 and 200 days for fibrin-coated Mg and Fe wires, respectively.

Combining this characterization method with a simplified *in vivo* corrosion method using wires and an *in vitro* submersion test method could result in a powerful tool for low-cost, quantitative evaluation of candidate materials for bioabsorbable implant applications.

Because of the tensile testing method's apparent sensitivity to differences in the corrosion rate, it is well suited for use in screening studies of chemically modified, alloyed, and/or coated materials, which aim to identify promising material treatments.

1.1.6 Acknowledgments

The authors would like to express appreciation to Jon Stinson and Heather Getty of Boston Scientific in Plymouth, MN for several inspirational discussions that led to this project. The authors also thank Jessica Rhadigan (Forrest), Ellen Pokorney, Bryne Judy, and Becky Franke for their input in designing the corrosion protocol used in this experimentation and for assisting with other tasks. Boston Scientific is acknowledged for providing partial financial support for the early stage of this project.

1.1.7 References

[1] Heublein B, Rohde R, Kaese V, Niemeyer M, Hartung W, Haverich A. Biocorrosion of magnesium alloys: a new principle in cardiovascular implant technology. Heart 2003; 89: 391-395.

[2] Waksman R. Biodegradable stents: they do their job and disappear. J.Inavasive Cardiol. 2006; 18(2): 70-75.

[3] Onuma Y, Ormiston J, Serruys P. Bioresorbable Scaffold Technologies. Circ. J. 2011; 75: 509-520.

[4] Waksman R, Pakala R, Kuchulakanti P, Baffour R, Hellinga D, Seabron R, Tio F, Wittchow E, Hartwig S, Harder C, Rhode R, Heublein B, Andreae A, Waldmann K, Haverich A. Safety and efficacy of bioabsorbable magnesium alloy stents in porcine coronary arteries. Catheter. Cardio. Interv. 2006; 68: 607-617.

[5] Wang H, Estrin Y, Zuberova Z. Bio-corrosion of a magnesium alloy with different processing histories. Mater. Lett. 2008; 62: 2476-2479.

[6] Saris N, Mervaala E, Karppanen H, Khawaja J, Lewenstam A. Magnesium: an update on physiological, clinical and analytical aspects. Clin. Chim. Acta. 2000; 294(1-2): 1-26.

[7] Moravej M, Mantovani D. Biodegradable metals for cardiovascular stent application: interests and new opportunities. Int. J. Mol. Sci. 2011; 12: 4250-4270.

[8] Zhu S, Huang N, Xu L, Zhang Y, Liu H, Sun H, Leng Y. Biocompatibility of pure iron: *in vitro* assessment of degradation kinetics and cytotoxicity on endothelial cells. Mater. Sci. Eng. C 2009; 29: 1589-1592.

[9] Gu X, Zheng Y, Cheng Y, Zhong S, Xi T. *In vitro* corrosion and biocompatibility of binary magnesium alloys. Biomaterials 2009; 30: 484-498.

[10] Ghali E, Revie RW. Corrosion Resistance of Aluminum and Magnesium Alloys: Understanding, Performance, and Testing. Hoboken: Wiley; 2010.

[11] Kainer KU, editor. Magnesium - Alloys and Technologies. Weinheim: Wiley-VCH; 2003.

[12] Witte F, Hort N, Vogt C, Cohen S, Kainer K, Willumeit R, Feyerabend F. Degradable biomaterials based on magnesium corrosion. Curr. Opin. Solid State Mater. 2008; 12: 63-72.

[13] Witte F, Fischer J, Nellesen J, Crostack HA, Kaese V, Pisch A, Beckmann F, Windhagen H. *In vitro* and *in vivo* corrosion measurements of magnesium alloys. Biomaterials. 2006; 27: 1013-1018.

[14] Yang L, Zhang E. Biocorrosion behavior of magnesium alloy in different simulated fluids for biomedical application. Mater. Sci. Eng. C 2009; 29: 1691-1696.

[15] Müller WD, Nascimento ML, De Mele MFL. Critical discussion of the results from different corrosion studies of Mg and Mg alloys for biomaterial applications. Acta Biomater. 2010; 6: 1749-1755.

[16] Pierson D, Edick J, Tauscher A, Pokorney E, Bowen P, Gelbaugh J, Stinson J, Stinson J, Getty H, Lee CH, Drelich J, Goldman J. A novel *in vivo* approach for evaluating the bioabsorbable behavior of candidate stent materials. J. Biomed. Mater. Res. B. 2012; 100B:58-67.

[17] Seitz JM, Collier K, Wulf E, Bormann D, Bach FW. Comparison of the corrosion behavior of coated and uncoated magnesium alloys in an *in vitro* corrosion environment. Adv. Eng. Mater. 2011; 13(9): B313-B323.

[18] Xu XY, Liu T, Zhang K, Liu SH, Shen Z, Li YX, Jing XB. Biodegradation of poly(L-lactide-co-glycolide) tube stents in bile. Polym. Degrad. Stabil. 2008; 93(4): 811-817.

[19] Xin Y, Liu C, Zhang X, Tang G, Tian X, Chu PK. Corrosion behavior of biomedical AZ91 magnesium alloy in simulated body fluids. J. Mater. Res. 2007; 22(7): 2004-2011.

[20] Müller WD, Nascimento ML, Zeddies M, Córsico M. Magnesium and its alloys as degradable biomaterials. corrosion studies using potentiodynamic and EIS electrochemical techniques. J. Mater. Res. 2007; 10(1): 5-10.

[21] Xin Y, Huo K, Tao H, Tang G, Chu PK. Influence of aggressive ions on the degradation behavior of biomedical magnesium alloy in physiological environment. Acta Biomater. 2008; 4: 2008-2015.

[22] Song G, Atrens A, St. John D. An hydrogen evolution method for the estimation of the corrosion rate of magnesium alloys. In: Hryn J, editor. Magnesium Technology 2001; Warrendale, PA: The Minerals, Metals & Materials Society; 2001. pp 255-262.

[23] Bazbouz MB, Stylios GK. The tensile properties of electrospun nylon 6 single nanofibers. J. Polym. Sci. Polym. Phys. 2010; 48: 1719-1731.

[24] Makar GL, Kruger J. Corrosion of magnesium. Int. Mater. Rev. 1993; 38(3): 138-153.

[25] Bates R. Modeling of ductile fracture by microvoid coalescence for the prediction of fracture toughness. In: Wells J, Landes J, editors. Fracture: Interactions of

Microstructure, Mechanisms, Mechanics; Warrendale, PA: The Metallurgical Society of AIME; 1984. pp 117-155.

[26] Xin Y, Huo K, Hu T, Tang G, Chu P. Corrosion products on biomedical magnesium alloy soaked in simulated body fluids. J. Mater. Res. 2009; 24(8): 2711-2719.

[27] Virtanen S, Fabry B. Corrosion, surface modification, and biocompatibility of Mg and Mg alloys. In: Sillekens W, Agnew S, Neelameggham N, Mathaudhu S, editors. Magnesium Technology 2011; Warrendale, PA: The Minerals, Metals & Materials Society; 2011. pp 409-412.

[28] Bertha RM, Duran BS, Boullion TL. Statistical methods for engineers and scientists. 3rd ed. New York: Marcel Dekker; 1995.

[29] McCrum NG, Buckley CP, Bucknall CB. Principles of Polymer Engineering. 2nd ed. Oxford: Oxford University Press; 1997.

[30] Chawla KK. Ceramic Matrix Composites. 2nd ed. New York: Springer-Verlag; 2003.

1.2 New approaches in evaluating metallic candidates for bioabsorbable stents[2]

1.2.1 Abstract

A series of unconventional approaches has been developed at Michigan Technological University, which is able to screen candidate materials for use in bioabsorbable (or

[2] The material in Section 1.2 was previously published in *Emerging Materials Research* and is reproduced here with permission.

P. K. Bowen, J. Drelich, R. E. Buxbaum, R. M. Rajachar, and J. Goldman. "New approaches in evaluating metallic candidates for bioabsorbable stents." *Emerging Mater. Res.* 1(5) 237-255 (2012), doi: 10.1680/emr.12.00017.

References in Section 1.2 follow the *Emerging Materials Research* author guidelines.

bioresorbable) stents by reducing the scale of necessary animal studies and the complexity of biocorrosion analyses. Using a novel *in vivo* approach, materials formed into a simplified wire geometry were implanted into the wall of the abdominal aorta of rodents for several weeks or months to measure the extent of *in vivo* degradation, quantify mechanical strength over time, characterize the resulting products, and assess biocompatibility. An *in vitro* method was developed to identify bioabsorbable candidate materials, reproduce the corrosion products formed *in vivo*, and predict the degradation rate of stent materials. To accomplish this goal, wires were encapsulated in an extracellular matrix and corroded in cell culture media *in vitro*. Encapsulation of the wires *in vitro* was necessary in order to mimic *in vivo* stent encapsulation within a neo-intima. Alternatively, accelerated *in vitro* corrosion for materials with very low corrosion rates was accomplished by exposing fibrin-coated wires to a steady flow of cell culture media. After *in vivo* and *in vitro* tests, wires were subjected to tensile testing to quantify the rate of material degradation and loss of mechanical strength.

1.2.2 Introduction and Background

Coronary artery disease often culminates in vascular occlusion by way of conditions such as atherosclerosis. The occluded arteries must be repaired by coronary angioplasty, in which the blockage is compressed radially and the vessel mechanically widened to restore blood flow. Stents are commonly used in conjunction with balloon angioplasty to provide structural support and prevent collapse of the vessel after the balloon is withdrawn. Although the benefits of cardiac stents are numerous and well-documented,[1,2]

the scaffolding is not thought to play an important role after remodeling is complete. The short-term benefit can be overshadowed by long-term complications such as chronic inflammation,[3] late stage thrombosis,[4] and stent strut disruption.[5] In addition, restenosis often follows conventional stent implantation and is caused by neo-intimal proliferation and migration.[6,7] Newer drug-eluting stents have reduced but not eliminated restenosis relative to bare metal stents.[8]

Bioabsorbable—or "bioresorbable" or "biodegradable"—stents have potential as alternatives for vascular scaffolding that circumvent many of the current, long-term health risks of conventional permanent stents.[9,10] The ideal bioabsorbable stent would retain mechanical properties for approximately six months before being broken down, metabolized, and excreted by the body, allowing the vessel to function and remodel naturally.[11] Past investigations into bioabsorbable stent materials have focused on both polymeric and metallic variants. Poly-L-lactic acid (PLLA) has been shown to possess acceptable biocompatibility,[12] but a polymeric stent requires a greater strut thickness than most metal stents because of the polymer's lower relative strength.[13] Other limitations reported with polymer stents include the inability to expand completely with balloon dilation[14] as well as restenosis and smooth muscle hyperplasia rates similar to those observed for conventional bare metal stents.[15] For these reasons, bioabsorbable metal stents are being investigated.

Generally, alloys based on elements that have physiological roles in the human body are likely to be biocompatible and are therefore suitable materials for constructing

bioabsorbable stents. Specifically, magnesium (Mg) and iron (Fe) have been shown to hold promise due to their mechanical properties and purported biocompatibility of the base components.[16–19] Other biologically important materials, such as calcium, would degrade too quickly if placed in a physiological environment. Fe has a high mechanical strength, which allows for production of stents with a broad range of inner diameters.[20] Both Fe and Mg metals have higher tensile strengths and elastic moduli than biodegradable polymers[21,22] and can therefore provide a stiffer, stronger scaffolding to support the vessel and promote healing. Both metals exhibit mechanical behavior that is more predictable than that of polymers and the stent manufacturing industry has a well-established record of working with metallic materials, making the task of manufacturing a stent for deployment and arterial support relatively straightforward. Mg and its alloys have the additional benefit of inherent hypothrombogenicity,[23] which may explain the lack of thrombotic complications in past clinical trials.[11]

While the metallic stent materials are favored in several areas, implementation of these materials is not straightforward. Unfortunately, Mg alloys of commercial purity exhibit a relatively high rate of degradation and associated evolution of hydrogen gas.[24,25] In addition, some trials have shown that Mg completely bioabsorbs as early as 60 to 90 days post-implantation.[11] Many groups are currently pursuing specialized alloys, coatings, and processing techniques aimed at slowing the physiological corrosion rate of Mg. Meanwhile, Fe has been reported to possess excellent biocompatibility, with no signs of local or systemic iron toxicity, in addition to slow degradation that prevents fragment

embolization.[20,26] In contrast to Mg, Fe is generally believed to degrade too slowly to be used in its pure form in bioabsorbable applications.[27]

1.2.2.1 State of the art in bioabsorbable metallic materials

The industrial and academic community's current research and development efforts are largely concentrated on either accelerating or decelerating the degradation of Fe and Mg stent materials, respectively. In the case of Mg, a reduction in the corrosion rate is badly needed, as some modern works have gone as far as to dismiss the possibility of Mg implants on the basis of hydrogen evolution alone.[28] Multiple approaches have been taken to limit the degradation experienced by Mg stents, with limited success.[29-31] Mg alloys containing rare earth (RE) elements, such as WE- and AE-series alloys traditionally used in high temperature applications where creep resistance is paramount,[32] have become the focus for bioabsorbable stent development. These RE-bearing alloys have exhibited reduced degradation rates relative to other, more common Mg alloys.[33,34] Non-conventional processing methods have been used by others to produce prototypical alloys that are described as "stainless magnesium" in a recent review by Atrens *et al.*[35] An example of this approach is the work conducted by Hoffmann and coworkers in developing solid solution Mg-Ti alloys through nonequilibrium processing, namely high-energy ball milling.[36] It appears that research is currently focused on alloying, as opposed to coatings, which have traditionally been geared towards automotive applications.[37]

Aluminum-containing Mg alloys consistently perform well in *in vitro* corrosion studies intended to screen candidate materials.[23,24] However, concerns about aluminum-containing alloys have been raised in recent years, prompted by reports from toxicology and neurology researchers who have identified the prospect of aluminum toxicity.[38,39] These toxicological concerns, however, are not founded in data related to bioabsorbable implants and often use much higher aluminum concentrations than one would expect to be released from a degrading stent. Furthermore, the aluminum introduced in many of these studies comprises trivalent aqueous aluminum, not metallic specimens that are allowed to passivate and/or dissolve naturally, as would occur in an implant scenario. Moderate doses of aluminum that produce low serum concentrations are readily eliminated via renal action, indicating that dismissal of this series of alloys may be premature.[40,41]

In addition to alloy development work, attempts have been made to clarify the mechanism that governs magnesium degradation in a pseudophysiological environment. The work that has been done thus far points to direct participation by chloride, bicarbonate, phosphate, and calcium ions in the corrosion process as well as less direct participation by other ions, blood/cellular constituents, and dissolved gasses such as CO_2.[42,43] More broadly, though, magnesium deterioration depends on several parameters: makeup of the alloy, metallurgical treatments, surface treatment (coatings, ion implantation, etc.), species and concentration of the interacting electrolytes, chemistry

and biology of the environment, and the transport and metabolic phenomena associated with the reactants and the products of the corrosion reaction.[44]

Although there is less interest in iron stent materials, recent work on iron has aimed to increase the corrosion rate through creation of Fe-Mn alloys containing up to 35 wt.% Mn.[45,46] This material was successful in increasing the corrosion rate of the material significantly. However, for reasons discussed in the section on *in vivo* evaluation of materials, the authors have evidence showing that pursuit of Fe-based stent materials may be a fruitless endeavor.

1.2.2.2 The need for improved testing methods

The enormous number of alloys and coating materials that could potentially be tested in pursuit of an ideal bioabsorbable implant material exceeds current resources for evaluating their corrosion behavior, making this screening process excessively time-consuming and costly. Because of this, the authors found it necessary to pursue the development of testing methods for evaluating candidate materials that have reduced complexity and increased cost-effectiveness. This has resulted in a suite of complimentary *in vivo*, *in vitro*, and analysis techniques, which are described together in this contribution. The methods are most useful when used concurrently, as illustrated in Figure 1.10.

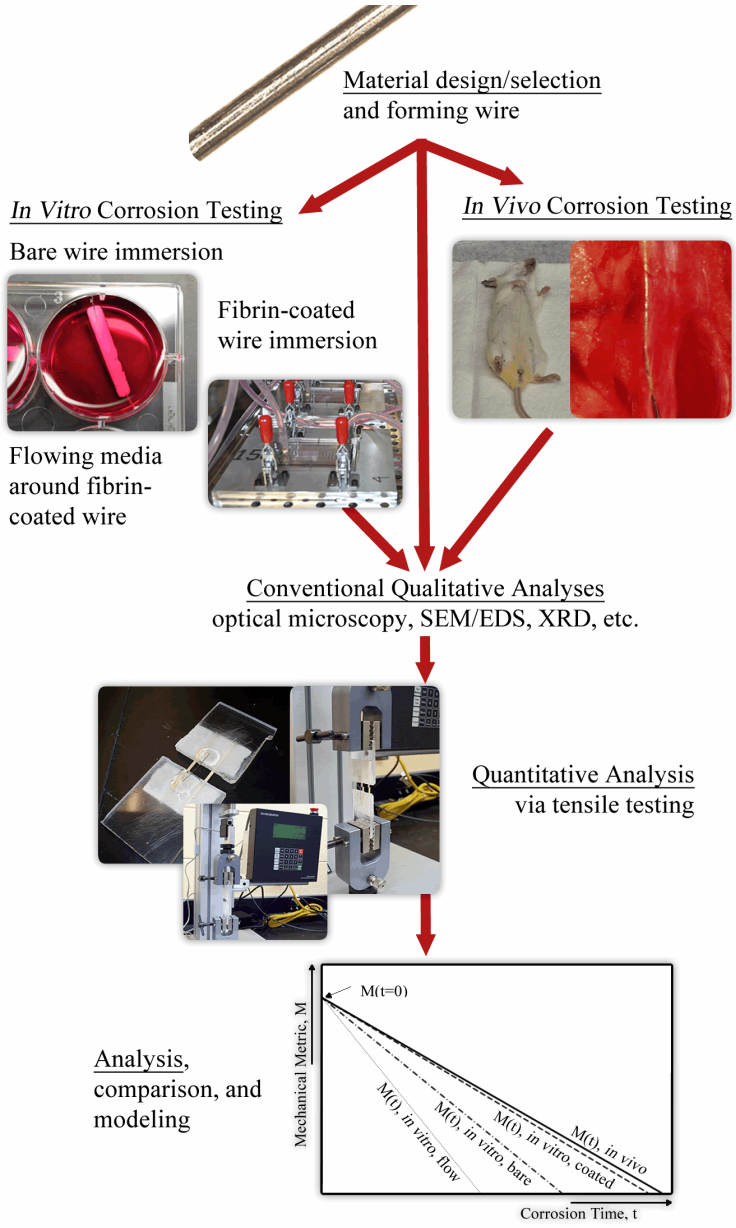

Figure 1.10 - Flowchart showing how a candidate bioabsorbable material can be tested and compared with existing materials using the suite of methods (*in vivo*, static and dynamic *in vitro*, and quantitative analysis through tensile testing) presented in this contribution.

Both *in vivo* and *in vitro* methods utilize a sample with a simplified wire geometry, which allows for easy implantation, explantation, sample handling, corrosion characterization,

and mechanical evaluation. The wires used in this work were 0.2–0.3 mm in diameter, high-purity, and stock with an as-drawn temper (from Goodfellow; Huntingdon, England). Methods have been presented by Seitz *et al.* by which one may form wires of a comparable diameter from a billet of experimental or custom alloy.[47,48] Other sample morphologies, such as "strips" (rectangular prisms) of material have been used in other preliminary studies,[49] as well as in producing some preliminary data presented by the authors in this report. However, the circular wire geometry is generally more conducive to batch production, testing, and analysis.

1.2.3 Methods for Testing Bioabsorbable Materials

1.2.3.1 Arterial implantation utilizing a rodent model

Some of the most important information on bioabsorbable implants with respect to biocorrosion, biocompatibility, and localized effects of degradation (i.e. corrosion product migration, cytotoxicity, etc.) has been generated from physiologically relevant *in vivo* studies. To date, relatively few reports have been published on the behavior of materials *in vivo* in comparison to the body of literature that has grown on materials corroded *in vitro*. *In vivo* evaluations of interventional cardiology devices are more often conducted by industrial labs than by academic investigators, and involve large animals such as pigs. The unfortunate consequence of these circumstances is a lack of disclosure and interinstitutional cooperation due to intellectual property and competitive concerns. The typical cost for a six-month *in vivo* study using a mini-swine subject and deployable stent would be at least $10,000 to $12,000 per animal.[50] Using the rodent implantation

technique, by the authors' estimate, the cost is reduced to less than 10% of that for the mini-swine study including the surgical procedure, animal housing, and all post-explantation analysis. Certainly, in late-stage trials where more detailed human health-related questions must be addressed, the mechanically expanded stent inside the porcine coronary artery is preferable to the implantation of wire geometries into small rodent arteries. However, the rodent model is more accessible to most universities' materials research programs and may be a more reasonable approach for evaluating degradation behavior as a pre-screening model to identify promising stent materials prior to stent manufacturing and large animal implantation studies.

Most of the *in vivo* works in the scientific literature related to bioabsorbable materials investigate degradation of orthopedic implants[34,51,52] or corrosion in a subcutaneous environment,[53] which can be easily accomplished in small animals such as rabbits or guinea pigs. However, these models are not suitable for determining the lifespan and behavior of a vascular device due to large differences in biological milieu between the arterial, orthopedic, and subcutaneous tissues. For this reason, the authors have developed an animal model in which a wire of the candidate material is implanted into the rat abdominal aortic artery, positioned either in direct blood contact inside the lumen or in the arterial wall, as shown schematically in Figure 1.11. A 0.2–0.3 mm diameter wire is preferred because it is commercially available and is approximately the same diameter as a typical stent strut. A 20–30 mm sample length is well suited for characterization and handling; 20 mm for Mg and 30 mm for Fe is now preferred for

mechanical testing (discussed later). Smaller, typically 5–10 mm, segments of wire may be simultaneously implanted at a different location along the artery to provide samples for characterization with optical microscopy (OM), scanning electron microscopy and energy dispersive spectroscopy (SEM/EDS), Raman spectroscopy, Fourier transform infrared spectroscopy (FT-IR), etc. The abdominal rat aorta can accommodate roughly 30 mm of combined wire length, although longer wire lengths than 20 mm are more challenging than smaller lengths to implant. Specific preparation, sterilization, and related procedures can be found in the authors' previous contribution.[54]

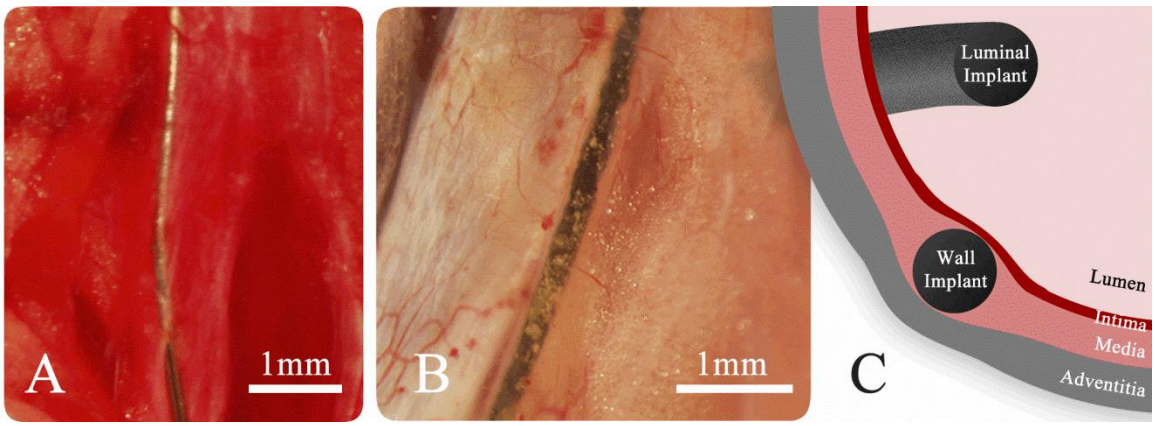

Figure 1.11 - *In situ* photographs of the wire states upon implantation (A) and explantation (B), after three weeks' degradation, are presented. The schematic (C) shows the position of the wall implant wire in the arterial media and the luminal implant wire positioned away from the intima.

The position of the wire—in the arterial wall or in the lumen—determines the nature and composition of the wire's environment, which greatly influences the corresponding degradation that occurs. Positioning the wire in the lumen replicates the conditions a stent experiences during its early life, before it becomes encapsulated in neointimal tissue. The material is exposed to flowing blood, including circulating immune cells,

platelets, constituent biomolecules, and dissolved gasses. Cellular action does not have a large effect on Mg corrosion at this stage, as the surface does not typically become encapsulated by a thrombus.[23] Conversely, implantation in the arterial wall works to mimic the environment a stent material is subjected to after it has been encapsulated by neointimal tissue. The wall environment includes modified, generally reduced, mass transport properties, cyclic stresses, cellular action by vascular cells, and phenomena specific matrix/ionic milieu. Since the authors have found that the wire undergoes the bulk of its degradation after being encapsulated, use of the rodent wall model is preferred for simplicity in preliminary work.

During implantation in the wall environment, the wire is pushed through the adventitia and into the media. Care is taken to avoid puncturing the intima during surgery, so that the sample is implanted within the media, as illustrated in Figure 1.11(A) and the associated schematic (C). The luminal implants require that the intima be punctured during implantation so that the wire can be threaded through the artery, as in the schematic [Figure 1.11(C)]. When Mg implants are removed from the euthanized rat, corrosion is often obvious on the wire's surface, as in Figure 1.11(B), but corrosion product is not typically observed in the tissue. The media and adventitia tissues do not adhere well to pure, corroded Mg wire, allowing for easy extrication of the sample and preservation of the corrosion products. The relatively poor adhesion may be due to the nature of the corrosion layer, which has been hypothesized to comprise a strongly hydrated layer of amorphous and/or semicrystalline $Mg(OH)_2$ when corroded in water.[55]

Fe exhibits very different corrosion behavior when implanted in the arterial wall for an extended period. Elemental (EDS) maps of a nine-month wire/tissue cross section are presented in Figure 1.12. These maps show that a passive layer initially formed on the wire but was later "pushed away" from the Fe core. This passive layer is displayed as a bright green/yellow area on the calcium/phosphorus map. From the iron/oxygen map, one can see that a significant amount of iron oxide has developed between the passive layer and the remaining Fe. These results are indicative of the evolution of a voluminous Fe-O corrosion product, which was confirmed by histological examination[54] and by results presented later. The corrosion products do not appear to be excreted nor metabolized at an appreciable rate. Instead of dissolving in an apparently harmless manner, pure Fe seems to be unsuitable for application in interventional cardiology due to the accumulation of voluminous corrosion products in the arterial walls of rats.[54] Mg has not exhibited the same buildup of corrosion product, but instead appeared to dissolve harmlessly,[54] suggesting that Mg and its alloys are currently the most promising bioabsorbable materials.

1.2.3.1.1 Use in candidate material evaluation

The rodent arterial implant model was only recently introduced, so there is limited experimental evidence showing that the technique is useful for evaluating novel bioabsorbable materials. The authors show here\ that the arterial implant model can, in fact, be used to quantify corrosion experienced by alloyed Mg implants. A section of hot-rolled Mg-9 wt.% aluminum (A9 in conventional notation[56]) foil was examined. Due to relatively low ductility, A9 (similar to AZ91) is difficult to draw into a round wire, so

a strip of material was instead prepared with a low-speed diamond saw and fine-grit SiC sandpaper. A section measuring approximately 18 mm long, 600-700 µm wide, and about 200 µm thick was implanted into the arterial wall in a manner identical to that described above.

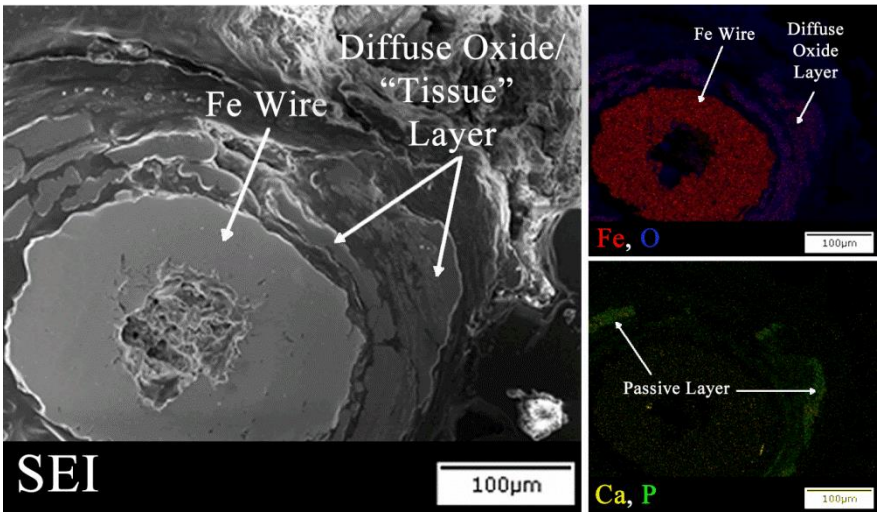

Figure 1.12 – SEI and elemental maps of a wire/tissue cross section. The Fe and O elemental maps are superimposed in the top right image, and the Ca and P elemental maps are superimposed in the bottom right image. The purple areas in the Fe/O map correspond, then, to iron oxide, and bright spots on the Ca/P map correspond to some calcium phosphate product.

After 3 months *in vivo*, the sample was removed and the explant was examined in whole and in cross section using OM and SEM/EDS. The results are presented in Figure 1.13 with an optical micrograph of the entire strip presented in Figure 1.13 (left), an optical micrograph of the cross section presented in Figure 1.13 (top), and two EDS spectra corresponding to the metallic core (left spectrum) and the corrosion product (right spectrum). Cracking was readily observable on the wide face of the explant, a feature

typical of corroded Mg that is usually attributed to dehydration of the corrosion layer.[57] There also appeared to be an area of localized mineralization on the exterior surface; EDS analysis showed that the white feature was composed almost exclusively of Ca and P (data not shown). The cross section revealed an apparently intact Mg core, the light area, surrounded by a corrosion product layer, the dark area. The surrounding gray area on the cross section is the mounting epoxy and plastic sample clip used to secure the sample.

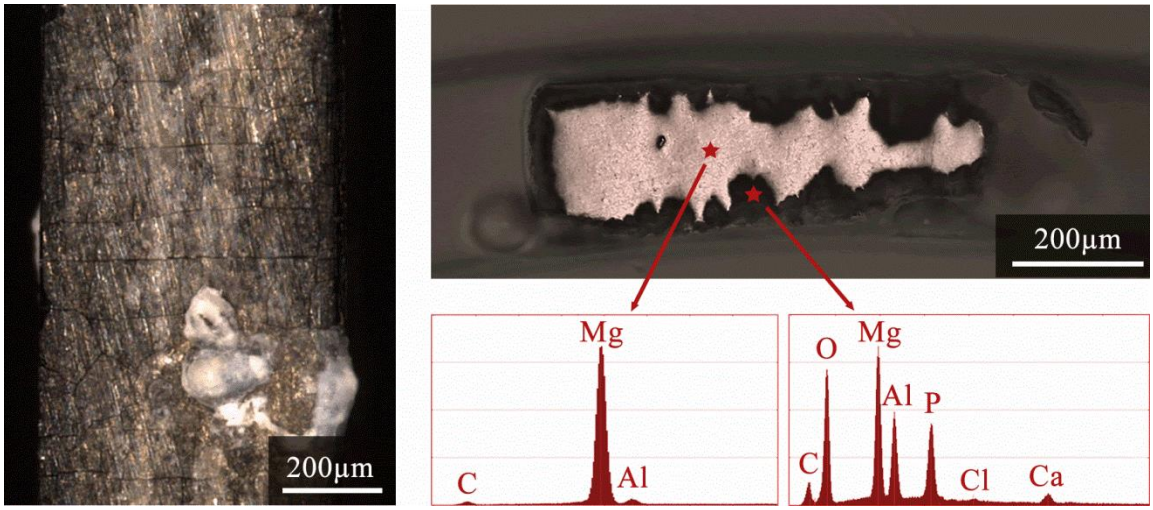

Figure 1.13 – Optical micrographs of the implanted A9 strip on the wide face (left) and in cross section (top). Two schematic EDS spectra from the carbon-coated sample are shown. The left spectrum corresponds to the matrix metal and shows that Mg and Al radiation was generated. The right side corresponds to the corrosion product layer and comprises primarily Mg, Al, O, P, and Ca radiation with trace C and Cl.

Elemental analysis of the corrosion layer and the metallic core yielded results consistent with past experimentation. The metallic core showed evidence of Mg and Al radiation with C radiation originating from the conductive carbon coating. The corrosion layer again showed evidence of Mg and Al radiation, but with a higher Al:Mg peak height ratio, signifying Al enrichment. The corrosion layer also revealed radiation from O, P,

and Ca, with trace Cl. The C peak seemed to be more intense than the C peak originating from the metallic phase, indicating that the corrosion layer may also contain chemically bonded carbon atoms in addition to the conductive carbon coating. These results are in agreement with preliminary *in vitro* data that have been collected using human whole blood with regard to the P and Ca content of the corrosion layer.[23]

When imageJ (National Institutes of Health, USA) was used to perform a cross sectional analysis of the explanted A9 strip, it showed an approximate cross sectional area reduction of approximately 41% after a duration of three months post-implantation. This cross sectional area reduction corresponds to a 0.06 mg/cm^2/day mass loss and 0.12 mm/year rate of penetration. This degradation rate is on the same order of magnitude as *in vivo* degradation rates of a LAE442 alloy, which was reported to have a 0.31 mm/year penetration rate at three months *in vivo* as an orthopedic implant.[58] This result using A9 Mg alloy proves that the experimentation performed *in vivo* using the arterial implantation in rats produces degradation rates that are comparable to those shown by comparable *in vivo* methods.

1.2.3.1.2 Use in exploring other biodegradation processes

Even though the rodent arterial implant model was developed for bioabsorbable material degradation studies, it has since proven useful for exploring other biological processes in the arterial environment. Calcium is a biocompatible material that may prove useful in the development of bioabsorbable stents. For instance, hydroxyapatite has already been used as reinforcement in an experimental bioabsorbable metal matrix composite in a

study conducted by Witte and coworkers.[59] To clarify the degradation behavior of calcium-rich materials in the arterial environment, Ti-6Al-4V wires were coated with a calcium phosphate layer by immersion in a 1.5× concentrated simulated body fluid containing 7.5 M Mg^{2+} to inhibit crystal growth for 24 h at 37°C. A thin (< 3 μm) layer of amorphous calcium phosphate was thus deposited on the implant surface. Atop this coating, a thick (30 μm) coating of crystalline calcium phosphate was grown by immersion in a supersaturated calcium phosphate solution for 48 h at 37°C. The resulting layer, as indicated by SEM/EDS, was composed of octacalcium phosphate (OCP), $Ca_8H_2(PO_4)6{\cdot}5H_2O$. The OCP-coated wires were then implanted into the arterial environment for 9 months. The purpose of this experiment was to examine the modification of the OCP layer by both environments and to identify possible differences between the environments with regard to calcium-rich materials.

After initial experiments, the wires were examined via field emission SEM. The surfaces of the wires explanted from the two environments were vastly different, as shown in Figure 1.14. After nine months, the OCP layer is still readily visible on the wire that was implanted in the luminal environment [Figure 1.14 (A)], but the OCP layer was completely absent on the wire that spent nine months in the arterial wall [Figure 1.14 (B)]. This leads to the observation that implantation of a calcium-rich material in the wall environment leads to active removal of the calcium content over several months. The mechanism for this OCP-stripping phenomenon is not currently known, but it could have important implications in bioabsorbable stent development and merits further

investigation. The authors posit that the rodent arterial implant model can play a key role in this investigation.

The difference between the behavior of metallic materials in the luminal and wall environments is similarly illustrated by inspecting the degradation of candidate bioabsorbable materials (Mg and Fe) in the two locations. Whereas attack in the luminal environment was generally quite limited, samples inserted into the wall underwent substantial corrosion. Figure 1.14 illustrates the difference in biocorrosion of Mg in the luminal versus wall environments in (C) and (D), respectively.

It can be seen that the wire samples are mildly corroded in the lumen, as the surface appears tarnished in Figure 1.14(C), but there is little to suggest that there is any localized attack or through-thickness corrosion. However, the attack in the arterial wall is much more substantial and the fragmentation that results is evidenced by Figure 1.14(D). Fe extracted from the luminal environment [Figure 1.14(E)] appears to be lightly corroded, while the wall contacting surfaces on a portion of the Fe sample in Figure 1.14(F) have ballooned outwards because of the evolution of a voluminous corrosion product.[54] The precise reason for this difference between the luminal and wall environment with respect to material degradation is currently unknown. However, it will likely play a key role in the evaluation of bioabsorbption, as the pre- and post-encapsulation degradation rate of any candidate biomaterial will differ in a manner similar to the wires presented in Figure 1.14.

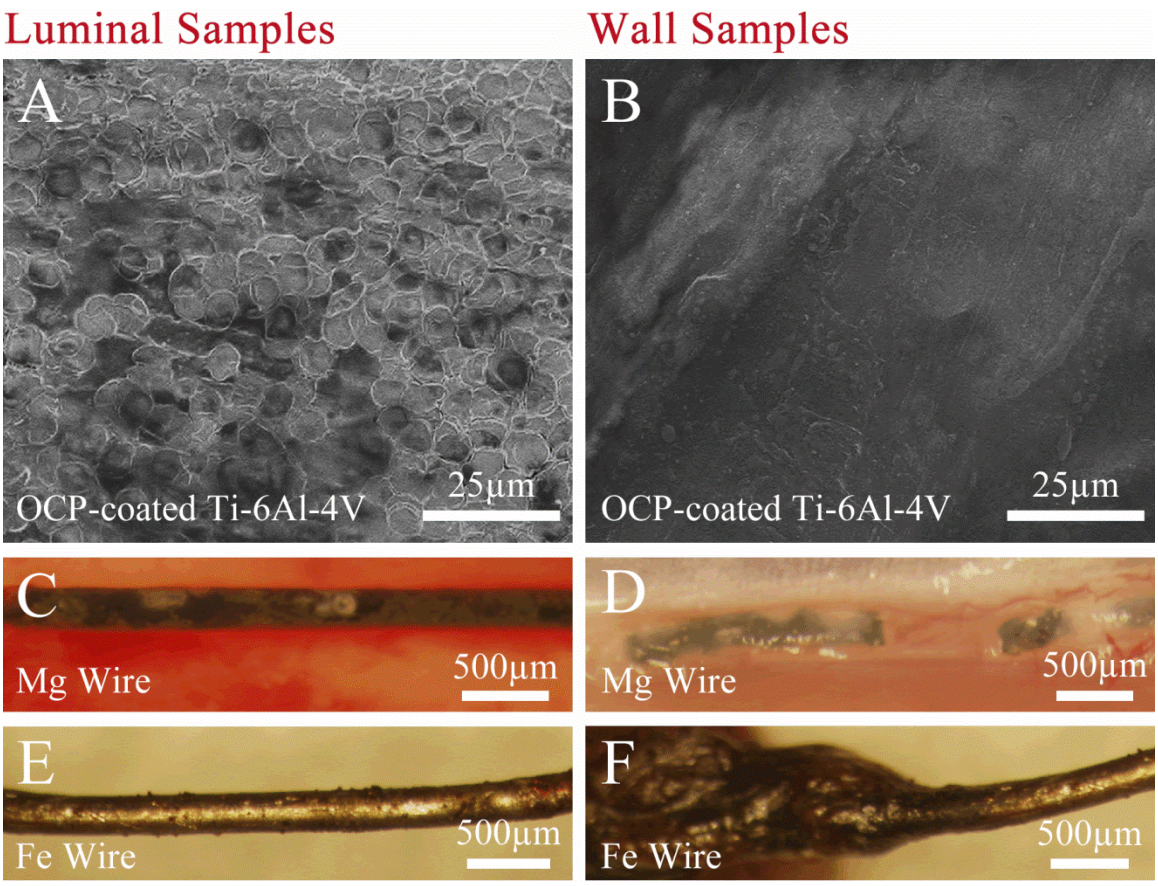

Figure 1.14 – General differences between the luminal and arterial wall environment illustrated by: two OCP-coated Ti-6Al-4V wires after 9 months' time in the arterial lumen (A) and wall (B) showing presence and absence of the initial OCP layer, respectively; Mg wires corroded in the lumen (C) and wall (D) showing mild and severe attack, respectively; and Fe samples corroded in the lumen (E) and wall (F) showing negligible attack and accelerated attack, respectively.

1.2.3.1.3 Challenges to use of the rodent model

The rodent model shows promise in greatly reducing the cost and time required to conduct *in vivo* material evaluation. However, researchers must be aware of some drawbacks related to the technique. In general, the few deficiencies of the rodent model are offset by cost savings and widespread accessibility, especially in preliminary investigations.

The wire represents a small segment of a stent and does not simulate all aspects of stent/artery interaction, such as forces originating from artery-implant interaction and injury to/inflammation of the arterial wall. This model does not replicate all mechanical conditions that a stent is subjected to while in service. However, this model does allow for reliable investigation of the metal-blood and metal-matrix interface. It also allows for identification of physiological corrosion products and an estimate of the lifetime of an actual stent, barring any drastic modification of that time by effects such as stress corrosion cracking. With the relatively low level of mechanical stresses expected during service, these issues, while important to the future of metallic bioabsorbable stent development, should not completely control corrosion of straight, uniform stent strut segments. As mentioned previously, a relatively expensive large animal study with a balloon-deployed stent would be required to investigate the influence of mechanical forces on degradation.

Another potential problem is that the animal model also lacks atherosclerotic lesions, which may contain considerable calcium, phenotypically modulated smooth muscle cells, and dysfunctional endothelial cells. However, the significant benefit of the rodent wire implantation approach relative to a large animal stent implantation is that it can be used to quickly evaluate the corrosion behavior of novel stent materials while incurring minimal costs. *In vivo* trials using small animals before further material refinement and/or large animal implantation are critical to avoid costly mistakes. Thus, this type of small animal testing, while lacking details such as atherosclerotic lesions, is an

appropriate precursor to large animal studies in which these details may be replicated at greater cost.

1.2.3.2 Attempts to replicate *in vivo* results *in vitro*

Although *in vivo* studies are useful for screening late-stage material candidates (i.e. a limited number of variants within a single alloy system), *in vitro* methods are better suited for multi-candidate (i.e. multi-alloy system) screening experiments. In general, *in vitro* methods are highly flexible, as one can use simple conditions such as static submersion test conditions, or complicated conditions such as flowing media. Regardless of the conditions used, the litmus test for success should be reasonable replication of the *in vivo* corrosion mechanism.

Currently, there is no universally agreed-upon *in vitro* test that accurately predicts *in vivo* corrosion for metallic materials. Recent work by Geis-Gerstorfer *et al.*[23] and Schille *et al.*[60] using a dynamic environment containing human whole blood has shown markedly similar corrosion characteristics compared to corrosion experiments performed *in vitro* through submersion in Dulbecco's Modified Eagle Medium (DMEM) both with and without fetal bovine serum added[61,43] and simulated body fluid (SBF).[62] Other solutions that have been used include Hank's balanced salt solution (HBSS, or "Hank's Solution") and phosphate buffered saline (PBS), both of which have failed to replicate corrosion in explants and samples placed in contact with human whole blood. When medical facilities are not readily accessible, the use of human whole blood may not be feasible. For this

reason, DMEM and SBF will likely be the favored *in vitro* corrosion media in many materials labs.

The authors have developed two novel *in vitro* techniques with two different applications: a technique involving static submersion of fibrin-coated wires, and a second technique involving laminar flow of media over a fibrin-coated wire. The conventional wire submersion in static media was used as the *de facto* control.

1.2.3.2.1 Static submersion of fibrin-coated samples

Though simulation of *in vivo* corrosion with *in vitro* approaches is commonly undertaken with DMEM, SBF, and human whole blood, an important limitation of this approach is the lack of an accurate recapitulation of *in vivo* kinetics. An evaluation technique devoid of animal testing would be particularly useful if applied in materials laboratories where access to animal facilities is limited. Furthermore, measurements collected using bare wires submerged in the aforementioned solutions are of limited usefulness; the results can only be interpreted in a relative manner (e.g. in relation to commercially pure Mg or some *in vivo* data). The static *in vitro* method is simple, straightforward, and, when refined, will require the same amount of time as a full small animal study using rats at a reduced cost.

The disagreement in kinetics between submersion and *in vivo* models may be related to the reduced capacity for mass transport across the biological matrix—that is, the diffusion coefficient is lower in tissue than in a liquid. Hence, in order to develop a more

realistic *in vitro* test method that also mimics the kinetics of *in vivo* degradation, it was necessary to encapsulate the biodegradable metal with a diffusion-restrictive coating. Preliminary experimentation showed that fibrin—a highly networked material—more effectively modulated the corrosion rate than collagen—a non-networked material. Because of this, experimentation done thus far has utilized a "fibrin casting" technique, details of which are presented in the Appendix. This is a first step in being able to obtain an accurate estimate of the expected lifetime of a bioabsorbable device from *in vitro* analyses.

A metallographic cross section of a corroded wire is presented in Figure 1.15. The wire shown was corroded with a fibrin sheath for four weeks in DMEM in accordance with the protocol outlined above. The secondary electron image (SEI) shows, at first glance, a non-circular cross section with odd-looking protrusions. However, when elemental mapping was performed it was quickly apparent from the Mg and Ca maps (as well as the composite map) that the circular shape of the original wire was retained to a large degree. The abnormal features on the exterior are Ca- and P-rich, indicating that localized calcification of the wire occurred. Moving inward, a bulk corrosion product containing Mg, Ca, O, P, and maybe C, occupies a sizable fraction of the cross section of the corroded wire. An intact Mg core is readily visible as a bright blue area in the elemental map. There also appears to be a slightly Mg- and O-enriched region immediately to the southwest of the Mg core, which may correspond to a second corrosion product.

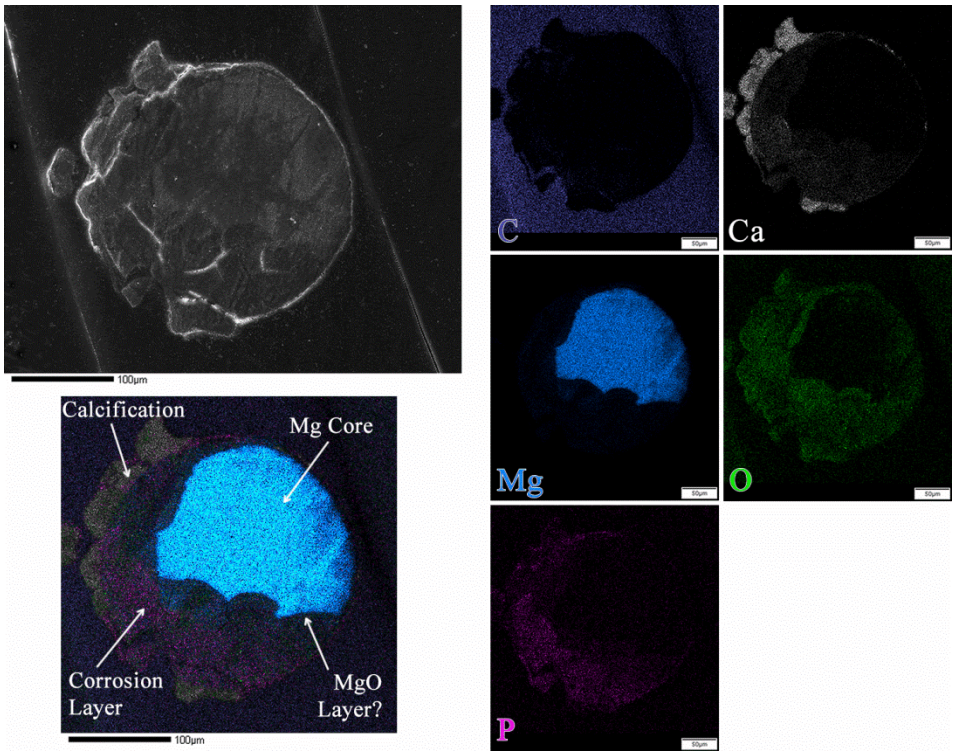

Figure 1.15 – SEI (top left) and elemental maps of a magnesium wire that was corroded *in vitro* with a fibrin sheath for four weeks. The composite map (bottom left) shows three or four regions of composition: a metallic Mg core (bright blue), calcification on the exterior of the wire (gray), bulk corrosion layer (purple/gray/blue/green intermixed), and possibly a Mg oxide-rich region near the core (blue/green). The composite map is broken into is constituent element maps to the right; all constituent map scale bars are 50 µm.

The wire itself underwent uniform corrosion, as it is typically defined,[63] although the corrosion product is not of uniform thickness. Nonuniform distribution of fibrin around the wire allows much more rapid mass transport from one surface, just as it would in an arterial environment. Similar corrosion distribution was observed by Waksman *et al.* during the histological examination of an iron stent explanted from a porcine subject.[64] Thus, corrosion appears to be much more rapid on the "outward-facing" side of the wire, resulting in higher penetration rates. A cross sectional area analysis of the wire in Figure

1.15 yields a degradation rate of 0.20 mg/cm^2/day or a penetration rate of 0.42 mm/year. It should be noted that this value is largely a function of the fibrin encapsulation; one may modify the corrosion rate by changing the thickness or concentration of the encapsulant (fibrin). It is the expectation of the authors that this methodology may be further refined to the point where the thickness and concentration of the encapsulant is engineered to give the same corrosion rates as the *in vivo* implantation model. If this were to happen, accurate testing may be performed *in vitro* without calibration experimentation involving small animals, opening the door for material development without intensive use of animal facilities.

The degradation of iron wires is fundamentally different from the corrosion of magnesium under these conditions. In many cases, it appears that the bulk of the wire remains passive in DMEM while pitting occurs at a few sites along the length of the wire. When degradation occurs by this mechanism, uniform corrosion is of minimal interest. In addition to a schematic showing the internal structure of the circumferential pits as determined by optical examination, a typical example of Fe corrosion in static media is presented in Figure 1.16. The typical morphology is a large (two or three times the nominal wire diameter) "ball" of fragile, brown corrosion product under which the wire has a severely reduced cross section. Immediately adjacent to the "ball," there is often a short segment where the passive layer on the wire is apparently disrupted, resulting in blistering and discoloration. Along the wire, away from the voluminous corrosion product, the wire remains shiny and unaffected. It is likely that similar pitting

mechanisms to those outlined by Jones[63] (for Fe pitting) and MacDonald[65] (for pit initiation) are responsible for the localized breakdown of Fe wires.

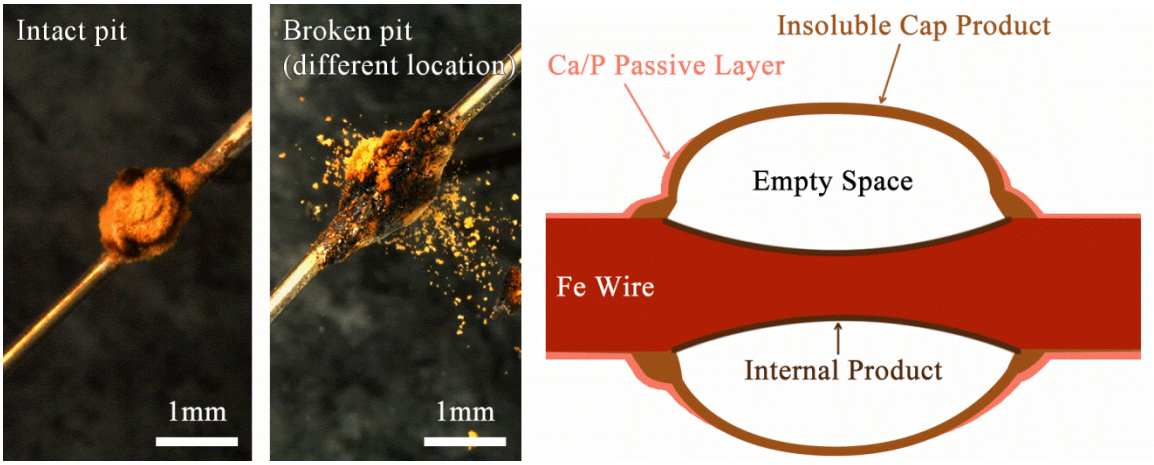

Figure 1.16 – Pit morphology on an iron wire corroded *in vitro* in static media for two weeks of an intact pit (left) and a broken pit (middle). A schematic of a typical pit in cross section is presented on the far right showing the disruption of the passive layer adjacent to the pit cap product as well as the empty space between the wire core and the insoluble pit cap.

1.2.3.2.2 Laminar flow over encapsulated samples

In the field of bioabsorbable material development, it is desirable to use accelerated corrosion experiments with the purpose of rapidly screening candidate compositions. A dynamic environment (i.e. with flowing media, cyclic stress, and/or other factors) does not appear to be strictly required to mimic the basic corrosion behavior (mechanism) of Mg, as that can be accomplished with static submersion. However, the use of flowing media is able to accelerate the corrosion of candidate materials to the point that evaluations of material degradation relative to a standard sample (i.e. bare Mg or bare Fe) can be completed in a matter of days. An *in vitro* test method has been devised using a

parallel plate flow chamber that promises to be highly scalable and can accommodate many samples at once. On a small scale, this allows for testing of a few candidate compositions at once, a single composition at several time points, or a single composition and time with many replicates.

A diagram of this steady flow setup is presented in Figure 1.17(A). Fluid moved by the pump flowed into the top of a compliance chamber where it was allowed to settle and flow smoothly out of an outlet at the bottom. The compliance chamber served to both aerate the solution and mitigate the "pulsing" effect of the peristaltic pump. The bottom outlet of the compliance chamber was connected to the inlet of the parallel plate flow chamber. Details regarding the design and construction of the parallel plate flow chamber are presented in the Appendix. The fluid then flowed over the fibrin-encapsulated sample, as in Figure 1.17 (B), and emptied into a fluid reservoir. DMEM from the reservoir was pulled back into the pump to complete the circuit. Using this setup, the flow chamber was completely separated from the peristaltic pump, which was necessary to achieve laminar flow. At steady state, the volumetric flow rate through the pump was necessarily equal to that of the parallel plate chamber—if the flow rates were unequal, accumulation in one or another chamber would have occurred. Figure 1.17(C) and (D) illustrate the in-incubator configuration (sans the peristaltic pump) and a close-up of the flow chamber assembly, respectively.

Although only preliminary data are available at this point, it appears that the steadily flowing DMEM does not significantly modify the corrosion behavior (in terms of

products and morphologies) relative to the static submersion testing. Mg wires corroded using this technique had similar characteristics as samples produced using the other methods, including corrosion anisotropy typical of wires encapsulated in asymmetric fibrin. It also displayed nonuniform distribution of corrosion products similar to the wire in Figure 1.15. Fe exhibited the same corrosion behavior in this dynamic environment as in the static media. However, unlike the static media where a pit cap was produced around an intact segment of Fe wire, no pit cap was observed in steady flow samples. The reason may be that the flowing media was able to carry away the pit reaction products before they were able to precipitate and form a cap. Strong localized attack still occurred, resulting in *in situ* fracture of the Fe samples after a short time. The rate at which degradation occurs using this system is much accelerated relative to the other methods discussed in this report.

Using this methodology, it is feasible that a complete assessment of the degradation of some candidate materials could be completed within a week with several replicates at each desired time point. This method would also move farther away from an absolute corrosion rate; comparison to *in vivo* data (or *in vitro* data using a refined encapsulation method) as "calibration" points would be necessary to translate the results into a real, arterial degradation rate. Large-scale experimentation with the steady flow system has not yet been done by the authors, but this system could easily be implemented in an industrial or academic laboratory setting with minimal capital investment.

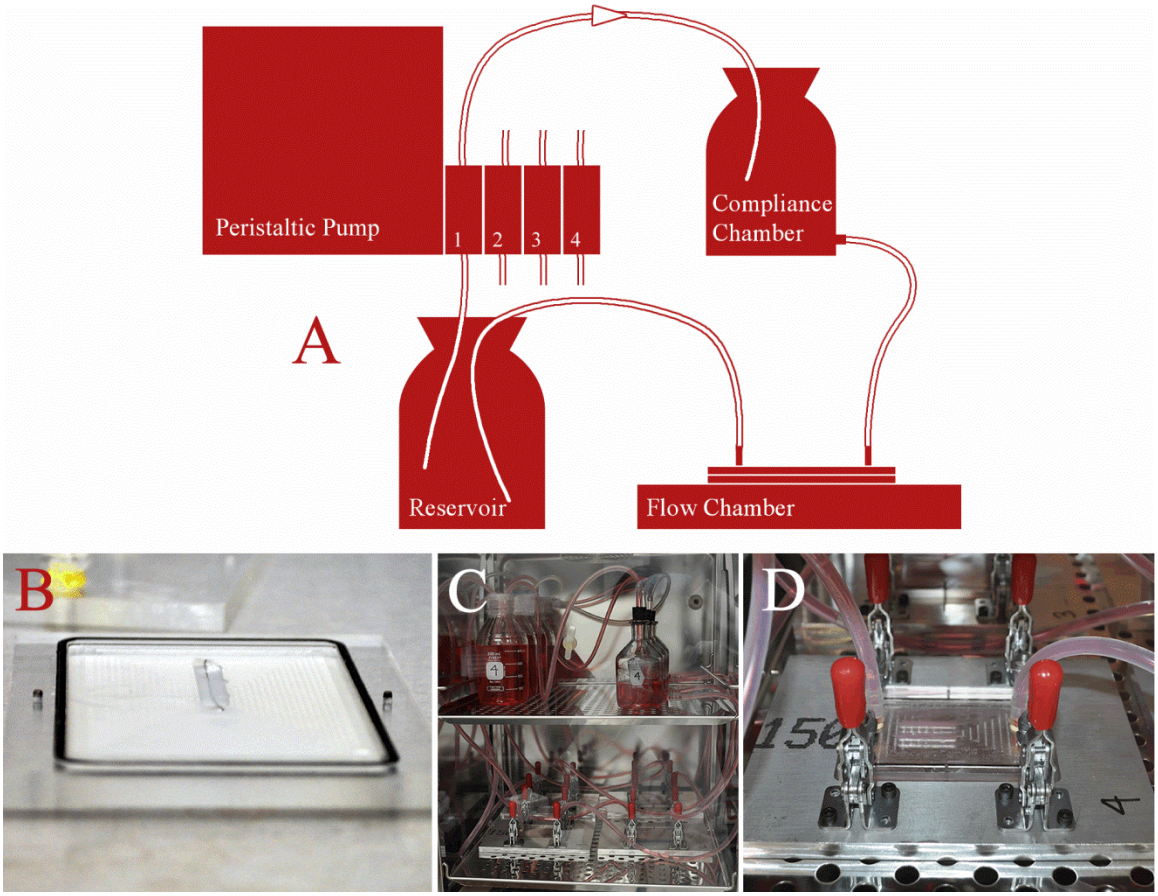

Figure 1.17 – Operation of the steady flow setup used to accelerate *in vitro* degradation: a schematic showing the flow direction for a single circuit (A); a wire encapsulated by fibrin in the bottom half of the flow chamber prior to experimentation (B); the inside of the incubator housing all parts of the circuit except for the peristaltic pump (C); and a close-up image of the steady flow chamber with the flow direction to the left (D).

1.2.4 Qualitative Testing Results

In this particular corrosion system, one may glean a significant amount of information from simple stereomicroscopic examination. The color of the corrosion products, the morphology of secondary and tertiary products, and any localized diametral variations carry information about corrosion progression. This crucial information is neglected by many investigators in the field of bioabsorbable materials, but is widely utilized by

corrosionists.[63] Figure 1.18 presents several examples of Mg wires corroded using the methods described above, in addition to results from the more conventional bare-wire submersion method. It is apparent from Figure 1.18 that a well-defined pattern applies to the corrosion of Mg wires. Fe degradation is not discussed in this section, as the nature of degradation has already been addressed and there is no significant change in sample appearance from one time point to another. Fe wires simply begin to exhibit more severe pitting behavior as the corrosion time increases.

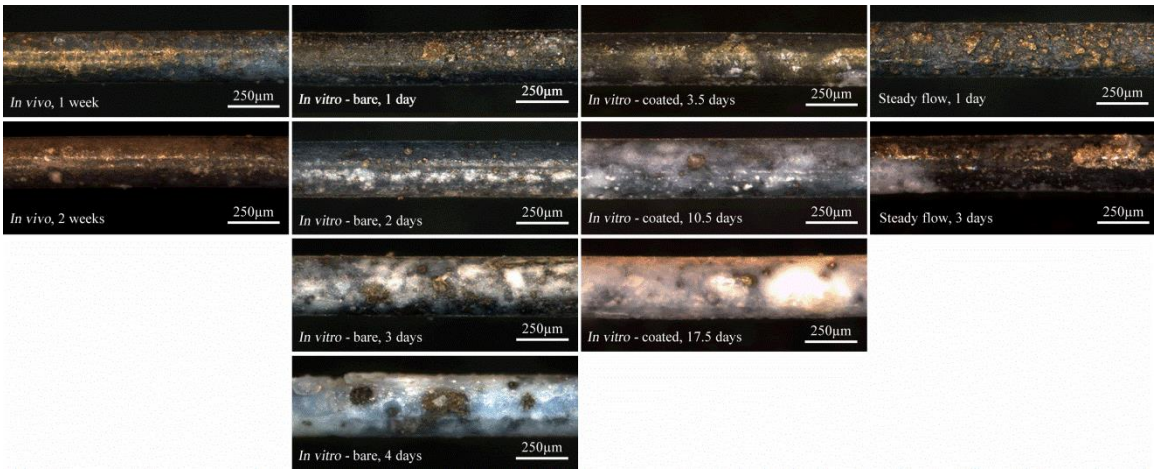

Figure 1.18 – Stereomicrographic images of Mg wires subjected to the environments discussed for different amounts of time. From left to right, the samples were subjected to *in vivo* corrosion, *in vitro* corrosion without a fibrin coating, *in vitro* corrosion with a fibrin coating, and *in vitro* corrosion in the parallel plate flow chamber. Corrosion time increases going down each column.

In general, the Mg degradation products appear to begin as a thin, coherent gray/blue layer. Soon after, a secondary golden-brown layer forms on the initial gray/blue film. The brown layer appears to spread over the wire surface in the *in vivo* and steady flow cases, but remains localized in "islands" in both *in vitro* cases, probably because of some

transport-related phenomenon. Nevertheless, it is clearly present in both instances. Finally, a white, tertiary product begins to form on the brown and/or gray/blue layer. The white layer is barely visible at the end of 2 weeks *in vivo* and appears relatively late in steady flow, but is pronounced earlier in *in vitro* tests with static media. Thickening of the white layer appears to be the terminal corrosion stage in the extended *in vitro* studies. The layer itself becomes brittle and begins to chip away, and, as the cross-sectional area of the Mg core reduces further and further, the wires take on a brittle mechanical character. At very late stages of corrosion, the wires are extremely difficult to handle and only remain intact in the *in vitro* scenarios where static media is used. Fragmentation of the wires is observed *in vivo* and in the steady flow case after the white layer becomes dominant, precluding detailed assessment of failure in those cases. At extremely long times (many weeks) in static DMEM—after the Mg core has been completely dissolved and the other corrosion products apparently transform into the white product—the corrosion product remains intact but is readily broken apart by the smallest disturbance of the media. It could be argued, based on these results, that the mode of failure (dominance of a uniform brittle phase cracked by minute stresses) is likely to be the same in both static *in vitro* and *in vivo*/steady flow cases.

1.2.5 Quantification of Metal Degradation Rate

As work in this area progresses, it is desirable to develop and fully characterize a single quantitative method for the evaluation of bioabsorbable candidate materials. To date, studies of Mg corrosion have relied on quantitative techniques such as monitoring the

changes in sample mass,[66–68] current density (or other electrochemical techniques),[42,69] and/or the volume of evolved hydrogen.[24,70] X-ray tomographic analysis has been conducted on some bioabsorbable samples explanted from animals, though the application to date has been limited to orthopedic specimens.[34] These quantitative techniques have their own strengths and weaknesses and provide valuable information about Mg degradation, but some are simply not feasible for use in bioabsorbable material systems. For example, the simple mass gain/loss method is difficult to apply to our *in vivo* approach, since explanted wires retain significant amounts of tissue,[54] which hinders estimation of the mass preceding removal of the corrosion product. The largest single drawback, common to all of these techniques, is the difficulty in applying data generated from any of these techniques directly to stent design.

In application, the single most important aspect of a stent is that is must act as vascular scaffolding until repair is complete, and its effectiveness as scaffolding is largely dictated by its mechanical behavior. Consequently, it is advantageous to know precisely how the mechanical properties of a given material change (decrease) over time. If a mechanical degradation profile is well known, then a material can be specified to have a specific fractional strength at any point during its lifetime—e.g. 50% of the nominal strength is retained after degradation over 6 months. To be practically helpful, data gleaned from the characterization method must account for the effects of uniform corrosion (cross sectional area reduction) as well as localized attack in the form of pits and/or crevices. To this end, a method of tensile testing wires similar to that used to evaluate polymeric

nanofibers[71] has been developed. The method was developed to characterize the mechanical profile of materials over their corrosion lifetimes with strong statistical significance.[61] The technique is easily used in conjunction with *in vitro* and *in vivo* corrosion methods described above and works well with wire sample geometry.

To accomplish this, the corroded wires are mounted to two pieces of polycarbonate substrate using general-purpose epoxy. A "gauge length" is established by maintaining a precise distance between the substrate pieces. Toothpicks (or some other support) are taped to the back of the polycarbonate in order to support the relatively fragile wires. A schematic of the tensile assembly is presented in Figure 1.19, showing its construction before testing is performed. Mechanical testing is conducted by gripping the two polycarbonate pieces, clipping the toothpicks, and running the test. The authors use a small tensile frame—a Test Resources 100-series instrument—with wide soft tissue grips and a 250 lbf (~1 kN) load cell, although smaller load cells can be used depending on the material being tested.

The data generated by this test is in the form of load/elongation. However, to be instructive in an engineering analysis, the data is better presented in a stress/strain configuration. The strain is simply calculated by the elongation divided by the nominal gauge length, 10 mm. Calculation of the stress in the "raw," or uncorroded, wire is also trivial, as it is the load divided by the nominal cross sectional area. Calculation of the real stress in the corroded wires, on the other hand, is a complex proposition. This is due to the unknown cross section at the point of failure resulting from the invariable presence

of changes in uniform corrosion severity, pits, and crevices. Hence, the true stress is not calculated for the corroded wires, but rather an "effective" stress is calculated using the same nominal cross sectional area as the "raw" wire calculation. Typical mechanical behavior of a severely corroded Mg specimen is contrasted with that of an as-received wire sample in Figure 1.19. This particular sample had been corroded for 3 weeks with a fibrin coating in DMEM under cell culture conditions and has a significantly reduced effective tensile strength and total elongation (> 60% and > 80% decreases, respectively).

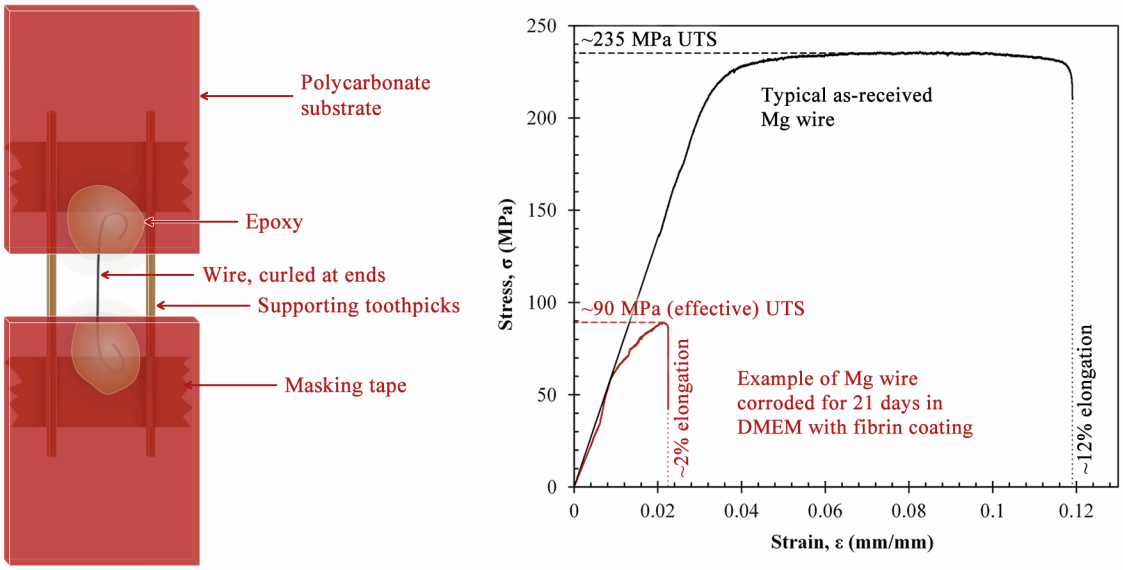

Figure 1.19 – Schematic of the tensile samples used in this study (left) and an example of a "raw," or uncorroded, Mg wire compared to a severely corroded Mg wire (right). The tensile curves on the right illustrate the drastic reduction in ductility, elongation at failure, and tensile strength after corrosion of fibrin-encapsulated wires in DMEM for three weeks.

When the mechanical behavior data were aggregated, the ultimate (or "effective ultimate") tensile strength was selected for evaluation because of its good reproducibility from sample-to-sample. Other variables, such as compliance, Young's modulus, and

0.2% offset yield strength all showed larger scatter, although they also would provide some information about corrosion progression. Another reason for selecting the effective tensile strength is that, using the assumption stated previously, the ratio of the strength of a corroded wire to that of an as-received wire gives a rough estimate of the cross sectional area reduction at the point of failure. It should be noted, though, that this extension of the tensile testing method requires the assumption that the contribution of localized corrosion was negligible.

In both Mg and Fe, the mechanical data showed a considerable amount of variability, but a generally decreasing tensile strength trend was apparent for both materials. The data, plotted as a function of corrosion time for all methods (*in vitro* steady flow, *in vitro* static with and without fibrin, and *in vivo*), are presented in Figure 1.20. The statistical nature of these data is discussed in the authors' previous work,[61] so the discussion here is limited to trends and preliminary data that have not yet been reported.

The Mg data show a clear downward trend with some methods resulting in considerably more scatter than others do. First comparing the static *in vitro* techniques, the rate of decrease of the effective tensile strength in the uncoated samples is clearly greater than the rate of decrease in the fibrin-coated samples. This observation stands to reason; mass transport will occur at a reduced rate in the system containing the fibrin-coated sample, thus reducing the corrosion rate. In addition to this, the scatter in the fibrin-coated sample data is quite large, owing to nonuniform distribution of fibrin around the wire and/or defects in some fibrin sheaths.

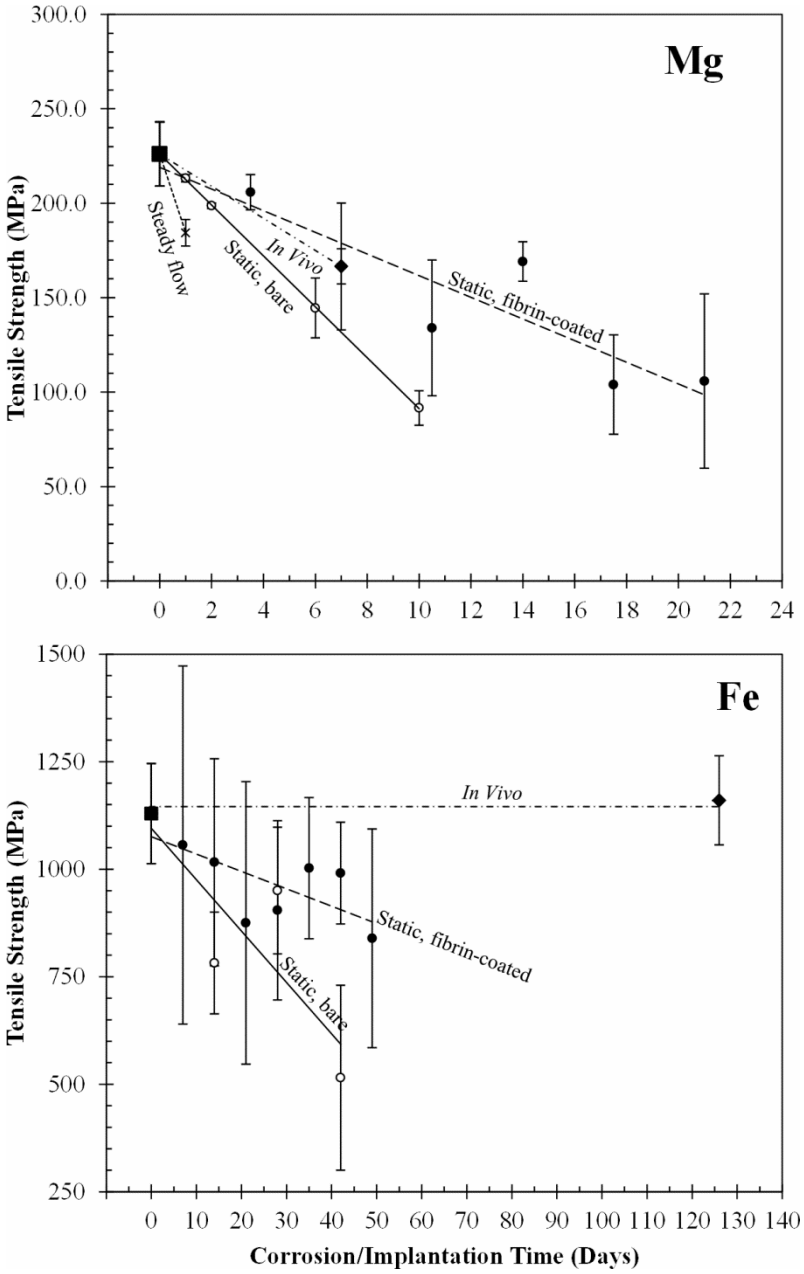

Figure 1.20 – Complete tensile strength data for Mg (top) and Fe (bottom) showing the degradation rates for wires corroded *in vivo*, *in vitro* in DMEM with and without a fibrin coating, and in the *in vitro* steady flow configuration.

It is noteworthy, also, that the single, preliminary *in vivo* data point lies remarkably close to the static *in vitro* trendline for samples that employed a fibrin coating. This single data

point is not conclusive and has a large associated error, but it is safe to say that the degradation behavior of the coated is trending in the right direction relative to the bare wire data. An additional preliminary data point for wires corroded for one day using the *in vitro* steady flow method is presented for Mg. In a situation similar and opposite to that previously stated, the enhanced transport due to flowing media appears to accelerate corrosion, although more data are needed before conclusions can be drawn.

The Fe data exhibit a comparatively large amount of scatter at each time point, indicative of pseudo-random, nonuniform corrosion events leading to failure. In most cases, the initially passive (Ca- and P-containing) film was disrupted by the evolution of a voluminous product identified as hematite,[54] as in the rodent arterial explants. The same relationship between the uncoated static wires and those with a fibrin sheath is observed in both materials. As before, the bare wires were observed to degrade at a much faster rate. In the case of Fe, however, no significant change in the tensile strength was observed even after 4.5 months of time spent in the arterial wall. Samples were also evaluated in tension after 1.5 and 3 months of implantation, but those surface coatings of the wires—possibly a passive layer—caused them to separate from the epoxy at relatively low loads, resulting in no valid tensile stress data. To replicate the *in vivo* behavior *in vitro*, then, a higher-concentration fibrin coating or alternative coating method would be required. Regardless, the negligible amount of degradation in the Fe wires coupled with the voluminous corrosion product observed *in vivo* collectively prove that Fe is a poor choice for bioabsorbable implants.

1.2.6 Conclusions

In vivo evaluation using the rodent arterial implant model, *in vitro* evaluation using fibrin-coated samples in static DMEM, an *in vitro* steady flow method, and quantitative tensile evaluation are all viable methods for evaluating bioabsorbable materials, such as Fe, Mg, and Mg alloys.

In vivo, implantation of Mg wires in the arterial wall leads to well-behaved, typically uniform degradation, while implantation of Fe wires leads to the evolution and retention of a voluminous corrosion product. The *in vivo* technique developed is also useful in evaluating candidate materials and biological processes, as shown in the candidate material degradation and OCP-stripping examples. The measured degradation rate of a candidate alloy (A9) was shown to be reasonable for physiological corrosion, and the elemental makeup of the corrosion products was shown to be consistent with previously published data.

The *in vitro* techniques were shown to provide valuable information related to the degradation behavior of bioabsorbable Mg, and a significant amount of information about the corrosion progression was gleaned from stereomicrographs. The bare wire control method, when DMEM was used as the corrosion medium, appeared to replicate the corrosion products observed *in vivo*. When a fibrin coating was introduced to the system, degradation was observed to slow significantly, closer to the *in vivo* corrosion rate. This is likely due to restricted mass transport between the wire and the surroundings. Finally,

steadily flowing media was introduced to the system, which appears to replicate the corrosion products and morphology of samples corroded using the rodent arterial implantation model. The flowing media appeared to increase the corrosion rate due to enhanced mass transport, even to the point of causing *in situ* fracture of Fe samples.

To quantitatively evaluate the wires, it was shown that a tensile testing method consistently produced a degradation profile for both Fe and Mg. The profile for Mg appeared to have less scatter at each time point, and the preliminary tensile data for *in vivo* degradation of Mg were in good agreement with data corresponding to *in vitro* degradation of fibrin-coated Mg wires. The qualitative observation that fibrin-coated wires degraded more slowly than their bare counterparts was supported by the quantitative data. Fe, on the other hand, exhibited a large amount of scatter within each time point. The same decrease in the rate of degradation of fibrin-coated wires relative to bare wires was observed for Fe, but the *in vivo* corrosion rate was apparently much lower than that of the fibrin-coated wires for this material. Most importantly, though, this quantitative evaluation technique works seamlessly with all the corrosion methods presented, completing a "suite" of corrosion techniques useful in bioabsorbable material studies.

1.2.7 Appendix—Details of experimentation

1.2.7.1 Fibrin encapsulation for static submersion

A mold was machined which had several rectangular grooves, each 30 mm long, 5 mm wide, and 3 mm deep. A method for suspending the wires above the bottom of the large

mold slots was needed; 0.3 mm deep semicircular grooves were added to each long end of the large grooves. The bottom and sides of the grooves were covered with Parafilm to prevent adhesion of the polymerized fibrin to the mold walls. 30–34 mm wires were then positioned such that equal lengths on each end were supported by the shallow grooves. Then, fibrinogen (100 mg/mL) and thrombin (2.5 U/mL) solutions were added in equal amounts to each groove containing the wires, and the entire mold was placed in an incubator to allow the fibrinogen/thrombin mixture to polymerize and form a fibrin sheath. After polymerization was complete, the fibrin-coated wires were removed from the mold and submerged in DMEM under cell culture conditions. Recently published work[61] presents a more complete protocol as well as data acquired using this methodology in contrast to data from submersion of bare wires.

1.2.7.2 Flow chamber design and construction

The parallel plate flow chamber was designed to subject wires to a shear stress representative of the arterial environment. Published ranges for arterial shear stresses were approximately 1-3 Pa,[72,73] so a target value of 2 Pa was chosen for the chamber design. Using the design methodology of Reyes[74] and assuming a value of 0.78 mPa·s for DMEM viscosity, a plate separation of 300 μm, and width of 5 cm, a flow rate of 115.4 mL/min was calculated to obtain the desired shear stress. The steady flow system utilized a peristaltic pump with an adjustable flow rate, which was set to the desired 115 mL/min. Further review of the literature suggested that the blood flow through coronary arteries could be modeled as laminar flow, meaning a Reynolds number less than 2100

was appropriate.[75] To achieve laminar flow, then, required a minimum entrance length of 9 mm.[74]

With these design parameters under consideration, a parallel plate flow chamber was designed and fabricated using polycarbonate for the base plates (Lancet Glass; Houghton, MI). A seal was achieved by using a 1/8 in (3.18 mm) standard O-ring (McMaster-Carr; Robbinsville, NJ) inset in symmetric 0.3 mm deep grooves on each base plate. The inlet and outlet holes were positioned on the top plate such that the entrance length was 26 mm, which provided a factor of safety of approximately three relative to the minimum length required for laminar flow. The inlet and outlet were polycarbonate tube connectors (McMaster-Carr) which connected to silicone tubing (Cole-Palmer; Vernon Hills, IL). The bottom plate had a 40 mm slot machined into it with 0.5 mm grooves on each side, which allowed the fibrin casting/wire encapsulation to be performed *in situ*. The assembly was held together by four hold-down toggle clamps (McMaster-Carr) attached to an aluminum base plate.

1.2.8 Acknowledgments

The authors would like to express appreciation to Jon Stinson, Heather Getty and Jake Edick of Boston Scientific in Plymouth, MN for several inspirational discussions that led to this project. The authors are also grateful to Dr. Mark Cunningham of Surpass, Inc. for the information on large animal models for stent evaluation. The authors would also like to thank Jesse Gelbaugh, Jessica Rhadigan (Forrest), Ellen Pokorney, Bryne Judy, and Becky Franke for their input in designing the corrosion protocol used in this

experimentation and for assisting with other tasks. Thanks, also, to Mike LaBeau for his assistance in learning and operating the tensile testing equipment, to Connor McCarthy for his help with lab protocol and troubleshooting, and to Cam McNamara for his time spent editing and proofreading. Boston Scientific is acknowledged for providing partial financial support for the early stages of this project.

1.2.9 References

1. Fischman, D. L.; Leon M.B.; Baim D.S.; Schatz R.A.; Savage M.P.; Penn I.; Detre K.; Veltri L.; Ricci D.; Nobuyoshi M.; Cleman M.; Heuser R.; Almond D.; Teirstein P.S.; Fish R.D.; Colombo A.; Brinker J.; Moses J.; Shaknovich A.; Hirshfeld J.; Bailey S.; Ellis S.; Rake R.; Goldberg S. A randomized comparison of coronary-stent placement and balloon angioplasty in the treatment of coronary artery disease, *New. Engl. J. Med*. **1994**, *331*, 496-501.
2. Eleizi, S.; Kastrati A.; Neumann FJ.; Hadamitzky M.; Dirschinger J.; Schomig A. Vessel size and long-term outcome after coronary stent placement, *Circulation*. **1998**, *98*, 1875-1880.
3. Farb, A.; Weber D.K.; Kolodgie F.D.; Burke A.P.; Virmani R. Morphological predictors of restenosis after coronary stenting in humans, *Circulation*. **2002**, *105*, 2974-2980.
4. Cook, S.; Wenaweser P.; Togni M.; Billinger M.; Morger C.; Seiler C.; Vogel R.; Hess O.; Meier B.; Windecker S. Incomplete stent apposition and very late stent thrombosis after drug-eluting stent implantation, *Circulation*. **2007**, *115*, 2426-2434.
5. Chung, WS.; Park CS.; Seung KB.; Kim PJ.; Lee JM.; Koo BK.; Jang YS.; Yang JY.; Yoon JH.; Kim DI.; Yoon YW.; Park JS.; Cho YH.; Park SJ. The incidence and clinical impact of stent strut fractures developed after drug-eluting stent implantation, *Int. J. Cardiol*. **2008**, *125*(3), 325-331.

6. O'Connell, B. M.; McGloughlin T.M.; Walsh M.T. Factors that affect mass transport from drug eluting stents into the artery wall, *Biomed. Eng. Online*. **2010**, *9*.
7. Kastrati, A.; Schomig A.; Elezi S.; Schuhlen H.; Dirschinger J.; Hadamitzky M.; Wehinger A.; Hausleiter J.; Walter H.; Neumann FJ. Predictive factors of restenosis after coronary stent placement, *J. Am. Coll. Cardiol*. **1997**, *30*(6), 1428-1436.
8. Baber, U.; Mehran R.; Sharma S.K.; Brar S.; Yu J.; Suh J.W.; Kim H.S.; Park S.J.; Kastrati A.; DeWaha A.; Krishan P.; Moreno P.; Sweeny J.; Kim M.C.; Suleman J.; Pyo R.; Wiley J.; Kovacic J.; Kini A.S.; Dangas G.D. Impact of the Everolimus-eluting stent on stent thrombosis: a meta-analysis of 13 randomized trials, *J. Am. Coll. Cardiol*. **2011**, *58*(15), 1569-1577.
9. Waksman, R. Biodegradable stents: they do their job and disappear, *Catheter. Cardio. Interv.* **2006**, 18(2), 70-75.
10. Onuma, Y.; Ormiston J.; Serruys P. Bioresorbable scaffold technologies, *Circ. J.* **2011**, *75*, 509-520.
11. Waksman, R.; Pakala R.; Kuchulakanti P.; Baffour R.; Hellinga D.; Seabron R.; Tio F.; Wittchow E.; Hartwig S.; Harder C.; Rohde R.; Heublein B.; Andreae A.; Waldmann K.; Haverich A. Safety and efficacy of bioabsorbable magnesium alloy stents in porcine coronary arteries, *Catheter. Cardio. Interv.* **2006**, *68*, 607-617.
12. Tamai, H.; Igaki K.; Tsuji T.; Kyo E.; Kosuga K.; Kawashima A.; Matsui S.; Komori H.; Motohara S.; Uehata H.; Takeuchi E. A biodegradable poly-l-lactic acid coronary stent in the porcine coronary artery, *J. Interv. Cardiol.* **1999**, *12*(6), 443-449.
13. Bunger, C. M.; Grabow N.; Sternberg K.; Goosmann M.; Schmitz K.P.; Kreutzer H.J.; Ince H.; Kische S.; Nienaber C.A.; Martin D.P.; Williams S.F.; Klar E.; Schareck W. A biodegradable stent based on poly(L-lactide) and poly(4-hydroxybutyrate) application: Preliminary for peripheral vascular experience in the pig, *J. Endovasc. Ther.* **2007**, *14*(5), 725-733.

14. Grabow, N.; Bunger C.M.; Schultze C.; Schmohl K.; Martin D.P.; Williams S.F.; Sternberg K.; Schmitz K.P. A biodegradable slotted tube stent based on Poly(L-lactide) and poly(4-hydroxybutyrate) for rapid balloon-expansion, *Ann. Biomed. Eng.* **2007**, *35*(12), 2031-2038.
15. Mario, C.; Griffiths H.; Goktekin O.; Peeters N.; Verbist J.; Bosiers M.; Deloose K.; Heublein B.; Rohde R.; Kasese V.; Ilsley C.; Erbel R. Drug-eluting bioabsorbable magnesium stent, *J. Interv. Cardiol.* **2004**, *17*(6), 391-395.
16. Wang, H.; Estrin Y.; Zuberova Z. Bio-corrosion of a magnesium alloy with different processing histories, *Mater. Lett.* **2008**, *62*, 2476-2479.
17. Saris, N.; Mervaala E.; Karppanen H.; Khawaja J.; Lewenstam A. Magnesium: an update on physiological, clinical and analytical aspects, *Clin. Chim. Acta.* **2000**, *294*, 1-26.
18. Moravej, M.; Mantovani D. Biodegradable metals for cardiovascular stent application: interests and new opportunities, *Int. J. Mol. Sci.* **2011**, *12*, 4250-4270.
19. Zhu, S.; Huang N.; Xu L.; Zhang Y.; Liu H.; Sun H.; Leng Y. Biocompatibility of pure iron: *in vitro* assessment of degradation kinetics and cytotoxicity on endothelial cells, *Mater. Sci. Eng. C.* S. **2009**, *29*, 1589-1592.
20. Peuster, M.; Hesse C.; Schloo T.; Fink C.; Beerbaum P.; von Schnakenburg C. Long-term biocompatibility of a corrodible peripheral iron stent in the porcine descending aorta, *Biomaterials*. **2006**, *27*, 4955-4962.
21. Brandes EA, editor. *Smithells Metals Reference Book*. 6th edn. London: Butterworth & Co. 1983.
22. Daniels, A. U.; Chang M.KO.; Andriano K.P.; Heller J. Mechanical properties of biodegradable polymers and composites proposed for internal fixation of bone, *J. Appl. Biomater.* **1990**, *1*(1), 57-78.
23. Geis-Gerstorfer, J.; Schille C.; Schweizer E.; Rupp F.; Scheideler L.; Reichel HP.; Hort N.; Nolte A.; Wendel HP. Blood triggered corrosion of magnesium alloys, *Mater. Sci. Eng. B.* **2011**, *176*, 1761-1766.

24. Gu, X.; Zheng Y.; Cheng Y.; Zhong S.; Xi T. *In vitro* corrosion and biocompatibility of binary magnesium alloys, *Biomaterials*. **2009**, *30*, 484-498.
25. Liu, L. J.; Schlesinger M. Corrosion of magnesium and its alloys, *Corros. Sci.* **2009**, *51*, 1733-1737.
26. Zhang, E.; Chen H.; Shen F. Biocorrosion properties and blood and cell compatibility of pure iron as a biodegradable biomaterial, *J. Mater. Sci. Mater. M.* **2010**, *21*, 2151-2163.
27. Yang, L.; Zhang E. Biocorrosion behavior of magnesium alloy in different simulated fluids for biomedical application, *Mater. Sci. Eng. C.* S. **2009**, *29*, 1691-1696.
28. Ghali, E.; Revie R.W. *Corrosion Resistance of Aluminum and Magnesium Alloys: Understanding, Performance, and Testing*. Hoboken: Wiley, 2010.
29. Pu, Z.; Puleo D.; Dillon O.; Jawahir L. Controlling the biodegradation rate of magnesium-based implants through surface nanocrystallization induced by cryogenic machining. In: *Magnesium Technology 2011*. Sillekens W.; Agnew S.; Neelameggham N.; Mathaudhu S., eds. Warrendale, PA: Wiley-TMS **2011**, 409-412.
30. Virtanen, S.; Fabry B. Corrosion, surface modification, and biocompatibility of Mg and Mg alloys. In: *Magnesium Technology 2011*. Sillekens W.; Agnew S.; Neelameggham N.; Mathaudhu S., eds. Warrendale, PA: Wiley-TMS **2011**, 409-412.
31. Witte, F. ; Hort N.; Feyerabend F.; Vogt C. Magnesium (Mg) corrosion: a challenging concept for degradable implants. In: *Corrosion of Magnesium Alloys*. Song, G.L., ed. Philadelphia: Woodhead **2011**, 416-417.
32. Kainer K.U., ed. *Magnesium - Alloys and Technologies*. Weinheim: Wiley-VCH **2003**.
33. Witte, F.; Hort N.; Vogt C.; Cohen S.; Kainer K.; Willumeit R.; Feyerabend F. Degradable biomaterials based on magnesium corrosion, *Curr. Opin. Solid State Mater.* **2008**, *12*, 63-72.

34. Witte, F.; Fischer J.; Nellesen J.; Crostack H.A.; Kaese V.; Pisch A.; Beckmann F.; Windhagen H. *In vitro* and *in vivo* corrosion measurements of magnesium alloys, *Biomaterials* **2006**, *27*, 1013-1018.
35. Atrens, A.; Liu M.; Abidin N.I.Z. Corrosion mechanism applicable to biodegradable magnesium implants, *Mater. Sci. Eng. B.* **2011**, *176*, 1609-1636.
36. Hoffmann, I.; Cheng YT.; Puleo D.A.; Song G.; Waldo R.A. Mg-Ti: A possible biodegradable, biocompatible, mechanically matched material for temporary implants, *Mater. Res. Soc. Symp. Proc.* **2011**, 1301.
37. Gray, J. E.; Luan B. Protective coatings on magnesium and its alloys - a critical review, *J. Alloy Compd.* **2002**, 336, 88-113.
38. El-Rahman, S. SA. Neuropathology of aluminum toxicity in rats (glutamate and GABA impairment), *Pharmacol. Res.* **2003**, *47*, 189-194.
39. Kumar, V.; Gill K.D. Aluminium neurotoxicity: neurobehavioural and oxidative aspects, *Arch. Toxicol.* **2009**, *83*, 965-978.
40. Gitelman, H. J. Aluminum exposure and excretion, *Sci. Total Environ.* **1995**, *163*, 129-135.
41. Sjogren, B.; Lidums V.; Hakansson M.; Hedstrom L. Exposure and urinary excretion of aluminum during welding, *Scand. J. Work Environ. Health.* **1985**, *11*, 39-43.
42. Xin, Y.; Huo K.; Tao H.; Tang G.; Chu P.K. Influence of aggressive ions on the degradation behavior of biomedical magnesium alloy in physiological environment, *Acta Biomater.* **2008**, *4*, 2008-2015.
43. Willumeit, R.; Fischer J.; Feyerabend F.; Hort N.; Bismayer U.; Heidrich S.; Mihailova B. Chemical surface alteration of biodegradeable magnesium exposed to corrosion media, *Acta Biomater.* **2011**, 7, 2704-2715.
44. Müller, W. D.; Nascimento M.L.; De Mele M.FL. Critical discussion of the results from different corrosion studies of Mg and Mg alloys for biomaterial applications, *Acta Biomater.* **2010**, *6*, 1749-1755.

45. Hermawan, H.; Alamdari H.; Mantovani D.; Dube D. Iron-manganese: new class of metallic degradable biomaterials prepared by powder metallurgy, *Powder Metall.* **2008**, *58*(1), 38-45.

46. Hermawan, H.; Purnama A.; Dube D.; Couet J.; Mantovani D. Fe-Mn alloys for metallic biodegradable stents: degradation and cell viability studies, *Acta Biomater.* **2010**, *6*, 1852-1860.

47. Seitz, JM.; Wulf E.; Freytag P.; Bormann D.; Bach FW. The manufacture of resorbable suture material from magnesium, *Adv. Eng. Mater.* **2010**, *12*(11), 1099-1105.

48. Seitz, JM.; Utermohlen D.; Wulf E.; Klose C.; Bach FW. The manufacture of resorbable suture material from magnesium - drawing and stranding of thin wires, *Adv. Eng. Mater.* **2011**, *13*(12), 1087-1095.

49. Zberg, B.; Uggowitzer P.J.; Loffler J.F. MgZnCa glasses without clinically observable hydrogen evolution for biodegradable implants, *Nat. Mater.* **2009**, *8*, 887-891.

50. Cunningham, M. R. Private communication. March 2012.

51. Li, Z.; Gu X.; Lou S.; Zheng Y. The development of binary Mg-Ca alloys for use as biodegradable materials within bone, *Biomaterials* **2008**, *29*, 1329-1344.

52. Xu, L.; Yu G.; Zhang E.; Pan F.; Yang K. *In vivo* corrosion behavior of Mg-Mn-Zn alloy for bone implant application, *J. Biomed. Mater. Res. A.* **2007**, *83A*(3), 703-711.

53. Heublein, B.; Rohde R.; Kaese V.; Niemeyer M.; Hartung W.; Haverich A. Biocorrosion of magnesium alloys: a new principle in cardiovascular implant technology, *Heart.* **2003**, *89*, 391-395.

54. Pierson, D.; Edick J.; Tauscher A.; Pokorney E.; Bowen P.; Gelbaugh J.; Stinson J.; Getty H.; Lee C.H.; Drelich J.; Goldman J. A novel *in vivo* approach for evaluating the bioabsorbable behavior of candidate stent materials, *J. Biomed. Mater. Res. B.* **2011**, *100B*(1), 58-67.

55. Makar, G. L.; Kruger J. Corrosion of magnesium, *Int. Mater. Rev.* **1993**, *38*(3), 138-153.

56. Emley, E. F. *Principles of Magnesium Technology*. Oxford: Pergamon Press, 1966.
57. Baril, G.; Pébère N. The corrosion of pure magnesium in aerated and deaerated sodium sulphate solutions, *Corros. Sci.* **2001**, *43*(3), 471-484.
58. Witte, F.; Fischer J.; Nellesen J.; Vogt C.; Vogt J.; Donath T.; Beckmann F. *In vivo* corrosion and corrosion protection of magnesium alloy LAE442, *Acta Biomater*. **2010**, *6*, 1792-1799.
59. Witte, F.; Feyerabend F.; Maier P.; Fischer J.; Stormer M.; Blawert C.; Dietzel W.; Hort N. Biodegradable magnesium-hydroxyapatite metal matrix composites, *Biomaterials*. **2007**, *28*, 2163-2174.
60. Schille, C.; Braun M.; Wendel H.P.; Scheideler L.; Hort N.; Reichel HP.; Schweizer E. Corrosion of experimental magnesium alloys in blood and PBS: A gravimetric and microscopic evaluation, *Mater. Sci. Eng. B.* **2011**, *176*, 1797-1801.
61. Bowen, P. K.; Gelbaugh J.A.; Mercier P.J.; Goldman J.; Drelich J. Tensile testing as a novel method for quantitatively evaluating bioabsorbable material degradation, *J. Biomed. Mater. Res. B* **2012**, *100B*(8), 2101-2113.
62. Xin, Y.; Huo K.; Hu T.; Tang G.; Chu P. Corrosion products on biomedical magnesium alloy soaked in simulated body fluids, *J. Mater. Res.* **2009**, *24*(8), 2711-2719.
63. Jones, D. A. *Principles and prevention of corrosion.* 2nd edn. Upper Saddle River: Prentice Hall, 1996.
64. Waksman, R.; Pakala R.; Baffour R.; Seabron R.; Hellinga D.; Tio F.O. Short-term effects of biocorrodible iron stents in porcine coronary arteries, *J. Interv. Cardiol.* **2008**, *21*(1), 15-20.
65. MacDonald, D. D. The point defect model for the passive state, *J. Electrochem. Soc.* **1992**, *139*(12), 3434-3449.

66. Seitz, J. M.; Collier K.; Wulf E.; Bormann D.; Bach F.W. Comparison of the corrosion behavior of coated and uncoated magnesium alloys in an *in vitro* corrosion environment, *Adv. Eng. Mater.* **2011**, *13*(9), B313-B323.

67. Xu, X. Y.; Liu T.; Zhang K.; Liu S.H.; Shen Z.; Li Y.X.; Jing X.B. Biodegradation of poly(L-lactide-co-glycolide) tube stents in bile, *Polym. Degrad. Stabil.* **2008**, *93*(4), 811-817.

68. Xin, Y.; Liu C.; Zhang X.; Tang G.; Tian X.; Chu P.K. Corrosion behavior of biomedical AZ91 magnesium alloy in simulated body fluids, *J. Mater. Res.* **2007**, *22*(7), 2004-2011.

69. Müller, W. D.; Nascimento M.L.; Zeddies M.; Córsico M. Magnesium and its alloys as degradable biomaterials: corrosion studies using potentiodynamic and EIS electrochemical techniques, *J. Mater. Res.* **2007**, *10*(1), 5-10.

70. Song, G.; Atrens A.; St. John D. An hydrogen evolution method for the estimation of the corrosion rate of magnesium alloys. In: *Magnesium Technology 2001*, Hryn J., ed. Warrendale, PA: Wiley-TMS **2001**, 255-262.

71. Bazbouz, M. B.; Stylios G.K. The tensile properties of electrospun nylon 6 single nanofibers, *J. Polym. Sci. Pol. Phys.* **2010**, *48*, 1719-1731.

72. Kroll, M.; Hellums J.; McIntire L.; Schafer A.; Moake J. Platelets and shear stress, *Blood*. **1996**, *88*(5), 1525-1541.

73. Bacabac, R. ; Smit T.; Cowin S.; Van Loon J.; Nieuwstadt F.; Heethaar R.; Klein-Nulend J. Dynamic shear stress in parallel-plate flow chambers, *J. Biomech.* **2005**, *38*, 159-167.

74. Reyes, E. A. *Flow chamber for studying cell attachment to opaque substrates*. University of Florida, Gainesville, 2004, MS Thesis.

75. Lévesque, J.; Hermawan H.; Dubé D.; Mantovani D. Design of a pseudo-physiological test bench specific to the development of biodegradable metallic biomaterials, *Acta Biomater.* **2008**, *4*(2), 284-295.

2 Evaluation and correlation of corrosion rates

2.1 A new *in vitro-in vivo* correlation for bioabsorbable magnesium stents from mechanical behavior[3]

2.1.1 Abstract

Correlating the *in vitro* and *in vivo* degradation of candidate materials for bioabsorbable implants is a subject of interest in the development of next-generation metallic stents. In this study, pure magnesium wire samples were corroded both in the murine artery (*in vivo*) and in static cell culture media (*in vitro*), after which they were subjected to mechanical analysis by tensile testing. Wires corroded *in vivo* showed reductions in strength, elongation, and the work of fracture, with additional qualitative changes between tensile profiles. The *in vivo* degradation was 2.2 ± 0.5, 3.1 ± 0.8, and 2.3 ± 0.3 times slower than corrosion *in vitro* in terms of effective tensile strength, strain to failure, and sample lifetime, respectively. Also, a combined metric, defined as strength multiplied by elongation, was 3.1 ± 0.7 times faster *in vitro* than *in vivo*. Consideration of the utility and restrictions of each metric indicates that the lifetime-based multiplier is the best suited to general use for magnesium, though other metrics could be used to deduce the mechanical properties of degradable implants in service.

---

[3] The material in Section 2.1 was previously published in *Materials Science and Engineering C* and is reproduced here with permission.

P. K. Bowen, J. Drelich, and J. Goldman. "A new *in vitro-in vivo* correlation for bioabsorbable magnesium stents from mechanical behavior." *Mater. Sci. Eng. C* 33(8) 5064-5070 (2013), doi: 10.1016/j.msec.2013.08.042.

References in Section 2.1 follow the *Materials Science and Engineering C* author guidelines.

2.1.2 Introduction

Bioabsorbable endovascular stents have undergone much investigation in recent years [1-3], with recent advances including promising human trials of magnesium scaffolds [4] and the advent of zinc as a viable bioabsorbable stent material [5]. As these devices near clinical reality, the challenge of establishing an *in vivo*-*in vitro* correlation has come to the forefront. At the most basic level, a quantitative multiplier relating bench top tests to animal studies would allow investigators to infer *in vivo* material lifetimes and properties from *in vitro* experiments that are simple, rapid, and systematic in nature. In doing so, the number of required *in vivo* tests and, therefore, the number of sacrificed animals and their associated high costs may be reduced. Such testing has long been recognized to be an unfortunate, but necessary, consequence of device and biomaterial development [6], and improving the use of animal subjects consistent with the "replace, reduce, refine ("3R") doctrine [7] is desirable. One route to reducing animal experimentation is by reliance on computational models, which have been widely used in pursuit of improved permanent stent designs [8]. Specifically, integration of an appropriate multiplier may lend credence to attempts at predictively modeling the behavior of degradable stents *in silico*—an area in which considerable progress has already been made [9-12].

Discrepancies between *in vivo* tests and submersion tests *in vitro* were recognized in some of the earliest bioabsorbable stent work [13], and it was realized that a solution was necessary for the field to advance. This is also a challenge in the area of bioabsorbable orthopedics, where standardized *in vitro* corrosion methods (ASTM-D1141-98 for

immersion and DIN50918 for polarization) were used in comparison to micro-computed tomography measurements of explants, but no correlation between the sets of corrosion measurements was identified [14]. Kirkland *et al.* [15] concluded after a thorough review of bioabsorbable metallic implant literature that "at present, a strong correlation between *in vitro* and *in vivo* corrosion results has yet to be established in any reported work." This subject was also recently addressed by a workshop among experts organized jointly by the American Society for the Testing of Materials (ASTM) and the United States Food and Drug Administration (FDA). The ASTM-FDA workshop [16] reinforced the view that little is known about the predictive powers of *in vitro* corrosion testing with respect to *in vivo* biocorrosion of absorbable metallic implants.

Development of an appropriate *in vitro* protocol to simulate arterial degradation of magnesium has been widely investigated and debated. For example, Lévesque and coworkers [17] developed a sophisticated test bench in which samples were subjected to corrosion under pseudophysiological flow conditions. Other researchers have gone as far as to use human whole blood in a Chandler-loop configuration to construct a relevant *in vitro* test [18, 19]. Such efforts are characteristic of one current testing paradigm, which states that every effort should be made to replicate *in vivo* conditions in order to shift the rate and character of corrosion as close as is practical to that found in the human body. Relevant conditions may include pH, regulated by buffering or reagent administration; test solution-to-surface area ratio; the composition of the test solution; and the presence of proteins, among others [15, 20]. However, simple immersion testing in a suitable medium, such as Dulbecco's Modified Eagle Medium (DMEM), also produces an

appropriate corrosion response in magnesium [20, 21]. Increasingly complicated methods appeared to modulate the rate of corrosion, but did not change the character of the surface layer on commercially pure magnesium wires. For example, wires were immersed in DMEM after being encapsulated by an extracellular matrix, namely fibrin, [22], and a laminar flow cell was constructed and used to expose materials to flowing media [21]. Neither treatment resulted in grossly different corrosion products or morphologies thereof.

Several key aspects of testing dictate whether an *in vivo-in vitro* correlation may be established. These factors include:

1. a uniform sample geometry used both *in vivo* and *in vitro*;
2. an appropriate method of quantification that produces comparable data;
3. a reliable *in vivo* model that mimics human vasculature; and
4. a repeatable *in vitro* corrosion protocol that replicates the *in vivo* degradation mechanism.

The first barrier may be overcome by using uniform samples in all modes of analysis; the preferred geometry is that of a wire or small strip as previously discussed [22]. The second challenge may be met by one of an array of applicable analytical methods, including mass loss measurements, computed tomography, or other *ex post* modes of analysis. A method of mechanical evaluation in which corroded samples were subjected to tensile loading was previously developed [22], and it was shown to be capable of

resolving both material and environmental differences. To address the third point, an *in vivo* model was developed in which wires were implanted within the murine arterial lumen and wall to simulate pre- and post-encapsulation corrosion behavior, respectively [23]. Complementary methods may include sample implantation into a mini-swine or use of an alternative murine model [24]. To satisfy the fourth and final point, a simple DMEM immersion protocol was used. Culture media, such as DMEM, has an ionic profile like that of blood serum, which is crucial to replicating physiological corrosion [25]. However, simple immersion does not replicate the mass transport-restricting properties of the tissue, nor is it chemically identical to the arterial tissue. It lacks proteins and many organic molecules that may have an effect on corrosion. The lack of secondary constituents and modified mass transport *in vitro* can be accounted for in an appropriate multiplier. In future instances, other, more nuanced protocols may be substituted, which could control some of these important factors.

In the present work, the murine arterial implantation method, static submersion protocol, and tensile testing are coupled to construct a new mechanical *in vitro-in vivo* correlation for bioabsorbable magnesium in the arterial environment. Various mechanical metrics are utilized in this analysis, and the advantages and disadvantages of each are discussed. The resultant multipliers may be considered valid for correlating degradation of pure magnesium in the murine artery to physiological corrosion induced by immersion in a static DMEM solution. Such an approach satisfies the general criteria for establishing an *in vitro-in vivo* relationship, and constitutes a widely practicable way to correlate *in vitro* with *in vivo* behavior.

2.1.3 Methods and Materials

2.1.3.1 Material selection

For all experiments, a 250 ± 25 μm diameter magnesium (Mg) wire of 99.9%+ (commercial) purity was obtained from Goodfellow USA (Coraopolis, PA). 20 mm lengths (±1 mm) were cut from the coil and straightened by hand; this sample length afforded 5 mm on each side to serve as a grip section in post-corrosion tensile testing without compromising their ability to be implanted.

2.1.3.2 Implantation for *in vivo* corrosion

Prior to implantation, the Mg wires were briefly sanitized in 70% ethyl alcohol and irradiated with ultraviolet light. A surgical protocol previously used to implant samples in the arterial wall was utilized [23]. A single 20 mm wire segment for tensile testing and a single 10 mm segment for characterization (not included in this contribution) were implanted in serial segments of the abdominal aorta of each of ten adult Sprague-Dawley rats. During surgery, the magnesium wires were used to puncture the adventitial layer, and were then led into or near the medial layer without damaging the endothelium. At the end of 5–32 days a single rat was euthanized and the 10 and 20 mm Mg wires retrieved from the artery. If the wires were found in the artery already fragmented, they were designated "functionally degraded" and assigned a tensile strength and elongation of zero. After retrieval, the wires were stored in the low humidity environment of a desiccator. Animal study was approved by the Michigan Technological University

Institutional Animal Care and Use Committee and was conducted in accordance with the Panel on Euthanasia of the American Veterinary Medical Association.

2.1.3.3 Immersion and incubation for *in vitro* corrosion

In vitro corrosion was conducted using simple immersion in Dulbecco's Modified Eagle Medium. The DMEM variant used here was manufactured by Gibco® (Grand Island, NY), and was a high-glucose variety that contains both phenol red indicator and sodium pyruvate; it did not contain L-glutamine or HEPES buffer. A solution of 10,000 units/mL penicillin and 10 mg/mL streptomycin (Sigma Aldrich; St. Louis, MO) was added to the DMEM at a level of 1 vol.% to retard bacterial and fungal growth. 20 mm long Mg wire segments were ultrasonically cleaned in isopropyl alcohol (99%+) for two minutes and subjected to ultraviolet radiation. The Mg wires were placed at the bottom of untreated, polycarbonate eight-well plates, and 5 mL of DMEM solution was pipetted in each well. The trays were placed in a cell culture incubator maintained at 37°C and 5% CO_2 for a time varying from 1 to 16 days with three replicates per time point.

After the specified period, the DMEM solution from the compartments containing 20 mm wires was collected for pH measurement. The pH of the DMEM was observed to increase in the first two days to a value of approximately 8.2–8.3 and stabilized thereafter (data not shown). The increase is expected from physiologically corroding magnesium, and originates from the consumption of acidic ions in the hydrogen reduction reaction [26]. The wires were removed and stored in a desiccated environment. If the samples fragmented in the solution during removal through no human error they were designated

"functionally degraded" and, again, assigned an effective tensile strength and elongation of zero.

2.1.3.4 Quantification using tensile testing and analysis

Tensile testing was carried out according to the previously reported protocol [22] briefly summarized here. Two polycarbonate substrates (approximately 30 mm wide × 40 mm long) were separated by a distance of 10 mm while wooden supports were fixed to the reverse side by adhesive tape. The corroded and control wires (20 mm nominal length) were mounted such that 5 mm on each end was fixed to one of the substrates with Loctite "General Purpose" two-part epoxy (Henkel Corporation; Westlake, OH). After allowing the epoxy to cure, the mounts were loaded in tension after disrupting the wooden supports using a Test Resources (Shakopee, MN) 100-series modular test system with a 250 lb_f (~1.1 kN) load cell. The crosshead speed of 0.2 mm/min corresponded to a strain rate of 3.3×10^{-4} per second. Load data was logged at a rate of 16 Hz.

Because a conventional extensometer could not be clipped to the gauge section of this sample, compliance of the load frame was removed by use of a post-processing MATLAB script based on user selection of the linear elastic portion of the load-elongation curve. Conversion of load and elongation to stress and strain, respectively, was based on a 10 mm gauge section and a fixed gauge diameter of 250 μm. The latter assumption resulted in values of "effective stress" that has merits discussed at length in a

previous report [22]. Smoothing of tensile data for presenting the curves was performed by a custom MATLAB boxcar-like algorithm with Gaussian central-point weighting.

2.1.3.5 Statistical methods

Statistical analyses in this report were conducted using the MATLAB Statistics Toolbox. Point-to-point integration was conducted using the trapezoidal method. All error values and error bars in this contribution are reported as standard error. Linear regression, when necessary, was carried out using the *regstats* function. The standard error associated with the *in vivo*-*in vitro* multiplier was computed using an error propagation approach [27] under the assumption that errors were random in nature. Any tests for significance were conducted using a one-tailed *t*-test, wherein the confidence level necessary to claim significance was 95%.

2.1.4 Results

2.1.4.1 Observations from *in vivo* specimens

In this experiment, all magnesium wires were easily extricated from the arterial wall. At present, it is thought that a degradation time of one month does not provide enough time for tissue to adhere firmly to the implant, and hydrogen evolution may have also adversely affected tissue adhesion [26]. The explants were found to be intact with good mechanical integrity through 29 days. At 32 days, however, the 20 mm wire was found fractured *in situ*, presumably due to uniform and semi-localized corrosion in combination with typical stresses imposed on the implant by the arterial matrix. In mechanical terms,

the 32-day explant was considered to be “functionally degraded,” and effective tensile strengths and elongations to failure of zero were assigned to this sample. The surface character and bulk composition of the magnesium corrosion products are not addressed here; these analyses will be included in a future report. Furthermore, the fracture surfaces and characteristics thereof were presented in a previous contribution [22].

Much can be learned by examining the effective stress versus strain plots obtained during tensile testing, presented in Figure 2.1. As samples became increasingly degraded, the tensile profile of the as-received wire was scaled both vertically, corresponding to a decrease in the maximum effective stress, and horizontally, indicating a lower strain to failure. Some factors, including the strain necessary to initiate yielding and the sample flow stress, decreased in relatively small increments. Variability was observed in the measured slope of the linear-elastic region. Such deviations are to be expected when using this tensile testing method. The most pronounced change from time point-to-time point is the severe decrease in uniform plastic deformation that occurs between each time point, which has implications regarding the total work necessary to fracture the specimens.

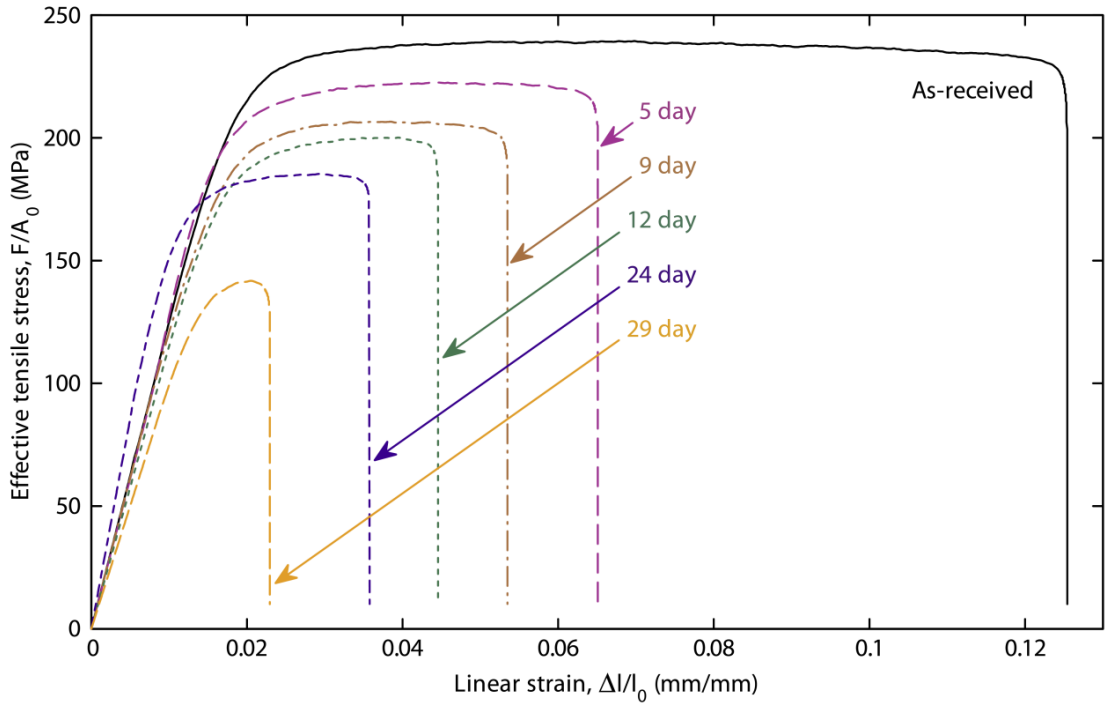

Figure 2.1 – Effective stress ($\sigma_{eff} = F/A_0$) plotted as a function of linear strain (l_0 = 10 mm) for representative tests of magnesium explants. A trend of decreasing elongation to failure and decreasing effective tensile strength results in scaling of the curves towards the origin.

Calculation of the area beneath the tensile curve yields information about the work of fracture [28], which is, in practical terms, the mechanical work required to deform the magnesium wires sufficiently to cause fracture. The volume-normalized nominal work of fracture of Mg in wire form was 28.4 ± 0.8 MN·m/m^3. A sudden decrease in the work of fracture was evident (Figure 2.2). By five days' residence it was reduced to approximately 12.3 MN·m/m^3, or about 43% of the as-received value. After a rapid initial decrease, the loss in work of fracture appeared linear (R^2 = 0.82, p-value = 5×10^{-3}) at a rate of 0.38 ± 0.08 MN·m/m^3 per day. After 29 days in the arterial wall, the measured work of fracture was 2.2 MN·m/m^3—a paltry 8% of the nominal value. The

inability of the severely degraded wires to accommodate even small amounts of mechanical work may help explain why fracture is observed after a 32 day *in vivo* residence, when linear extrapolation predicts a work of fracture less than 1 MN·m/m^3.

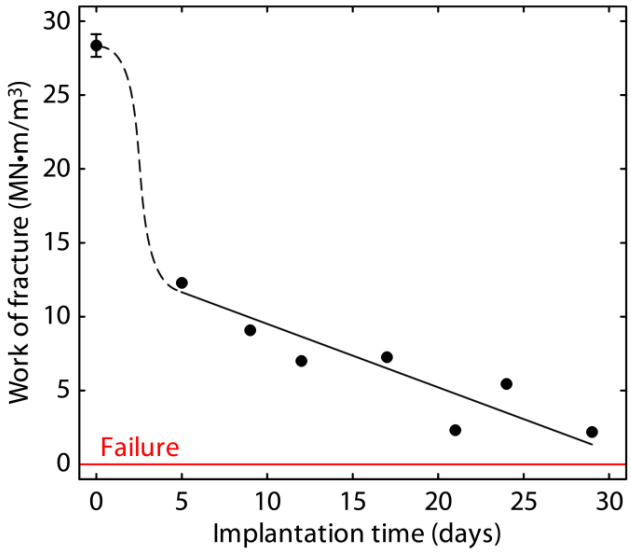

Figure 2.2 – Nominal volume-normalized work of fracture observed in explanted magnesium wires. The nominal value is assigned a standard error.

2.1.4.2 Development of *in vitro-in vivo* multipliers

2.1.4.2.1 Use of conventional metrics

The tensile behavior of samples corroded *in vitro* is modified by the presence of an intact corrosion overlayer; a comparable formation present *in vivo* seems to be sufficiently damaged to prevent its participation in the tensile test. As discussed previously [22], the typical *in vitro* tensile profile is evocative of brittle-matrix composite deformation. For this reason, analysis of work of fracture like that considered for *in vivo* samples in the previous section is not extensible to *in vitro* tensile data. Fortunately, other mechanical

metrics unobfuscated by the participation of corrosion products—effective tensile strength ($\sigma_{\mathrm{eff}}^{\mathrm{TS}} = \mathrm{F}/\mathrm{A}_0$), the functional life of the implant, and the strain to failure (ϵ_{f})—were available for assessment. These are critical parameters in long-term stent performance, and could potentially be extended to predict properties and eventual fragmentation *in vivo*.

The effective tensile strength and strain to failure values are shown in Figure 2.3 for both *in vivo* (panels A and B) and *in vitro* samples (panels C and D). The decrease in strength follows a linear downward trend in both environments for the bulk of the sample lifetime. However, the effective tensile strength decreases abruptly when functional degradation occurs. Interpretation of the strain to failure trend is somewhat more subjective; it seems from the early-stage *in vitro* behavior that the initial decrease is slow, followed by a rapid decrease and subsequent downward linear trend. The qualitative similarity of elongation to failure trends [Figure 2.3(B) and (D)] to the work of fracture behavior [Figure 2.2] is strong. From this, it is inferred that functional degradation is closely tied to strain to failure, though it does not appear to be a perfect predictor at times close to the endpoint.

These rates—$\sigma_{\mathrm{eff}}^{\mathrm{TS}}$ decrease, ϵ_{f} decline, and inverse functional degradation times—were transformed into a set of values comprising an *in vitro-in vivo* correlation through trend and error propagation analyses. The linear regions designated for analysis varied between metrics. For the effective tensile strength, all data excluding the functionally degraded point were considered. Strain to failure data were limited to those *after* the

initial, sharp decrease but *before* functional degradation, and are labeled in Figure 2.3(B) and (D).

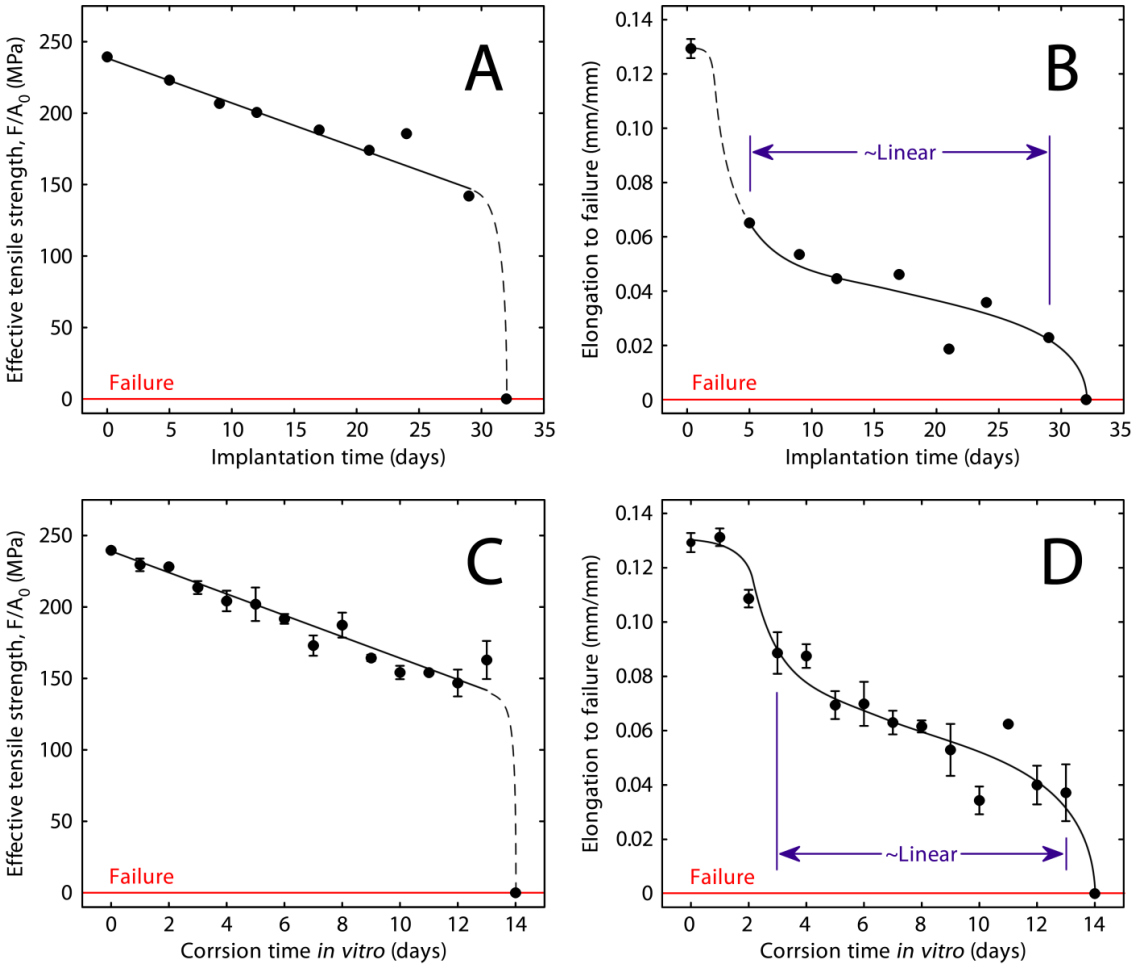

Figure 2.3 – Trends in mechanical behavior observed *in vivo* for effective tensile strength (A) and elongation to failure (B) as well as mechanical degradation observed *in vitro* in strength (C) and elongation (D). Note the difference in time scales. The as-received and *in vitro* data (C and D) are assigned standard errors.

The values of these metrics are presented in Table 2.1 in addition to goodness-of-fit indicators. Slightly different multipliers were found in each case:

i. the strength trend indicated that *in vitro* degradation was 2.2 ± 0.5 times faster than that *in vivo*;

ii. strain to failure led to the conclusion that *in vitro* corrosion progressed 3.1 ± 0.8 times faster; and

iii. the degradation as evidenced by the inverse degradation time was 2.3 ± 0.3 times faster *in vitro* than *in vivo*.

Table 2.1 – *In vitro* and *in vivo* trends/values and their associated errors that enabled calculation of an *in vitro-in vivo* multiplier.

Metric	**Environment**	**Trend/Metric Value**	**R^2**	***p*-value**	***In vitro-In vivo* Multiplier**
Effective strength, σ_{eff}^{TS} (MPa/day)	*In vivo*	-2.8 ± 0.5	0.88	2×10^{-3}	2.2 ± 0.5
	In vitro	-6.4 ± 0.8	0.67	2×10^{-8}	
Strain to failure, ϵ_f (10^3/day)	*In vivo*	-1.7 ± 0.4	0.78	8×10^{-3}	3.1 ± 0.8
	In vitro	-5.3 ± 0.7	0.68	1×10^{-8}	
Functional degradation time (days)	*In vivo*	32 ± 3*	-	-	2.3 ± 0.3
	In vitro	14 ± 1*	-	-	
Combined, $\sigma_{eff}^{TS} \times \epsilon_f$ ((MN·m/m^3)/day)	*In vivo*	-0.44 ± 0.08	0.84	3×10^{-3}	3.1 ± 0.7
	In vitro	-1.4 ± 0.2	0.74	7×10^{-10}	

* Estimated error based on temporal resolution of mechanical data

2.1.4.2.2 Use of a combined metric

The authors contend that the work of fracture (Figure 2.2) is the single best predictor of *in situ* implant fragmentation. A similar metric that is not subjected to brittle matrix-induced error, but is comparable *in vitro* and *in vivo*, is desired. A possible value that could stand in for the work of fracture is the product of the effective tensile strength and strain to failure ($\sigma_{eff}^{TS} \times \epsilon_f$), herein referred to as the "combined metric." Multiplication of the individual factors captures the primary modulation of work of fracture by reduction of

ϵ_f, while at the same time reflecting the comparatively minor effect of tensile strength reduction. The resulting combined metric has the same units as the nominal volume-normalized work of fracture previously discussed (MN·m/m^3), and thus should approach zero as the implant becomes increasingly prone to fracture. Calculations on the same *in vitro* and *in vivo* mechanical data discussed in the previous section were carried out, and are presented in Figure 2.4.

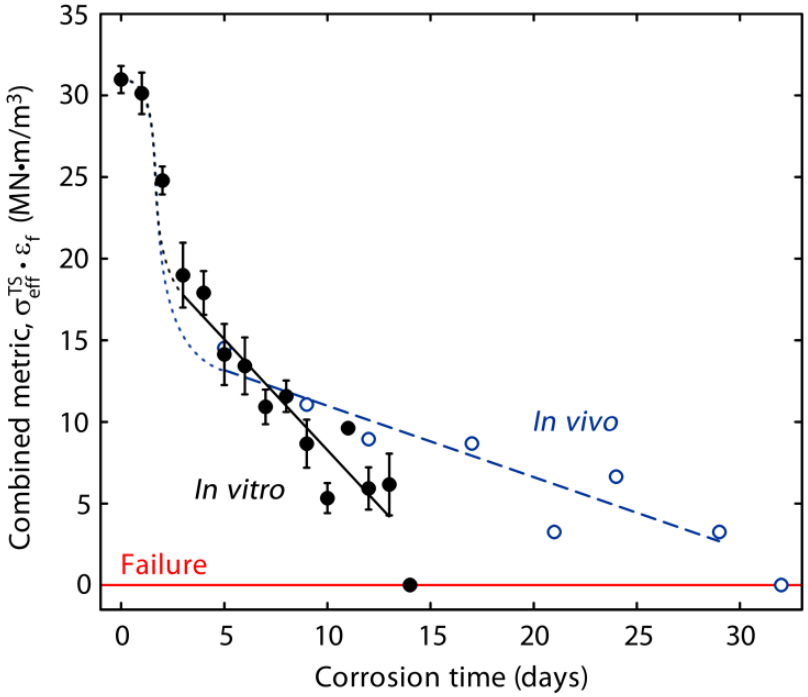

Figure 2.4 – Trend observed for the combined mechanical metric ($\sigma_{eff}^{TS} \times \epsilon_f$) for *in vivo* (○) and *in vitro* (●) samples, with the two relevant linear trends (*in vivo* and *in vitro* dotted and solid, respectively).

A regression analysis was performed in a manner identical to the strain to failure analysis previously discussed. The same point selection criteria were used, and the selected points form the linear trend lines presented in Figure 2.4. The regression and goodness-of-fit

results are presented in the last row of Table 2.1. Trend analysis indicated that the rate of decrease in the combined metric (0.44 ± 0.08 MN·m/m^3 per day) was comparable to the work of failure value previously discussed (0.38 ± 0.08 MN·m/m^3 per day). The *in vitro* rate of decrease in the combined metric was calculated to be 3.1 ± 0.7 times faster than the corresponding *in vivo* reduction. Incidentally, this is partway between the strain to failure and the effective tensile strength multipliers (Table 2.1).

2.1.5 Discussion

Comparing the various metrics and their associated errors using a one-tailed *t*-test indicated that there were no significant differences between metrics (Table 2.2). A visual comparison of multiplier values, presented in Figure 2.5, reveals that the values are close in magnitude, and their errors are large in comparison to inter-metric differences.

Table 2.2 – Matrix of p-values found by comparing the individual multipliers (row versus column) in a one-tailed t-test. A p-value < 0.05 was required to claim significance.

	***p*-values**		
Parameters	*Strain to Failure (ϵ_f)*	*Degradation Time*	*Combined Metric ($\sigma_{eff}^{TS} \times \epsilon_f$)*
Strength (σ_{eff}^{TS})	0.17	0.46	0.15
Strain (ϵ_f)		0.17	0.49
Degradation Time			0.14

While statistical significance cannot be claimed, it is evident from both Table 2.2 and Figure 2.5 that effective tensile strength and time to degradation are similar in magnitude, as are strain to failure and the combined metric ($\sigma_{eff}^{TS} \times \epsilon_f$). The origins of this difference

seem to lie in the nature of the trend calculation; both strength- and time-based multipliers take advantage of strict linearity—real and assumed, respectively—while strain-based and combined metrics are calculated only for a linear portion of their respective nonlinear data sets.

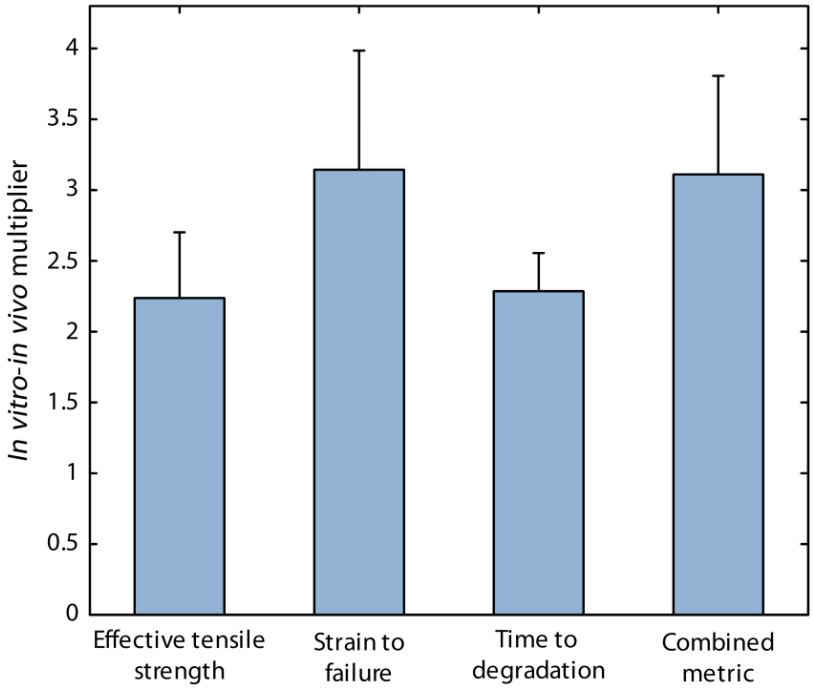

Figure 2.5 – Visual presentation of the various mechanical *in vivo-in vitro* multipliers. Error bars are indicative of standard error.

Various methods of calculation lead to differential utility of the aforementioned multipliers (Table 2.3). It seems that the time to functional degradation (multiplier of 2.3 ± 0.3) is appropriate for most *in vitro* testing employed in screening experiments. A 1-to-2.3 (*in vitro*-to-*in vivo*) timescale is simple to employ in testing, and can at least provide a first-approximation implant lifetime. Some intricacies of the degradation process are not accessible to this metric. It does not embody, for example, the transient embrittlement of

a given material. In addition, changes in the *in vitro* methodology or active corrosion mechanisms necessitate new *in vitro* experiments in order to recalculate the multiplier. This metric also utilizes only a single value as opposed to a trend, and thus possesses reduced robustness. However, it has the unique advantage of being valid over the entire implant lifetime, fundamentally because it *is* the implant lifetime, and is therefore the most viable in application to pure magnesium under the conditions reported.

Table 2.3 – Utility and drawbacks of the various mechanical multipliers.

Multiplier Basis	**Utility**	**Drawbacks**
Effective strength, σ_{eff}^{TS}	− Linear throughout the degradation process − Indicates maximum load borne by corroded specimens	− Requires assumed minimum value to predict functional degradation
Strain to failure, ϵ_f	− Closely related to sample embrittlement	− Only linear for part of the degradation process − May not approach zero at time of failure
Functional degradation time	− Is, by definition, equivalent to the implant lifetime − Simple application in material screening	− Lack of statistical robustness
Combined metric, $\sigma_{eff}^{TS} \times \epsilon_f$	− Approximates work of failure − Most predictive of sample failure (approaches zero)	− Only linear for the latter portion of the degradation process

The remaining three metrics present a conundrum: no single correlation seems to be useful over the entire implant life cycle without the application of restrictive assumptions. The effective strength multiplier, for instance, requires knowledge of the minimum viable tensile strength, or the value at which functional degradation is observed. The problem with formulating this boundary condition lies in the apparent independence of functional

degradation from the effective tensile strength; the dominant linear trend does not approach zero at the time of failure [Figure 2.3(A) and (C)]. A consistent minimum value of ~60% of the nominal strength seems to apply to the *in vitro* and *in vivo* data in this report, but the wider applicability of this value as a limiting criterion is not evident. Similar to the effective strength criterion, the strain to failure and combined criteria are not valid over the entire sample lifetime. They seem to pose a problem opposite to the previous, however, in that they require a limiting *maximum* value at which the initial, rapid decline ceases and linearity begins. The combined metric, in particular, seems to approach zero at the observed time of failure, but the value at which linearity begins is inconsistent. The confluence of restricting factors limits this metric's utility in extrapolating from *in vitro* data, though it does potentially enable the calculation of mechanical properties in the course of *in vivo* degradation.

This report presents a method of determining a numerical value for *in vivo-in vitro* correlation, but the utility of the numerical value is inherently limited to pure magnesium material in the murine artery. As mentioned previously, significant changes to the corrosion environment or active mechanism might shift the numerical value of this correlation. Generally speaking, the chemistry of the *in vivo* and *in vitro* corrosion environments are relatively constant if good practice (i.e. media volume-to-surface area ratio) is followed [15]. Modification of the corrosion mechanism, on the other hand, can easily originate from a change in the material composition [29] or an improperly selected corrosion medium [19]. Material factors (i.e. alloying , surface preparation, etc.) can

activate local or microgalvanic corrosion mechanisms [30] that would require re-working of the multiplier. Likewise, extension of this multiplier to other base materials would require repeating the analysis presented here to determine a material-specific *in vivo-in vitro* correlation.

2.1.6 Conclusions

A new *in vitro-in vivo* correlation is proposed here for the physiological corrosion of magnesium in the arterial environment that relies on a direct comparison of the mechanical behavior of uniform, progressively degraded samples. *In vivo* corrosion of magnesium wires was carried out in the arterial walls of rats, and *in vitro* corrosion experiments were conducted by immersing identical samples in static culture media (DMEM). Tensile profiles and the work of fracture of explanted magnesium samples were discussed. Four metrics were utilized to formulate *in vitro-in vivo* correlation: the effective tensile strength (with a multiplier of 2.2 ± 0.5); strain to failure (3.1 ± 0.8); the time to functional degradation (2.3 ± 0.3); and a combined metric, $\sigma_{\mathrm{eff}}^{\mathrm{TS}} \times \epsilon_{\mathrm{f}}$ (3.1 ± 0.7). All metrics indicated that *in vitro* corrosion in static media was more rapid than *in vivo* corrosion in the murine arterial wall. None of the individual multipliers showed statistically significant differences, but each one was observed to have both specific utility and restrictions in application. It is suggested that a multiplier based on the time to functional degradation is generally appropriate for an estimate of implant lifetime *in vivo*, while the others may be used to infer implant properties in service.

2.1.7 Acknowledgements

The DeVlieg Foundation and the American Heart Association are acknowledged for supporting P. K. B. during the time this work was conducted. The authors thank Adam Drelich for his assistance in performing the tensile testing. Emily Shearier is acknowledged for her assistance editing and proofreading.

2.1.8 References

[1] G. Mani, M.D. Feldman, D. Patel, C.M. Agrawal, Biomaterials 28 (2007) 1689-1710.

[2] R. Waksman, R. Pakala, Curr. Pharm. Design 16 (2010) 4041-4051.

[3] Y. Onuma, J. Ormiston, P.W. Serruys, Circ. J. 75 (2011) 509-520.

[4] M. Haude, R. Erbel, P. Erne, S. Verheye, H. Degen, D. Bose, P. Vermeersch, I. Wijnbergen, N. Weissman, F. Prati, R. Waksman, J. Koolen, Lancet 381 (2013) 836-844.

[5] P.K. Bowen, J. Drelich, J. Goldman, Adv. Mater. 25 (2013) 2577-2582.

[6] P.J. Prendergast, S.A. Maher, J. Mater. Process Tech. 118 (2001) 337-342.

[7] W.M.S. Russell, R.L. Burch, C.W. Hume, The principles of humane experimental technique, Universities Federation for Animal Welfare, Wheathampstead, England, 1992.

[8] D. Martin, F.J. Boyle, Comput. Methods Biomec. 14 (2011) 331-348.

[9] D. Gastaldi, V. Sassi, L. Petrini, M. Vedani, S. Trasatti, F. Migliavacca, J. Mech. Behav. Biomed. Mater. 4 (2011) 352-365.

[10] J.A. Grogan, B.J. O'Brien, S.B. Leen, P.E. McHugh, Acta Biomater. 7 (2011) 3523-3533.

[11] W. Wu, S. Chen, D. Gastaldi, L. Petrini, D. Mantovani, K. Yang, L. Tan, F. Migliavacca, Acta Biomater. 9 (2013) 8730-8739.

[12] R. Willumeit, F. Feyerabend, N. Huber, Acta Biomater. 9 (2013) 8722-8729.

[13] B. Heublein, R. Rohde, V. Kaese, M. Niemeyer, W. Hartung, A. Haverich, Heart 89 (2003) 651-656.

[14] F. Witte, J. Fischer, J. Nellesen, H.-A. Crostack, V. Kaese, A. Pisch, F. Beckmann, H. Windhagen, Biomaterials 27 (2006) 1013-1018.

[15] N.T. Kirkland, N. Birbilis, M.P. Staiger, Acta Biomater. 8 (2012) 925-936.

[16] M. Dreher, S. Anderson, ASTM-FDA workshop on absorbable medical devices: Lessons learned from correlations of bench testing and clinical performance, Department of Health and Human Services, Food and Drug Administration, Silver Spring, MD, 2012.

[17] J. Levesque, H. Hermawan, D. Dube, D. Mantovani, Acta Biomater. 4 (2008) 284-295.

[18] J. Geis-Gerstorfer, C. Schille, E. Schweizer, F. Rupp, L. Scheideler, H.P. Reichel, N. Hort, A. Nolte, H.P. Wendel, Mater. Sci. Eng. B 176 (2011) 1761-1766.

[19] C. Schille, M. Braun, H.P. Wendel, L. Scheideler, N. Hort, H.-P. Reichel, E. Schweizer, J. Geis-Gerstorfer, Mater. Sci. Eng. B 176 (2011) 1797-1801.

[20] R. Willumeit, J. Fischer, F. Feyerabend, N. Hort, U. Bismayer, S. Heidrich, B. Mihailova, Acta Biomater. 7 (2011) 2704-2715.

[21] P.K. Bowen, J. Drelich, R.E. Buxbaum, R.M. Rajachar, J. Goldman, Emer. Mater. Res. 1 (2012) 237-255.

[22] P.K. Bowen, J.A. Gelbaugh, P.J. Mercier, J. Goldman, J. Drelich, J. Biomed. Mater. Res. B 100B (2012) 2101-2113.

[23] D. Pierson, J. Edick, A. Tauscher, E. Pokorney, P.K. Bowen, J. Gelbaugh, J. Stinson, H. Getty, C.H. Lee, J. Drelich, J. Goldman, J. Biomed. Mater. Res. B 100B (2012) 58-67.

[24] P.P. Mueller, S. Arnold, M. Badar, D. Bormann, F.W. Bach, A. Drynda, A. Meyer-Lindenberg, H. Hauser, M. Peuster, J. Biomed. Mater. Res. A 100 (2012) 2881-2889.

[25] Y. Xin, K. Huo, H. Tao, G. Tang, P.K. Chu, Acta Biomater. 4 (2008) 2008-2015.

[26] G. Song, Corros. Sci. 49 (2007) 1696-1701.

[27] Y. Beers, Introduction to the Theory of Error, 2nd ed. Addison-Wesley, Reading, MA, 1957.

[28] M.A. Meyers, K.K. Chawla, Mechanical Behavior of Materials, Cambridge University Press, Cambridge, 2009.

[29] G. Song, A. Atrens, Adv. Eng. Mater. 1 (1999) 11-33.

[30] A. Atrens, M. Liu, N.I. Zainal Abidin, Mater. Sci. Eng. B 176 (2011) 1609-1636.

2.2 Rates of *in vivo* (arterial) and *in vitro* biocorrosion for pure magnesium[4]

2.2.1 Abstract

The development of magnesium-based materials for bioabsorbable stents relies heavily on corrosion testing by immersion in pseudophysiological solutions, where magnesium degrades faster than it does *in vivo*. The quantitative difference in corrosion kinetics *in vitro* and *in vivo* is largely unknown, but, if determined, would help reduce dependence on animal models. In order to create a quantitative *in vitro*-*in vivo* correlation based on an accepted measure of corrosion (penetration rate), commercially pure magnesium wires were corroded *in vivo* in the abdominal aortas of rats for 5–32 days, and *in vitro* for up to

[4] The material in Section 2.2 was previously published in the *Journal of Biomedical Materials Research Part A* and is reproduced here with permission.

P. K. Bowen, A. Drelich, J. Drelich, and J. Goldman. "Rates of *in vivo* (arterial) and *in vitro* biocorrosion for pure magnesium." *J. Biomed. Mater. Res. A* 103(1) 341-349 (2015), doi: 10.1002/jbm.a.35179.

References in Section 2.2 follow the *Journal of Biomedical Materials Research Part A* author guidelines.

14 days using Dulbecco's modified eagle medium (DMEM). Cross-sectioning, scanning electron microscopy, image analysis, a modified penetration rate tailored to degraded wires, and empirical modeling were employed to analyze the corroded specimens. *In vitro* penetration rates were consistently higher than comparable *in vivo* rates by a factor of 1.2–1.9× (± 0.2×). For a sample < 20% corroded, an approximate *in vitro-in vivo* multiplier of 1.3 ± 0.2× applied, while a multiplier of 1.8 ± 0.2× became appropriate when the magnesium specimen was 25–35% degraded.

2.2.2 Introduction

The physiological corrosion of magnesium and its alloys has been a key area of study in biomedical materials engineering in the last decade, with one long-term objective being widespread use of bioabsorbable endovascular (i.e. coronary) stents [1-4]. Investigative methods for the corrosion of bioabsorbable metallic devices are wide-ranging, employing environments ranging from pseudo-physiological salt solutions [5, 6], to simulated body fluids [7, 8] or cell culture media [9, 10], to murine [11-13] and porcine [14-18] animal models. The wide array of corrosion environments and techniques employed have resulted in variability in corrosion rates and mechanisms [19]. It has been shown, however, that valid alloy-to-alloy comparisons are possible with conscientious selection of environment and methods of analysis [20, 21]. At present, it is necessary to establish a relationship between corrosion conducted *in vitro* using physiologically relevant solutions and degradation that occurs *in vivo*. Such a correlation would improve the predictive power of *in vitro* immersion tests, thereby reducing the need for *in vivo* tests.

This was a conclusion of the recent review by Kirkland *et al.* [22] and the topic of a workshop co-hosted by ASTM International and the United States Food and Drug Administration [23].

Reported attempts at comparative corrosion measurements have been relatively limited. The first focused attempt appears to have been conducted by Witte and coworkers [24], who evaluated orthopedic biomaterials both *in vivo* using guinea pigs and *in vitro*. Quantitative comparisons were made by comparing microscale X-ray computed tomography (μCT) of the explanted materials to *in vitro* weight change and Tafel extrapolation (electrochemical) values using a standard chloride-sulfate salt solution. No reproducible correlation was identified. Deng *et al.* [25] discussed a prospective *in vitro-in vivo* correlation using full-stent weight loss measurements acquired from μCT. It was recognized that *in vitro* and *in vivo* degradation occurred on independent timescales, thus complicating the development of a correlation. The issue was resolved by relating the two corrosion systems on a scale of increasing corrosion severity. However, no quantitative results were presented in this work to validate the approach. A lack of progress in producing and comparing *in vivo* and *in vitro* measurements likely involves the relative difficulty of animal compared to benchtop studies in addition to the lack of a reliable model system for stent degradation.

A metallic specimen with wire geometry has been used in previous work to mimic a single stent strut. Figure 2.6 demonstrates that a 0.25 mm diameter wire is comparable in scale and geometry to the struts of a commercial Boston Scientific Express2™ stent. The

small size of the model geometry allows for *in vivo* corrosion testing in a small animal, such as within the abdominal aorta of a rat [11].

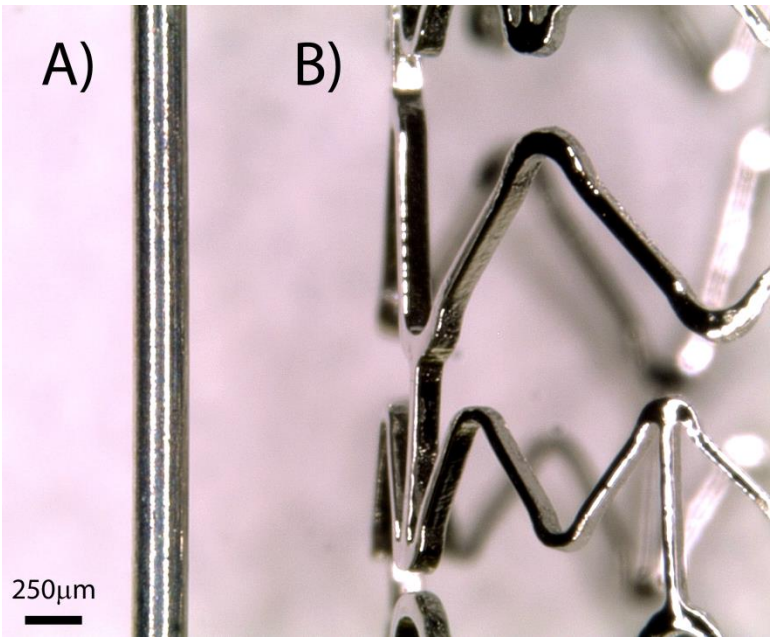

Figure 2.6 – An as-received 0.25 mm diameter wire (A) next to an expanded Boston Scientific Express2™ stent (B).

In vivo experience with this model has shown that magnesium undergoes bioabsorption in three stages: (I) the intact implant undergoes corrosion governed by rapid dissolution [26-28] later limited by self-protective behavior [29, 30]; (II) local, rapid, so-called "terminal" dissolution and fragmentation of the implant [31]; and (III) long-term absorption of fragmented/granular products of biocorrosion [32]. An *in vivo-in vitro* correlation is of immediate interest for stages in which magnesium acts as a structural implant material, namely stages I and II. It is anticipated that such a correlation may provide novel insight into *in vitro* versus *in vivo* magnesium corrosion as well as identify

potential avenues for modifying the *in vitro* immersion fluid to more closely match the corrosion behavior seen for magnesium *in vivo*.

To this end, Bowen *et al.* [33] compared the mechanical behavior of two sets of commercially pure magnesium wires in tension, previously shown to be a good, albeit unconventional, corrosion metric [34]. One set of wires was corroded *in vivo* in the abdominal aorta of rats, while the other was corroded *in vitro* using immersion in Dulbecco's modified eagle medium (DMEM). This approach satisfied a set of criteria considered necessary for *in vivo-in vitro* correlation development: uniform sample geometry; a suitable method of quantification; a relevant *in vivo* model; and a repeatable *in vitro* corrosion protocol with a corrosion mechanism similar to that acting *in vivo*. In general, modeling relied on fitting quasi-linear portions of the data set, and resulted in four separate multipliers, each corresponding to a different mechanical metric. The preferred correlation was based on the time to failure, or "functional degradation," which indicated corrosion *in vivo* took approximately 2.3 times longer than comparable degradation *in vitro*.

Leading up to this work, no correlation has been developed to relate *in vitro* corrosion to that expected *in vivo* based on a conventional corrosion metric. An *in vivo-in vitro* relationship that may be applied to such values as mass loss, μCT volume loss, hydrogen evolution, and Tafel extrapolation from potentiodynamic polarization [22] is required to satisfactorily address the fundamental research question: "how do the corrosion rates of magnesium alloys measured *in vitro* differ from those measured in an *in vivo* model?"

[24]. The goal of this study was, therefore, to create an *in vivo-in vitro* multiplier based on a conventional measure of corrosion, the penetration rate.

2.2.3 Materials and Methods

2.2.3.1 *In vivo* corrosion protocol

In vivo corrosion was conducted using a previously reported protocol [11]. Magnesium wire of 99.9% (commercial) purity and 250 ± 25 μm diameter from Goodfellow (Oakdale, PA) was divided into 10 mm segments and the ends smoothed with fine-grit sandpaper to remove any burrs. The wires were then cleaned with ethyl alcohol to remove dust or other loose contaminants and sterilize the surface. Adult male Sprague Dawley rats were anesthetized with isoflurane in oxygen. The 10 mm wire segments were used to puncture the outer adventitia of the abdominal aorta, and the wire was led in for the full length, firmly embedding it in the arterial media or inner adventitia. This procedure was reviewed and approved by Michigan Technological University's Internal Review Board. NIH guidelines for the care and use of laboratory animals were observed. This 10 mm segment was located proximal to a single 20 mm wire segment used in previous work for tensile testing [33].

Rats were housed until their euthanization and removal of the wires at ten time points ranging from 5 to 32 days. No post-implantation migration of the wires was observed after implantation in this study, as confirmed by visual inspection during extrication. The 32 day sample was observed to be fragmented *in situ*, constituting “functional

degradation" [33]. The explanted wires were stored in a desiccated environment prior to analysis.

2.2.3.2 *In vitro* corrosion protocol

In previous work by the authors, it was noted that a large volume of flowing media appeared to modify only the kinetics of degradation, while the degradation mechanism remained unaffected [9]. Similarly, inclusion of an extracellular coating (fibrin) modulated the degradation rate of magnesium, presumably by modulation of mass transport adjacent to the wire surface. However, the fibrin coating did not result in discernable differences in corrosion progression [34]. Based on these experiences, a simplified static immersion method was used to maximize repeatability.

The same lot of magnesium wire was divided into 10 mm segments, ultrasonically cleaned in isopropyl alcohol (99%+) for two minutes, and irradiated with ultraviolet light to clean and sterilize the surface. The wires were placed in eight-well plates and submerged in 5 mL of DMEM, a typical test solution for simulating magnesium biocorrosion [35, 36]. DMEM was purchased from Gibco® (Grand Island, NY) with phenol red indicator and sodium pyruvate; it did not contain HEPES buffer or L-glutamine. The DMEM was supplemented with 1 vol.% of a solution containing penicillin at 10,000 units mL^{-1} and streptomycin at 10 g L^{-1} (Sigma Aldrich; St. Louis, MO) to inhibit bacterial colonization. The media had a nominal pH of 7.51 ± 0.02. The plates with wires and media were incubated at 37°C and 5% CO_2 from 1 to 16 days

without replacement of the media. One 10 mm wire was removed each day, cleaned with ethyl alcohol to remove any residual media, and stored in a desiccator. Samples after 14 days were highly fragmented and could not be retrieved for further analysis. The pH of the media was measured after removal of the sample to be approximately 8.2–8.3 at each time point, consistent with previous observations [35].

2.2.3.3 Cross sectional analysis

Following the above analyses, the wires were placed in plastic sample clips and mounted in low viscosity two-part epoxy inside a silicone tube (~8 mm inner diameter). After curing, the mounted wires were removed from the silicone tubes. Cross sections were prepared by grinding the exposed wire in a metallographic fashion with 600- and 800-grit SiC paper and polishing with 1 μm Al_2O_3 slurry on a microfiber cloth. The polished end was then cut to create a section of 0.8–1 mm thickness. The newly exposed surface was ground, polished, and sectioned as before to produce 8–9 sections of explanted (*in vivo*) specimens and 5 sections of samples corroded *in vitro*. The embedded sections of wire were carbon-coated to improve conductivity and then imaged with a JEOL (Peabody, MA) JSM-6400 conventional SEM, using its backscattered electron detector to provide phase contrast. SEM imaging was conducted at 15 kV accelerating voltage and a reduced working distance of 12 mm. Images of each wire were acquired at 300× nominal magnification.

Cross sectional area (CSA) analysis was performed with the imageJ software package [37]. The process is illustrated in Figure 2.7. The visible area of the remaining

magnesium metal was selected by thresholding to select the brightest pixels ("A" in Figure 2.7) and the total area of the corresponding region—not just selected pixels—was measured ("B" in Figure 2.7). Previous characterization work demonstrated that the brightest central region was composed of metallic magnesium [31]. From the backscattered electron images, the nominal CSA of the wire section was estimated using an ellipse ("C" in Figure 2.7) and similarly measured. The change in cross sectional area was used to calculate a penetration rate for each section using an equation for the penetration of a small cylinder formulated in the next section. Regression analysis of the data and calculation of the correlation coefficient R^2 was done using the MATLAB software package. Error propagation calculations used the approach of Beers [38].

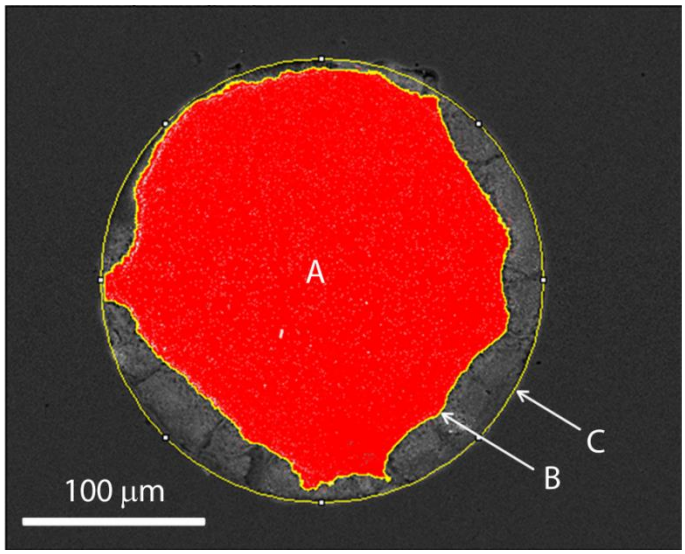

Figure 2.7 – Overlayed imageJ screenshots illustrating the process used to select regions for analysis. The area selected by thresholding (A) is selected as a continuous region, outlined in yellow (B), to represent remaining metallic magnesium. The original local cross sectional area is approximated by an ellipse (C).

2.2.3.4 Penetration rate for the wire geometry

A penetration rate was formulated for this sample geometry to reflect its expected physical meaning. The conventional penetration rate definition [39] is not well-suited to describing the corrosion of a small wire, as shown in the Appendix (Section 2.2.7). A modified penetration rate (*P'*) was defined for this purpose as the rate of change in radius at time *t*:

$$P' = -\frac{d(r(t))}{dt} \qquad \text{(Eq. 2.1)}$$

Integration and the application of the boundary condition $r(t = 0) = r_0$, where r_0 is the nominal sample radius, gave:

$$P' = \frac{r_0 - r(t)}{t} \qquad \text{(Eq. 2.2)}$$

In Equation 2.2, *P'* is the lifetime average corrosion rate of a sample at time *t*, not an instantaneous penetration rate and requires an experimentally determined radius *r(t)*. However, direct measurement of the sample radius is not practicable. Therefore, the nominal and final CSAs, A_0 and *A(t)* respectively, were introduced as measurable quantities:

$$P' = \frac{\sqrt{\frac{A_0}{\pi}} - \sqrt{\frac{A(t)}{\pi}}}{t} \qquad \text{(Eq. 2.3)}$$

The penetration rates reported herein are calculated using Equation 2.3 and can be interpreted as true rates of radial reduction. The nominal cross sectional area, A_0, and the cross sectional area at time *t*, *A(t)*, are obtained in this study through image analysis as previously described. The change in measured CSA is expressed as a positive, normalized value, ΔA_C:

$$\Delta A_C = \frac{A_0 - A(t)}{A_0} \qquad \text{(Eq. 2.4)}$$

Fractional CSA reduction is a useful metric for expressing the total extent of corrosion, as it is approximately equal to the metallic volume loss.

2.2.4 Results

2.2.4.1 Trends from image analysis

An analysis to elucidate the composition and corrosion mechanism of the *in vivo* magnesium specimens, including discussion of the backscattered images, has been conducted and reported elsewhere [31], and will not be repeated. Measured cross sectional areas were used to calculate a penetration rate (*P'*) using Equation 2.3 in addition to ΔA_C for explanted (*in vivo*) magnesium wires from Equation 2.4 is presented in Figure 2.8(A), and the calculated penetration rate is presented in Figure 2.8(B). The fractional CSA reduction and calculated penetration rates for samples corroded *in vitro* are presented in Figure 2.9(A) and Figure 2.9(B), respectively. The number of sections used in this study was sufficient to identify a mean CSA reduction and penetration rate to

reasonable precision, as shown by the standard error bars in Figure 2.8 and Figure 2.9. (The use of μCT in future studies may improve the precision of these measurements.)

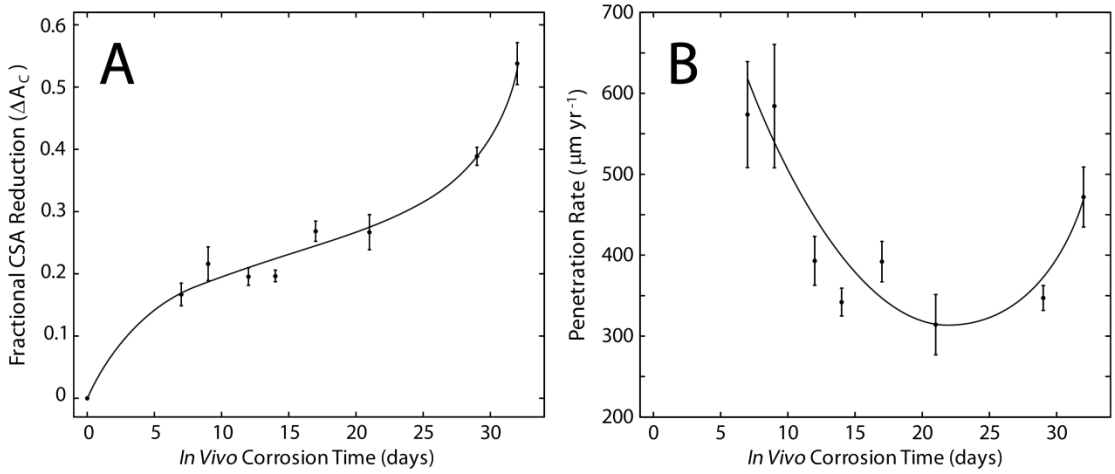

Figure 2.8 – Measured cross sectional area reduction (A) and calculated penetration rates (B) from specimens corroded *in vivo*. Error bars represent standard error from at least eight measurements. Trendlines were added to guide the eye.

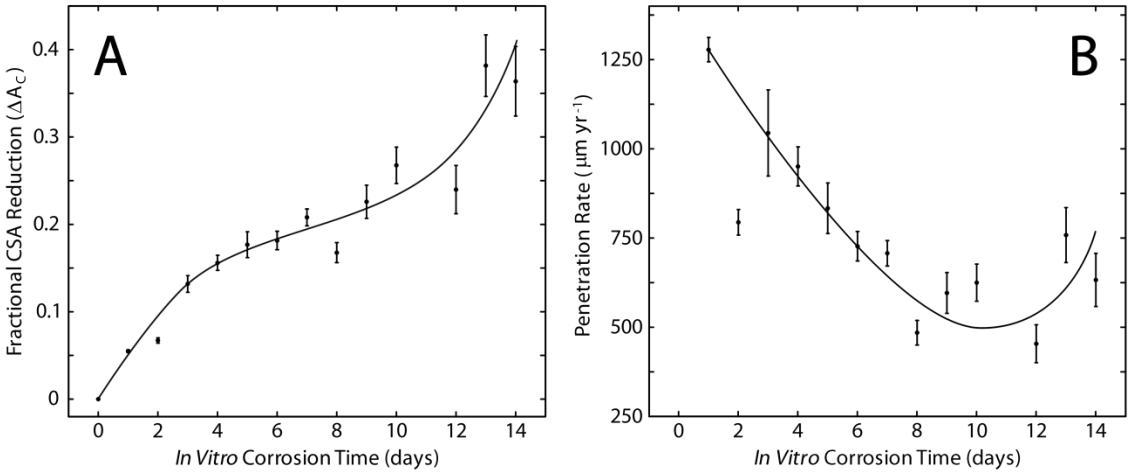

Figure 2.9 – Measured cross sectional area reduction (A) and calculated penetration rates (B) from specimens corroded *in vitro* using DMEM immersion. Error bars represent standard error from five measurements. Trendlines were added to guide the eye.

An apparent upward trend in CSA reduction [Figure 2.8(A) and Figure 2.9(A)] applies to both *in vivo* and *in vitro* samples. The CSA reduction data appear semi-linear in the central portion, for 7–21 days *in vivo* and 4–12 days *in vitro*. The slope of this segment seems to be lower than the rate of CSA reduction at the onset of corrosion (< 7 days *in vivo* and < 4 days *in vitro*), as well as during the late ("terminal") stages of corrosion, before *in situ* fracture of the samples. Terminal degradation was observed from 21 to 29 days *in vivo* and for 12–14 days *in vitro*. The temporal resolution of the data at early and late times is insufficient for hypothesis testing to confirm that the apparent differences in slope are significantly different.

Lifetime average penetration rates calculated for specimens corroded *in vivo* [Figure 2.8(B)] and *in vitro* [Figure 2.9(B)] are also visually similar with respect to time. The penetration rates *in vivo* were systematically lower than comparable rates *in vitro*, consistent with previous observations [19, 35]. Both environments produced rapid degradation at the onset of corrosion with a continuous decrease through the first ~21 days *in vivo* or ~8–9 days *in vitro*. Deceleration of corrosion may be interpreted, in part, as self-protective behavior akin to that previously reported for magnesium materials corroded *in vitro* [29, 30]. A minor increase in the penetration rate may have occurred in the terminal stages of corrosion. This would be in agreement with qualitative observations of locally accelerated late-stage corrosion in the same specimens [31]. However, instantaneous changes in corrosion rate were not readily accessible to the penetration rate definition used (Equation 2.3) due to ΔA_C being distributed evenly over

the entire lifetime of the sample. Sufficed to say, the penetration rate did not seem to decrease uniformly over the entire lifetime of the material.

2.2.4.2 Empirical modeling

In the absence of an analytical treatment to continuously describe corrosion rate in the complex physiological environment, mathematical modeling of CSA reduction and penetration rate was used as a substitute. A series of polynomials of increasing order (n) and associated regression coefficients β_i were employed to model the corrosion rate as a function of time:

$$P' = \sum_{i=0}^{n} \beta_i t^i \qquad \text{(Eq. 2.5)}$$

When the CSA reduction is expressed in terms of P' it is observed that $\Delta AC \propto P'^2 t^2$. Thus, when a penetration rate follows Equation 2.5 of order n, the CSA reduction is approximately described by a polynomial of order $2n + 2$.

To identify the minimum polynomial order that satisfies all measurements, both P' and ΔA_C were fit as polynomials with respect to time (Figure 2.10). The resulting regression parameters (t in days) and R^2 values, indicating goodness of fit, for each order are reported in Table 2.4. Visually, the penetration rates measured for *in vivo* and *in vitro* samples are not well described by a constant value ($n = 0$), nor by a linear ($n = 1$) correlation. The poor fit at low order is reflected in the R^2 values (Table 2.4), which are < 0.55 for $n \leq 1$. At $n = 2$, corresponding to a quadratic model of penetration rate, all data fall relatively close to the line of best fit with a concomitant increase in R^2 in both

environments. When the order is increased to $n = 3$ (cubic), the goodness of fit increases only marginally in both cases, and so the third term is not necessary. Unconstrained lines of best fit to CSA reduction measurements seemed to be of good quality at $n = 1$ or $n = 2$, corresponding to fitting polynomials of order 4 and 6, respectively. Again, an increase to $n = 3$ seems unnecessary. Thus, the penetration rate (P') of magnesium *in vivo* and *in vitro* is reasonably modeled by a second order polynomial, and the cross sectional area reduction consequently represented by a sixth order polynomial.

Table 2.4 – Regression parameters for the polynomial representation of penetration rate (Equation 2.5) corresponding to the best fit curves drawn in Figure 2.10.

In vivo							
Penetration Rate						*CSA Reduction*	
n	β_3	β_2	β_1	β_0	R^2	$2n + 2$	R^2
0				427.3	0.000	2	0.913
1			-5.241	519.6	0.207	4	0.982
2		1.344	-58.19	938.2	0.838	6	0.988
3	0.0091	0.8252	-49.48	895.8	0.839	8	1.000

In vitro							
Penetration Rate						*CSA Reduction*	
n	β_3	β_2	β_1	β_0	R^2	$2n + 2$	R^2
0				760.2	0.000	2	0.907
1			-39.88	1049	0.543	4	0.941
2		6.559	-138.7	1312	0.742	6	0.943
3	0.3195	-0.5997	-94.87	1249	0.747	8	0.974

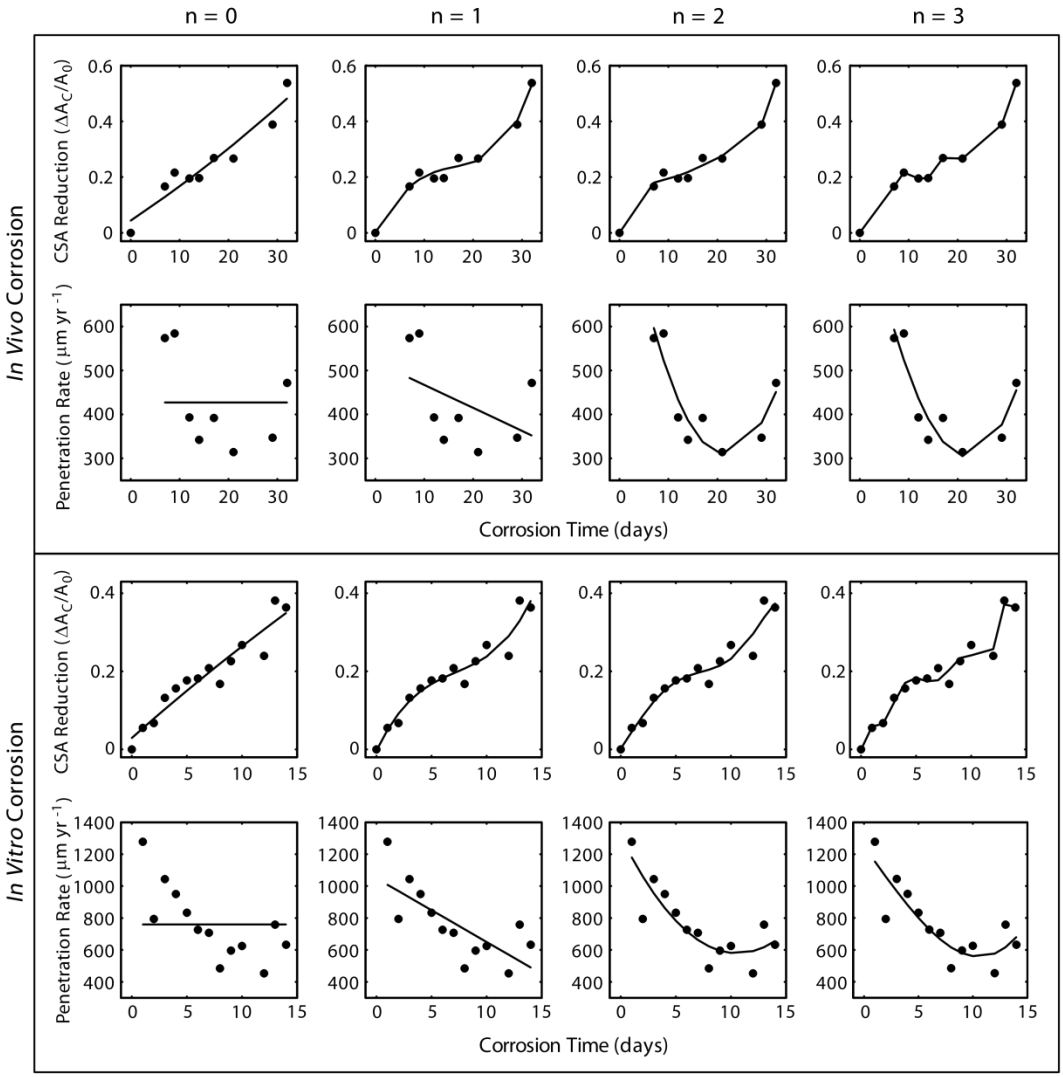

Figure 2.10 – Measured values (•) and predicted values (line) for samples corroded *in vivo* (top set) and *in vitro* (bottom set) for polynomial models. Error bars are omitted for clarity. Penetration rate is described by a polynomial of order *n* (Equation 2.5) and the CSA reduction is described by a polynomial of order 2*n* + 2.

2.2.4.3 Development of a correlation

Using the resulting empirical models, it was possible to construct a multiplier to correlate *in vitro* and *in vivo* corrosion. Because the corrosion times are scaled *in vitro* relative to

in vivo, it was not possible to define a multiplier as a function of time [25]. Instead, a correlation was described for a given fractional CSA reduction, thereby controlling for the severity of corrosion. The procedure employed in the analysis is illustrated in Figure 2.11 and may be summarized as:

i. a value of ΔA_C valid both *in vivo* and *in vitro* was selected;
ii. using the sixth order empirical model, *t* was found for the *in vitro* and *in vivo* environments separately such that ΔA_C was equivalent to the fixed value from (i);
iii. the *in vivo* and *in vitro* corrosion rates were determined at the respective *t* values determined in (ii) using the quadratic model; and
iv. the ratio of *P' in vitro* to *P' in vivo* from (iii) was plotted as a function of ΔA_C from (i).

The multiplier at each value of ΔA_C was calculated iteratively using MATLAB, and is depicted in Figure 2.11(C). Using this approach, the value obtained does not appear to be constant over the entire corrosion lifetime. Rather, the multiplier is 1.2–1.5× during the first 20% reduction in CSA, increasing to 1.7–1.9× at > 25% CSA reduction. The definition of *P'* in Equation 2.3 as a time-average quantity implies that the last value embodies all corrosion to that point and, therefore, should be reasonable at times close to implant failure. Using error propagation analysis with the fitting errors presented in Table 2.5, the multiplier standard error at the onset of corrosion was determined to be ± 0.2×.

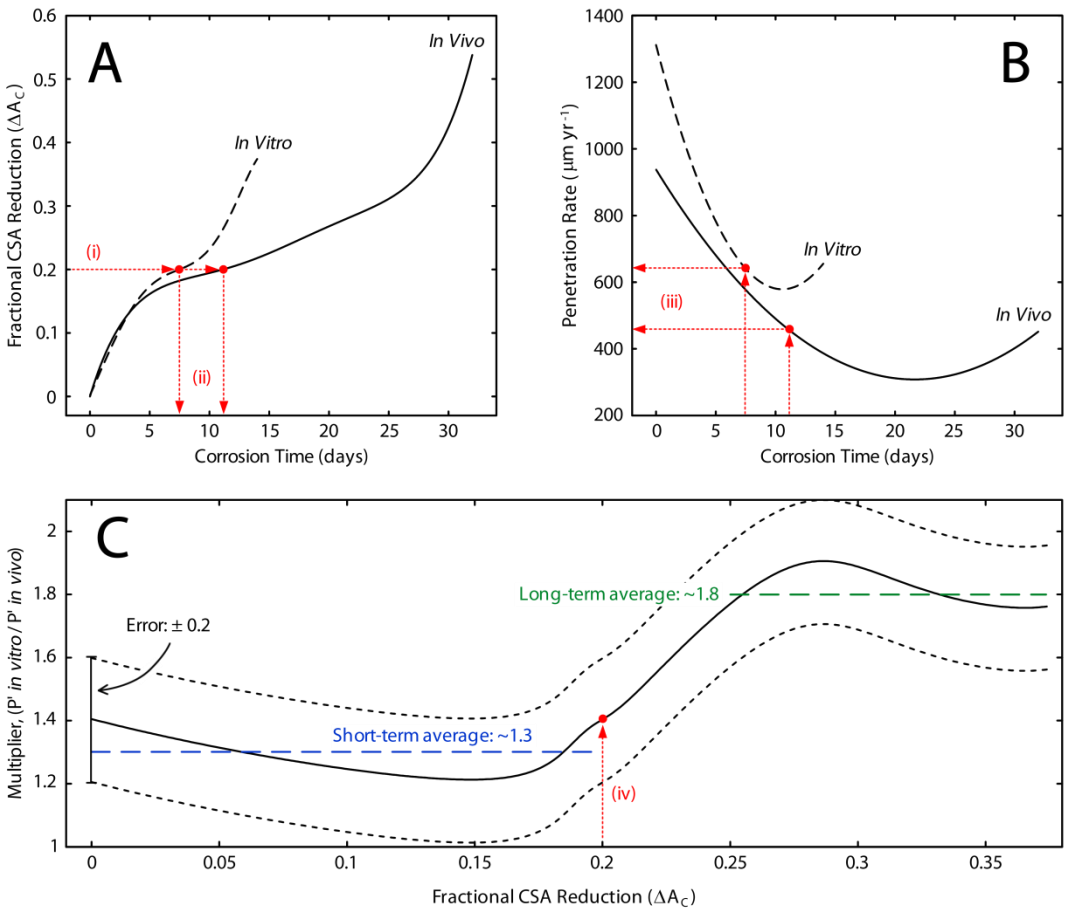

Figure 2.11 – CSA reduction (A) and penetration rate (B) models for the *in vitro* and *in vivo* environments were used to find an *in vivo-in vitro* multiplier (C). (i)–(iv) refer to the four steps used to calculate the multiplier as a function of ΔA_C.

Table 2.5 – Error in the quadratic regression parameters for penetration rate from Table 2.4

Environment	**Standard error**		
	β_2	β_1	β_0
In vivo	0.3039	12.15	103.0
In vitro	2.364	36.67	119.3

2.2.5 Discussion

We report here that trends for cross sectional area reduction (ΔA_C) and penetration rate (P') are similar *in vivo* (Figure 2.8) and *in vitro* (Figure 2.9). This suggests that *in vivo* corrosion progression—dissolution, self-protection, and late-stage breakdown—are loosely replicated *in vitro* using a DMEM solution. The *in vitro* corrosion in this study can be considered to be ~1.5× faster than *in vivo* degradation when an overall average is taken. It is known that the *in vitro* corrosion of magnesium is substantially faster than comparable *in vivo* degradation, and so this outcome was expected. Identification of the factors that contribute to the kinetic difference and clarification of their relative influences remains an open line of inquiry. Different sterilization methods employed on *in vivo* and *in vitro* samples may lead to different mechanical and corrosion behaviors at short times [40] (i.e. at times employed in most electrochemical studies). However, substantial surface conversion had occurred at even the earliest time points in this study, and so differences in surface condition are not likely to have affected any reported penetration rate measurements. Mueller *et al.* attributed kinetic differences largely to discrepancies in mass transport at the sample surface [19]. Willumeit *et al.* partially attributed the slow *in vivo* corrosion to the presence of organic constituents—amino acids, proteins, etc.—that are generally not present *in vitro* [35].

It is observed from a closer examination of Figure 2.11 that use of an overall average multiplier (~1.5×) in short-term corrosion studies will result in an overestimate of *in vivo* degradation. Its employment in long-term study is also inappropriate, as it would

underestimate the actual *in vivo* attack. It is suggested, therefore, to use a value of 1.3 ± 0.2× for corrosion experiments where mild degradation (i.e. ΔA_C < 20%) is observed. For longer-term experiments where a CSA reduction of ~25% or greater is realized, the higher late-stage multiplier of 1.8 ± 0.2× appears suitable. This constitutes the first report of a degradation-dependent kinetic discrepancy between the *in vitro* and *in vivo* environments.

The change in multiplier is interpreted here as a shift from "stage I" (initial dissolution and quasi-steady state degradation) to "stage II" degradation (terminal breakdown and subsequent implant fragmentation) at sufficiently large values of ΔA_C. The shift in multiplier may correspond to a change in the rate-limiting step in the corrosion process. It is supposed that the stage I limiting step is quasi-steady state mass transport through the duplex (hydroxyapatite and oxide/hydroxide) corrosion layer. In contrast, the stage II rate-limiting step was previously hypothesized to be governed by breakdown of the corrosion products [31]. It is therefore feasible that the limiting steps governing stage I and stage II corrosion are modulated differently by chemical and transport factors *in vivo* and *in vitro*. Environmental considerations referenced by Mueller *et al.* [19] and Willumeit *et al.* [35] remain relevant, but each may have different kinetic effects at each corrosion stage. Following from this, targeted improvements that shift the *in vitro* corrosion kinetics of one stage to match the other would improve the predictive power of non-animal corrosion tests by removing the apparent dependence of the numerical multiplier on corrosion severity.

Values of 1.3× and 1.8× (± 0.2×) in the short term and long term, respectively, are lower than previously derived correlations based on mechanical behavior [33]. The 2.3× value based on mechanical strength and the time-to-failure of samples examined was possibly subjected to secondary effects, which merit further investigation. One possibility is the convolution of degradation with semi-localized loss of material manifested as continuum damage effects [41]. A damage parameter that is larger *in vitro* than *in vivo* would explain an increase in the multiplier and could perhaps be attributed to mass transport factors like those considered by Mueller [19]. Employment of larger samples, 20 mm in length, may have also modified the *in vivo* or *in vitro* degradation behavior to produce a higher multiplier [22]. For modeling of stent mechanical behavior or performance (i.e. recoil) over time, the mechanically derived multiplier is appropriate. However, for the more common conventional corrosion analysis, the current work is superior.

The extent to which the multiplier values derived in this report may be applied to other materials, corrosion protocols, and sample geometries is not yet clear. It is likely that any changes to the materials and reagents used will require re-working of the numerical value of the multiplier. For example, use of a different corrosion solution, volume of solution, incubation conditions, the use of pH control, simulated flow, media replacement, and/or use of proteins or other supplements will affect the corrosion outcomes [19, 22]. Likewise, modifications to the *in vivo* protocol to utilize a subcutaneous or other implantation site will change the corrosion behavior. The general approach employed here is relevant for a wide variety of implant shapes. However, a more appropriate

method of analysis, such as μCT, and more nuanced treatment of the data would be necessary for complex geometries. Changes in the material including processing, purity, and alloying are likely to modify the early-stage corrosion mechanism [27] and will also necessitate re-derivation of the *in vivo-in vitro* multiplier. Despite sensitivity to materials and methods, the corrosion-based approach presented here is widely applicable to degradable metallic stent materials and should therefore be of great utility in future work.

2.2.6 Conclusions

In this study, an *in vitro-in vivo* biocorrosion correlation for magnesium based on penetration rate has been developed. Results apply to commercially pure magnesium corroded in the murine artery and in DMEM immersion testing. Multipliers calculated for a fixed cross sectional area reduction ranged from 1.2–1.9 ± 0.2×. Suggested multipliers are 1.3 ± 0.2× for samples < 20% degraded, and 1.8 ± 0.2× for samples that are > 25% corroded. This constitutes a kinetic difference that is dependent on the total corrosion severity (ΔA_C). Multiplier determination beyond a 35% reduction in the CSA was not feasible due to fragmentation of the samples corroded *in vitro*.

2.2.7 Appendix

For uniform corrosion of a typical sample in the form of a coupon or other standard geometry, the penetration rate (P) is defined as:

$$\mathrm{P} = -\frac{\Delta \mathrm{M}}{\rho \mathrm{A_s t}} \qquad \text{(Eq. 2.6)}$$

Here, ΔM is the change in mass measured at time t for an object of density ρ and surface area A_S. This metric has great utility in quantifying the corrosion of metals, and its physical significance is apparent for most geometries. The penetration rate, which carries units of length per time (i.e. mm yr^{-1}), corresponds directly to the thickness of material lost during uniform attack distributed over a surface.

The geometry used in this work is a small cylinder with a high aspect ratio (80:1) that undergoes significant degradation. This geometry is comparable to a single stent strut. The cylindrical face of the wire sample comprises 99.4% of the total surface area of the specimen, and so this is considered to be the only surface affected by corrosion. Degradation taking place lengthwise is therefore ignored. Because ρ for the intact metal is constant, $\Delta M/\rho = \Delta V$, where ΔV is the change in the volume of the specimen during the corrosion process. Recognizing that corrosion is approximately independent of the sample length, $\Delta V/A_S \approx \Delta A_C/p$, where ΔA_C is a measured change in the CSA and p is the perimeter of the cross section. Under uniform corrosion conditions, P can be expressed in terms of the nominal radius (r_0) and radius of the remaining metal at time t, $r(t)$:

$$P = \frac{r_0^2 - r(t)^2}{2 r_0 t} \qquad \text{(Eq. 2.7)}$$

Equation 2.7 may be rearranged to give an expression for $r(t)$ for a given penetration rate:

$$r(t) = \sqrt{r_0^2 - 2 P r_0 t} \qquad \text{(Eq. 2.8)}$$

Equation 2.8 demonstrates that $r(t)$ does not decrease linearly with t, but rather with $t^{1/2}$. This is at odds with the reasonable expectation that a constant penetration rate would

correlate to a linearly increasing depth of penetration. Therefore, the conventional penetration rate metric is not appropriate for the wire geometry employed in this study.

2.2.8 Acknowledgements

PKB was supported by fellowship funds from the DeVlieg Foundation and the American Heart Association. AD would like to express appreciation to the Institute of Materials Processing at Michigan Technological University for support over the course of this study. Owen Mills and Felicia Nip of the Applied Chemical and Morphological Analysis Laboratory at Michigan Tech are acknowledged for their help in preparing samples for electron microscopy.

2.2.9 References

[1] Mani G, Feldman MD, Patel D, Agrawal CM. Coronary stents: a materials perspective. Biomaterials 2007;28:1689-1710.

[2] Witte F, Hort N, Vogt C, Cohen S, Kainer KU, Willumeit R, Feyerabend F. Degradable biomaterials based on magnesium corrosion. Curr Opin Solid State Mater 2008;12:63-72.

[3] Hermawan H. Biodegradable metals for cardiovascular applications. Biodegradable metals: from concept to applications. Heidelberg: Springer; 2012. p 23-37.

[4] Kirkland NT. Magnesium biomaterials: past, present and future. Corros Eng Sci Techn 2012;47:322-328.

[5] Zainal Abidin NI, Martin D, Atrens A. Corrosion of high purity Mg, AZ91, ZE41 and Mg-2Zn-0.2Mn in Hank's solution at room temperature. Corros Sci 2011;53:862-872.

[6] Walker J, Shadanbaz S, Kirkland NT, Stace E, Woodfield T, Staiger MP, Dias GJ. Magnesium alloys: predicting *in vivo* corrosion with *in vitro* immersion testing. J Biomed Mater Res B 2012;100B:1134-1141.

[7] Kalb H, Rzany A, Hensel B. Impact of microgalvanic corrosion on the degradation morphology of WE43 and pure magnesium under exposure to simulated body fluid. Corros Sci 2012;57:122-130.

[8] Choudhary L, Raman RK. Magnesium alloys as body implants: fracture mechanism under dynamic and static loadings in a physiological environment. Acta Biomater 2012;8:916-923.

[9] Bowen PK, Drelich J, Buxbaum RE, Rajachar RM, Goldman J. New approaches in evaluating metallic candidates for bioabsorbable stents. Emer Mater Res 2012;1:237-255.

[10] Yang L, Huang Y, Feyerabend F, Willumeit R, Kainer KU, Hort N. Influence of ageing treatment on microstructure, mechanical and bio-corrosion properties of Mg–Dy alloys. J Mech Behav Biomed 2012;13:36-44.

[11] Pierson D, Edick J, Tauscher A, Pokorney E, Bowen PK, Gelbaugh J, Stinson J, Getty H, Lee CH, Drelich J, Goldman J. A simplified *in vivo* approach for evaluating the bioabsorbable behavior of candidate stent materials. J Biomed Mater Res B 2012;100B:58-67.

[12] Mueller PP, Arnold S, Badar M, Bormann D, Bach FW, Drynda A, Meyer-Lindenberg A, Hauser H, Peuster M. Histological and molecular evaluation of iron as degradable medical implant material in a murine animal model. J Biomed Mater Res A 2012;100:2881-2889.

[13] Bowen PK, Drelich J, Goldman J. Zinc exhibits ideal physiological corrosion behavior for bioabsorbable stents. Adv Mater 2013;25:2577-2582.

[14] Heublein B, Rohde R, Kaese V, Niemeyer M, Hartung W, Haverich A. Biocorrosion of magnesium alloys: a new principle in cardiovascular implant technology? Heart 2003;89:651-656.

[15] Di Mario C, Griffiths H, Goktekin O, Peeters N, Verbist J, Bosiers M, Deloose K, Heublein B, Rohde R, Kasese V. Drug-eluting bioabsorbable magnesium stent. J Interv Cardiol 2004;17:391-395.

[16] Waksman R, Pakala R, Okabe T, Hellinga D, Chan R, Tio MO, Wittchow E, Hartwig S, Waldmann KH, Harder C. Efficacy and safety of absorbable metallic stents with adjunct intracoronary beta radiation in porcine coronary arteries. J Interv Cardiol 2007;20:367-372.

[17] Slottow TL, Pakala R, Okabe T, Hellinga D, Lovec RJ, Tio FO, Bui AB, Waksman R. Optical coherence tomography and intravascular ultrasound imaging of bioabsorbable magnesium stent degradation in porcine coronary arteries. Cardiovasc Revasc Med 2008;9:248-254.

[18] Wittchow E, Adden N, Riedmuller J, Savard C, Waksman R, Braune M. Bioresorbable drug-eluting magnesium-alloy scaffold: design and feasibility in a porcine coronary model. EuroIntervention 2013;8:1441-1450.

[19] Mueller WD, Lucia Nascimento M, Lorenzo de Mele MF. Critical discussion of the results from different corrosion studies of Mg and Mg alloys for biomaterial applications. Acta Biomater 2010;6:1749-1755.

[20] Gu X, Zheng Y, Cheng Y, Zhong S, Xi T. *In vitro* corrosion and biocompatibility of binary magnesium alloys. Biomaterials 2009;30:484-498.

[21] Kirkland NT, Lespagnol J, Birbilis N, Staiger MP. A survey of bio-corrosion rates of magnesium alloys. Corros Sci 2010;52:287-291.

[22] Kirkland NT, Birbilis N, Staiger MP. Assessing the corrosion of biodegradable magnesium implants: a critical review of current methodologies and their limitations. Acta Biomater 2012;8:925-936.

[23] Dreher M, Anderson S. ASTM-FDA workshop on absorbable medical devices: Lessons learned from correlations of bench testing and clinical performance. Silver Spring, MD: Department of Health and Human Services, Food and Drug Administration; 2012.

[24] Witte F, Fischer J, Nellesen J, Crostack H-A, Kaese V, Pisch A, Beckmann F, Windhagen H. *In vitro* and *in vivo* corrosion measurements of magnesium alloys. Biomaterials 2006;27:1013-1018.

[25] Deng CZ, Radhakrishnan R, Larsen SR, Boismer DA, Stinson JS, Hotchkiss AK, Petersen EM, Weber J, Scheuermann T. Magnesium alloys for bioabsorbable stents: a feasibility assessment. In: Sillekens WH, Agnew SR, Neelameggham NR, Mathaudhu SN, editors. Magnesium Technology 2011.Warrendale, PA: The Minerals, Metals & Materials Society; 2011. p 413-418.

[26] Song G, Atrens A. Corrosion mechanisms of magnesium alloys. Adv Eng Mater 1999;1:11-33.

[27] Atrens A, Liu M, Zainal Abidin NI. Corrosion mechanism applicable to biodegradable magnesium implants. Mater Sci Eng B 2011;176:1609-1636.

[28] Atrens A, Song G-L, Cao F, Shi Z, Bowen PK. Advances in Mg corrosion and research suggestions. Journal of Magnesium and Alloys 2013;1:177-200.

[29] Wu G, Zhao Y, Zhang X, Ibrahim JM, Chu PK. Self-protection against corrosion of aged magnesium alloy in simulated physiological environment. Corros Sci 2013;68:279-285.

[30] Kim W-C, Han K-H, Kim J-G, Yang S-J, Seok H-K, Han H-S, Kim Y-Y. Effect of surface area on corrosion properties of magnesium for biomaterials. Met Mater Int 2013;19:1131-1137.

[31] Bowen PK, Drelich J, Goldman J. Magnesium in the murine artery: Probing the products of corrosion. Acta Biomater 2014;10:1475-1483.

[32] Seitz JM, Eifler R, Bach F, Maier H. Magnesium degradation products: Effects on tissue and human metabolism. J Biomed Mater Res A 2014;102A:3744-3753.

[33] Bowen PK, Drelich J, Goldman J. A new *in vitro-in vivo* correlation for bioabsorbable magnesium stents from mechanical behavior. Mater Sci Eng C 2013;33:5064-5070.

[34] Bowen PK, Gelbaugh JA, Mercier PJ, Goldman J, Drelich J. Tensile testing as a novel method for quantitatively evaluating bioabsorbable material degradation. J Biomed Mater Res B 2012;100B:2101-2113.

[35] Willumeit R, Fischer J, Feyerabend F, Hort N, Bismayer U, Heidrich S, Mihailova B. Chemical surface alteration of biodegradable magnesium exposed to corrosion media. Acta Biomater 2011;7:2704-2715.

[36] Scheideler L, Fuger C, Schille C, Rupp F, Wendel HP, Hort N, Reichel HP, Geis-Gerstorfer J. Comparison of different *in vitro* tests for biocompatibility screening of Mg alloys. Acta Biomater 2013;9:8740-8745.

[37] Rasband WS. ImageJ. Bethesda, Maryland: National Institutes of Health; 1997.

[38] Beers Y. Introduction to the Theory of Error, 2nd ed. Reading, MA: Addison-Wesley; 1957.

[39] Jones DA. Principles and prevention of corrosion. Prentice Hall; 1996.

[40] Seitz JM, Collier K, Wulf E, Bormann D, Angrisani N, Meyer-Lindenberg A, Bach F-W. The effect of different sterilization methods on the mechanical strength of magnesium based implant materials. Adv Eng Mater 2011;13:1146-1151.

[41] Gastaldi D, Sassi V, Petrini L, Vedani M, Trasatti S, Migliavacca F. Continuum damage model for bioresorbable magnesium alloy devices - Application to coronary stents. J Mech Behav Biomed Mater 2011;4:352-365.

3 *In vivo* corrosion mechanism

3.1 Magnesium in the murine artery: probing the products of corrosion[5]

3.1.1 Abstract

Many publications are available on the physiological and pseudophysiological corrosion of magnesium and its alloys for bioabsorbable implant application, yet few focus on characterization of explanted materials. In this work, commercially pure magnesium wires were corroded in the arteries of rats for up to one month, removed, and both bulk and surface products were characterized. Surface characterization using infrared spectroscopy revealed a duplex structure comprising heavily magnesium-substituted hydroxyapatite that later transformed into an A-type (carbonate-substituted) hydroxyapatite. To explain this transformation, an ion-exchange mechanism is suggested. Elemental mapping of the bulk products of biocorrosion revealed the elemental distribution of Ca, P, Mg, and O in the outer and Mg, O, and P in inner layers. Carbon was not observed in any significant quantity from the inner corrosion layer, suggesting that carbonates are not a prevalent product of corrosion. Backscatter electron imaging of cross sections showed that thinning or absence of the hydroxyapatite in the later stages of degradation is related to local thickening of the inner corrosion layer. Based on these experimental observations, mechanisms describing corrosion in the quasi-steady state and during terminal breakdown of the magnesium specimens are proposed.

[5] The material in Section 3.1 was previously published in *Acta Biomaterialia* and is reproduced here with permission.

P. K. Bowen, J. Drelich, and J. Goldman. "Magnesium in the murine artery: probing the products of corrosion." *Acta Biomater.* 10(3) 1475-1483 (2014), doi: 10.1016/j.actbio.2013.11.021.

References in Section 3.1 follow the *Acta Biomaterialia* author guidelines.

3.1.2 Introduction

Magnesium and its alloys have been heavily researched in recent years due to interest in their application as bioabsorbable vascular scaffolding [1]. Prior to widespread clinical adoption, extensive *in vitro* and *in vivo* corrosion testing is required. While there is a plethora of corrosion data from *in vitro* experiments [2], it appears that *in vivo* study is a major deficiency of the absorbable stent literature. Most contributions thus far have relied on porcine arterial implants [3-6] or are based on clinical (human) experience [7-10]. Very few contain appropriate descriptions of material degradation, and, of these, none completely disclose their corrosion analyses. A lack of disclosure is likely related to intellectual property concerns. Even so, some mechanisms and products of magnesium corrosion have become common knowledge, such as the general tendency for magnesium to form an oxygen-bearing product: MgO, $Mg(OH)_2$, a Mg carbonate, or a mixture thereof [6, 11]. Several references are made to the gradual replacement of magnesium by calcium and phosphorus *in vivo* [5, 6, 8, 9].

Characterization of the explanted stent materials and identification of the products thereby generated is critical to the maturation of this class of absorbable implants. For this reason, among others, two recent reviews of *in vitro* corrosion methodology called for detailed *in vivo* studies [2, 12]. Wittchow *et al*. [6] recently reported useful cross sectional data from an explanted stent corroded in a porcine model using energy dispersive X-ray spectroscopy. They noted two corrosion layers: an inner layer that they concluded could be either $MgCO_3$ or $Mg(OH)_2$, and an outer layer comprised of an

amorphous calcium phosphate. Elemental maps related to secondary components of the corrosion layer (e.g. rare earth-bearing oxides, aluminum, zinc, etc.) are not disclosed, nor are the X-ray diffraction patterns referenced in the report. Nevertheless, this seems to represent the most complete published material characterization of an explanted magnesium cardiovascular device to date.

The conventional method of stent fabrication and animal testing involves laser cutting and electropolishing a stent that is then implanted into a porcine model. This approach is generally inaccessible to academic researchers due to the expense of stent tube production and laser cutting, restrictions on the large animal subjects, and relatively high institutional and marginal costs of housing. As an alternative, an inexpensive *in vivo* method of biocorrosion simulation using wires [13, 14] or strip-shaped [15] samples implanted in the arterial walls of rats was recently developed by the authors. The wire geometry simulates the dimensions of a stent strut and lends itself to many analyses, including mechanical evaluation [16] and formulating quantitative relationships between *in vivo* and *in vitro* tests [17].

An improved understanding of the corrosion mechanism at later stages of degradation has the potential to expose new routes for improving the corrosion resistance of magnesium stent materials through surface modification and/or alloying. Additionally, understanding the stages of degradation directly preceding fragmentation has great engineering value. It would allow designers to anticipate a loss of scaffolding function in an absorbable stent. Here, the corrosion products on magnesium in the murine aortic wall are examined at

times varying from five days to functional degradation (failure) of the implant at 32 days. Optical microscopy, microscopic Fourier transform infrared spectroscopy (μFT-IR), cross sectioning, electron imaging, and elemental mapping have been used to characterize the explants. Identification of corrosion products with relevance to the long-term degradation mechanism of magnesium is thus pursued.

3.1.3 Methods and Materials

3.1.3.1 Corrosion protocol

Magnesium wire of 99.9% purity and 250 ± 25 μm diameter was purchased from Goodfellow (Coraopolis, Pennsylvania). Per specification, typical impurities included < 1 ppm Ag, 10 ppm Ca, 5 ppm Cu, 100 ppm Fe, 300 ppm Mn, < 1 ppm Na, and 100 ppm Si. The iron content is above the typical tolerance limits [18, 19], and so some degree of microgalvanic action is expected. The wire was divided into 10 and 20 mm segments and the ends smoothed with 800-grit sandpaper to remove any burrs that may hinder implantation. The wires were then cleaned with ethyl alcohol to remove dust and other surface contaminants.

Adult male Sprague Dawley rats were anesthetized with isoflurane in oxygen. The 10 mm wire segments were used to puncture the arterial adventitia of the abdominal aorta, and the wire was led in for the full length, thus firmly embedding it in the arterial media. 20 mm segments were implanted proximally to the first wire, within the abdominal aorta, and, after explantation, were used for mechanical analysis that is reported elsewhere [17].

It is noted that the arterial wall implantation method lacks some features of a fully expanded magnesium stent of the same material, including: (i) a lack of direct blood contact meant to simulate a post-encapsulation environment, (ii) an absence of local cold work that would modify the corrosion kinetics, and (iii) freedom from the cyclic stresses generally experienced by stents. This procedure was reviewed and approved by Michigan Technological University's Institutional Animal Care and Use Committee (IACUC).

Rats were housed until their euthanization in accordance with the Panel on Euthanasia of the American Veterinary Medical Association and extrication of the wires at ten time points ranging from 5 to 32 days. During the removal procedure, it was confirmed by visual examination that the implants had not shifted to a position outside the arterial media or adventitia. The 32 day sample was observed to be fragmented *in situ*, constituting "functional degradation," defined elsewhere [17]. The explants were cleared of biological fluids by wicking away surface moisture with a soft cloth and stored in a desiccated environment prior to analysis with optical microscopy, scanning electron microscopy (SEM), μFT-IR, and cross sectioning.

3.1.3.2 Explant analyses

Examination of the wires was carried out in a specific order to avoid chemically modifying the corrosion layers. Techniques that do not subject the sample to vacuum or impact of high-energy particles are unlikely to affect the chemical profile of the surface, particularly waters of hydration. For this reason, optical examination and μFT-IR were

performed first. SEM imaging of the surface, cross sectioning, and examination of the cross sections were conducted afterwards.

3.1.3.2.1 Optical imaging of the surface

Optical imaging of the corroded wire samples was performed with a Wild Heerbrugg M5a stereomicroscope and a Leica EC3 microscope camera (Leica Microsystems; Buffalo Grove, Illinois) at 50× nominal magnification. White-light illumination and exposure settings were the same from sample-to-sample to produce comparable images.

3.1.3.2.2 Microscopic Fourier transform infrared spectroscopy

μFT-IR was conducted in diffuse reflectance mode with a Jasco FTIR-4200 spectrophotometer equipped with an IRT-3000 microscope attachment. The IR microscope was used to limit the infrared light exposure to a ~250×500 μm representative area on each sample. A series of 1024 scans were performed at 1 cm^{-1} resolution from 600 to 4000 cm^{-1}. Background correction and a center-weighted boxcar smoothing algorithm were used to correct the data. Peak modeling was performed using peak-o-mat [20], an open source, Python-based software package.

3.1.3.2.3 Electron imaging of the surface

Scanning electron microscopy performed on the surface was done using a JEOL JSM-6400 (Peabody, Massachusetts) research-grade thermionic emission SEM. An accelerating voltage of 5 kV and reduced beam current was used for all samples. Only

secondary electron imaging was used to characterize the wire surfaces. A thermionic emission SEM (vacuum level of ~10^{-6} Torr) was preferred to a field emission SEM (~10^{-8} Torr) because dehydration of the sample degrades the high vacuum and poses a contamination risk to the emission tip.

3.1.3.2.4 Cross sectional analysis

Following the above analyses, the wires were placed in plastic sample clips and mounted in two-part epoxy inside a silicone tube (~8 mm inner diameter). After curing, the mounted wires were removed from the silicone tubes. The ends of the corroded wires—deformed by cutting—were avoided for this analysis; sectioning began at a minimum distance of 0.5 mm from the end of the wire. Cross sections were prepared by grinding the exposed wire in a metallographic fashion with 600- and 800-grit SiC paper and polishing with a 1 μm Al_2O_3 slurry on microfiber. The polished end was then cut to create a section of 0.8–1 mm thickness. The newly exposed surface was ground, polished, and sectioned as before to produce multiple sections. A representative section of good quality from four time points (7, 14, 21, and 32 days) was selected for detailed analysis.

The embedded sections of wire were carbon-coated to improve conductivity and then imaged with the JEOL JSM-6400 SEM, this time using its backscattered electron detector to provide phase contrast. Elemental mapping via energy dispersive spectroscopy (EDS) was performed using a 4pi Analysis system (Hillsborough, North Carolina) with a Si(Li) detector. Elemental maps for magnesium, oxygen, carbon, phosphorus, calcium,

chlorine, and sodium based on K_α radiation were captured at a 512 × 512 pixel resolution at 1500× nominal magnification. A detector dead time of ≥ 40% and pixel dwell time of 30 ms ensured a sufficient number of X-rays detected for each pixel.

3.1.4 Results

3.1.4.1 Surface imaging with optical and electron microscopy

Microscopic examination under identical exposure conditions indicated that several optically distinct products were concurrently present on the magnesium sample surfaces at most time points in this study. A progression in optical character is shown by the stereomicrographs presented in Figure 3.1. The 5 day time point had an oddly uniform appearance, from which the 7 day sample did not clearly follow. Secondary electron images (Figure 3.2) revealed formations on the surface consistent with the morphology and size of murine erythrocytes [21]. The biological material on the surface precluded using the 5 day sample for analysis via infrared spectroscopy, as a large amount of proteins, cells, and other biological constituents on the surface would create extraneous absorbance bands.

Comparison of the other sample surfaces pointed to clear differences. There were no strong indications of pitting or localized attack that reduced the apparent diameter of implants removed before 29 days. A thin, translucent, white surface layer was evident on the wire implanted for 12 days, and was morphologically different from the localized deposits previously observed. A similar translucent white layer appeared to cover nearly

the entire 14 day sample as well as wires from subsequent time points. On the 29 and 32 day specimens, the white overlayer seemed mostly opaque. Mild damage was observed on the surface at 29 days in roughly three locations along the length of the sample, and the material loss seemed to be limited to the opaque surface product. At the point of failure—32 days—damage was severe along the entire length of the wire and was again dominated by a fragmentation or spalling of surface product.

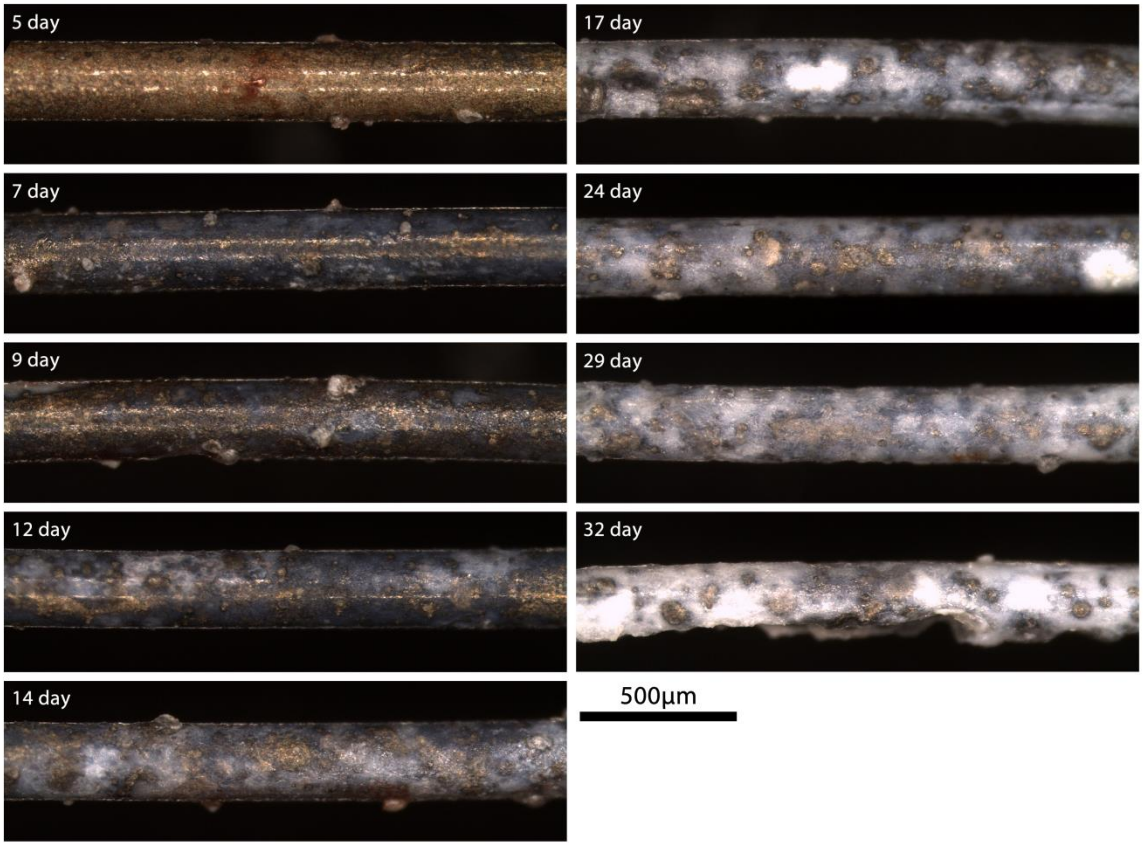

Figure 3.1 – A progression in the optical character of the corrosion layer is observed in the implants with increasing implantation time. All images were captured at 50× nominal magnification; the scale bar at lower right applies to all stereomicrographs.

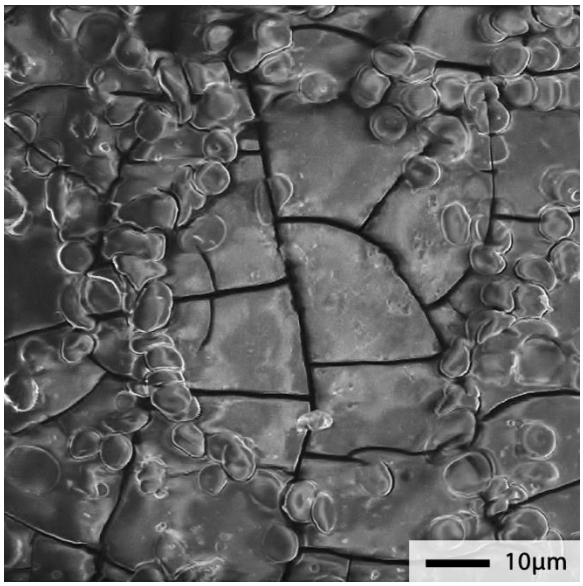

Figure 3.2 – Secondary electron image showing the adhesion of red blood cells to the magnesium wire surface after five days *in vivo*.

3.1.4.2 Fourier transform infrared spectroscopy

Infrared spectroscopy is ideal for determining the surface products present on explanted magnesium wires, as it carries absorption information from only a few surface micrometers [22]. General spectra, comprising absorption from all surface phases, are presented in Figure 3.3, and the major bands observed are listed in Table 3.1 [23-27]. No sharp band at 3275 cm^{-1}, corresponding to $Mg(OH)_2$ [28], was observed on the explant surfaces. A major shift in the spectral character was observed between days 12 and 14 consisting of the emergence of an independent H-O-H bending band, a strengthened carbonate ν_3 vibration, and a broadening of the phosphate ν_3 band. H-O-H bands and high-wavenumber OH^- vibrational modes (the latter are not shown) indicated the surface was continuously and strongly hydrated. An increase in H-O-H band intensity at 14 days qualitatively signifies a change in hydration of the surface product. This change is in

agreement with optical evidence of an emerging white-colored surface layer at 14 days (Figure 3.1).

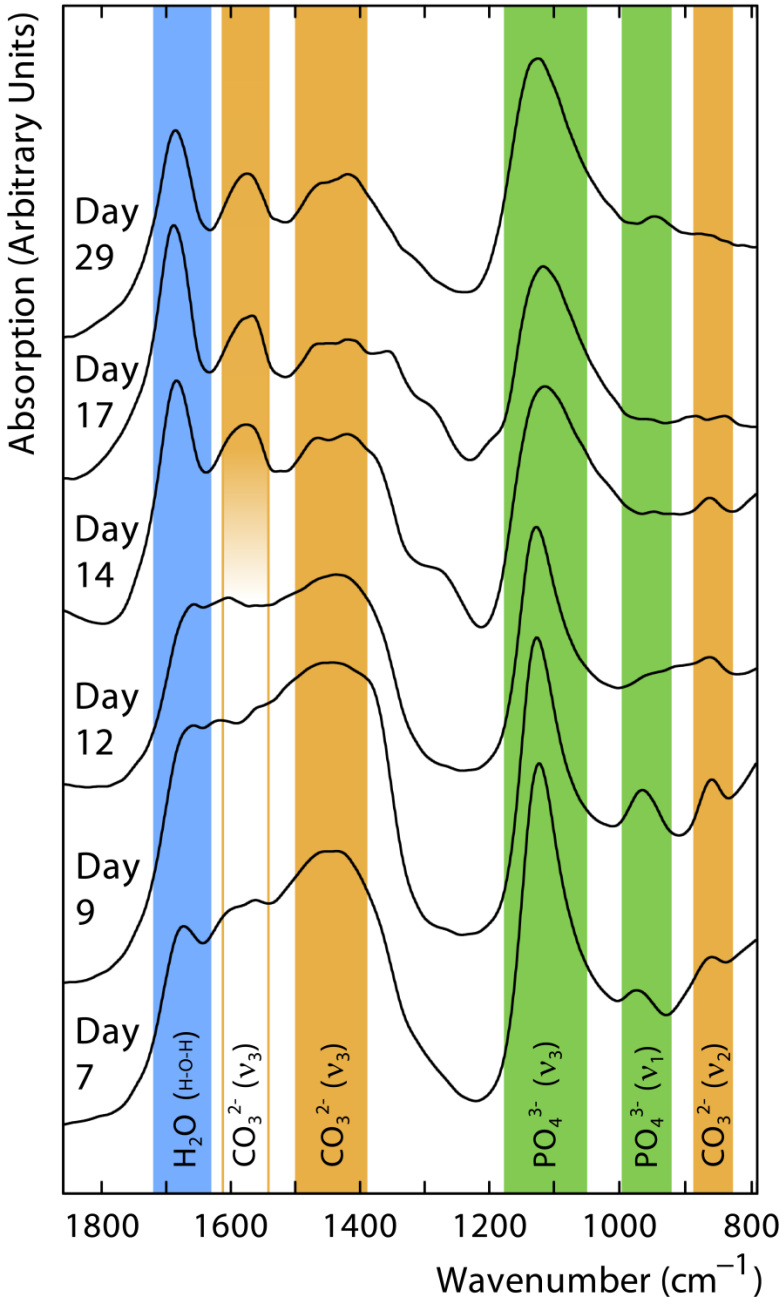

Figure 3.3 – General infrared spectra captured from the wires at time points through 29 days.

Table 3.1 – Infrared bands observed in the general FTIR spectra (Figure 3.3)

IR Band (cm^{-1})	**Attribution**	**Reference**
830-890	CO_3^{2-} (ν_2)	[23, 24]
920-1000	PO_4^{3-}, symmetric stretching (ν_1)	[25]
1050-1180	PO_4^{3-}, antisymmetric stretching (ν_3)	[26]
1390-1500	CO_3^{2-}, apatitic substitution (ν_3)	[23, 27]
1540-1620	CO_3^{2-}, apatitic substitution (ν_3)	[23, 27]
1660-1710	H_2O, H-O-H bending	[24, 26]

Gibson and Bonfield [23] were able to determine the mode of carbonate substitution in HAp based on the relative size of two peaks: A-type substitution, where carbonate is substituted for hydroxyl ions, results in ν_2 absorption at 880 cm^{-1}; alternatively, B-type substitution, where carbonate occupies a phosphate site, produces a ν_2 peak at 873 cm^{-1}. Peak modeling was used to extract the intensities of these two peaks between 14 and 29 days *in vivo* (Figure 3.4). It was observed that peak intensities remained relatively constant for A-type substitution, and varied by only ± 10%. Intensities corresponding to B-type substitution, however, declined by nearly an order of magnitude over the same time period.

Spectrum subtraction was utilized to isolate an IR spectrum for the first-to-form surface product. A small island of the second-to-form product was visible at 7 days; it was analyzed and the acquired spectrum was subtracted from the general scan (Figure 3.3). The corresponding spectra for the two surface products are presented in Figure 3.5 with the important carbonate, phosphate, and water bands highlighted. The spectrum of the

first-to-form substance was markedly different from the second-to-form product; it contained a stunted H-O-H bending band, a unified carbonate ν_3 band, and relatively narrow phosphate ν_1 and ν_3 bands.

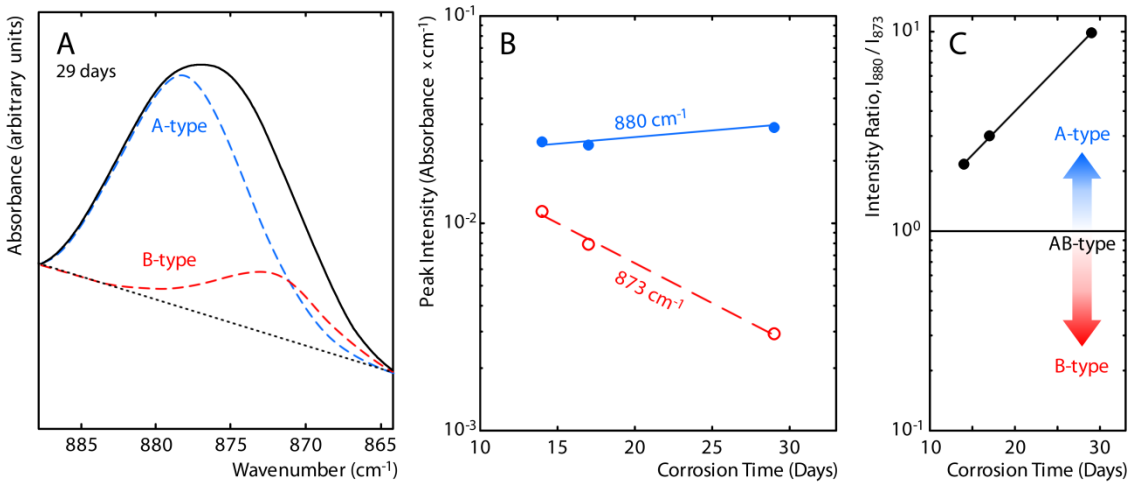

Figure 3.4 – Peak modeling—an example of which is shown for the 29 day time point (A)—yielded peak intensities for characteristic of A-type carbonate substitution (880 cm^{-1}) and B-type substitution (873 cm^{-1}) that are depicted with a solid line and broken line, respectively (B). A ratio of the former to the latter is consistently greater than unity, indicating A-type carbonate substitution in the surface product (C).

3.1.4.3 Cross sectional analysis

The elemental composition of bulk corrosion products that had accrued *in vivo* was also of interest in the present study. Polished cross sections of the corroded magnesium materials were analyzed to this end. A total of 73 sections (8–9 sections at each of eight time points) were produced and analyzed in the course of this study to give the authors a general sense of corrosion progression. Representative backscattered electron images (BEIs) corresponding to 7, 14, 21, and 32 day time points are presented in Figure 3.6 and Figure 3.6Figure 3.7 at 300× and 1500× nominal magnification, respectively. Four

distinct regions are apparent at first glance. From inside-to-outside, they are: (i) the inner magnesium wire, which appears bright; (ii) a relatively dark, low atomic number corrosion product adjacent to the wire (the "inner layer"); (iii) a high atomic number product on the outermost surface of the sample (the "outer layer"); and (iv) the darkest region, a low atomic number epoxy surrounding the specimens. The bright exterior can be attributed to the previously identified HAp layer, which gave a strong backscatter signal because of its calcium and phosphorus content.

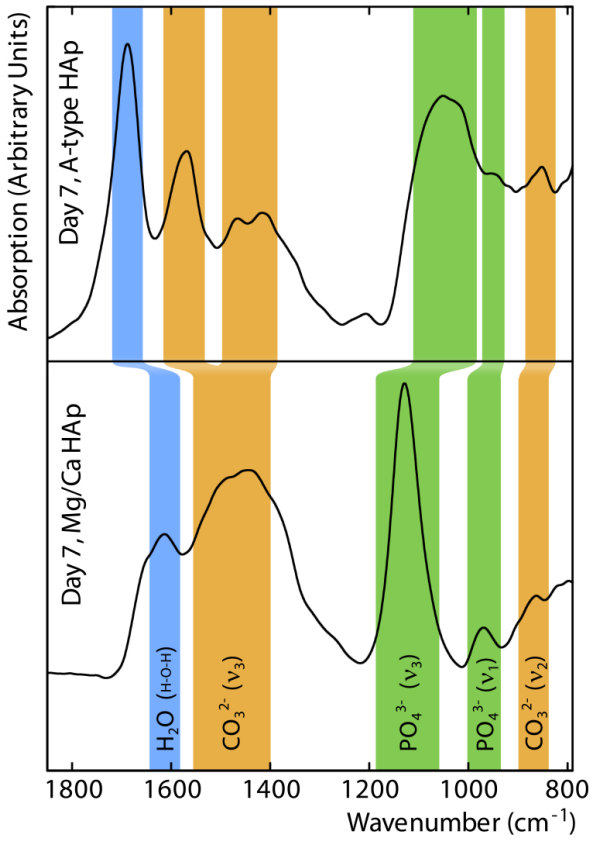

Figure 3.5 – Comparison of the spectra from the first-to-form product (Mg/Ca HAp) and second-to-form, white colored product (A-type HAp) at 7 days. The Mg/Ca HAp was generated by subtraction of the A-type HAp spectrum from an overall surface spectrum (Figure 3.3).

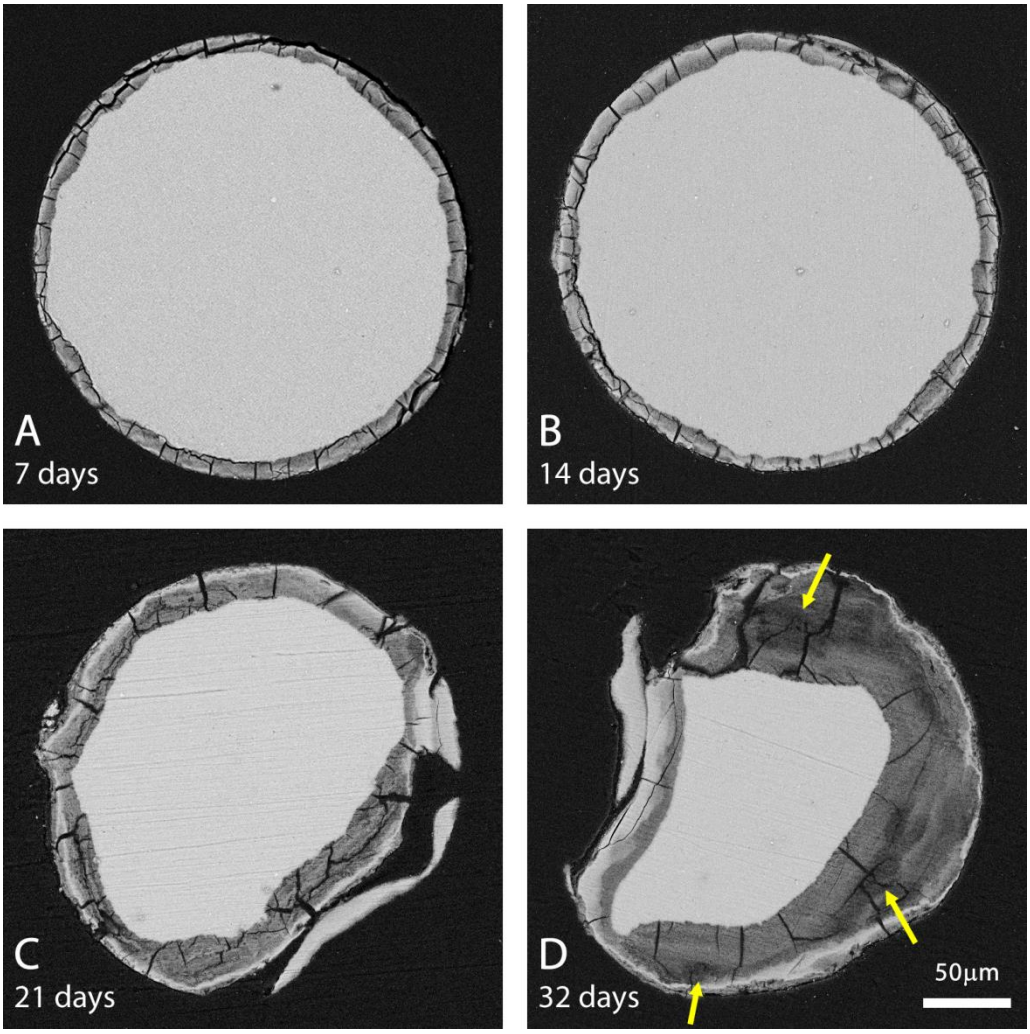

Figure 3.6 – Representative backscattered electron images (300× nominal magnification) of magnesium wire cross sections at 7 (panel A), 14 (B), 21 (C), and 32 days (D) *in vivo*. The 50 µm scale in (D) applies to all images. Yellow arrows in (D) indicate shadowed areas that correspond to epoxy infiltration.

Elemental mapping of the same series of cross sections revealed the distribution of the key elements magnesium, oxygen, phosphorus, and calcium in the sections of interest. These maps and corresponding regional BEIs are presented in Figure 3.7. The elemental signatures reconfirm the two distinct corrosion products that were apparent in the series of BEIs (Figure 3.6). At 7 days, a calcium- and phosphorus-containing uniform surface

layer is observed in addition to an inner layer comprising magnesium—albeit much less than the unadulterated metal—and oxygen. Phosphorus was incorporated to a limited degree in portions of the inner layer, but was more highly concentrated in the outer (surface) layer. Calcium was highly concentrated in the surface layer, but was not incorporated into the inner layer to the extent phosphorus was. Some variations in thickness of the outer layer are seen at 7 days, consistent with the corresponding BEI.

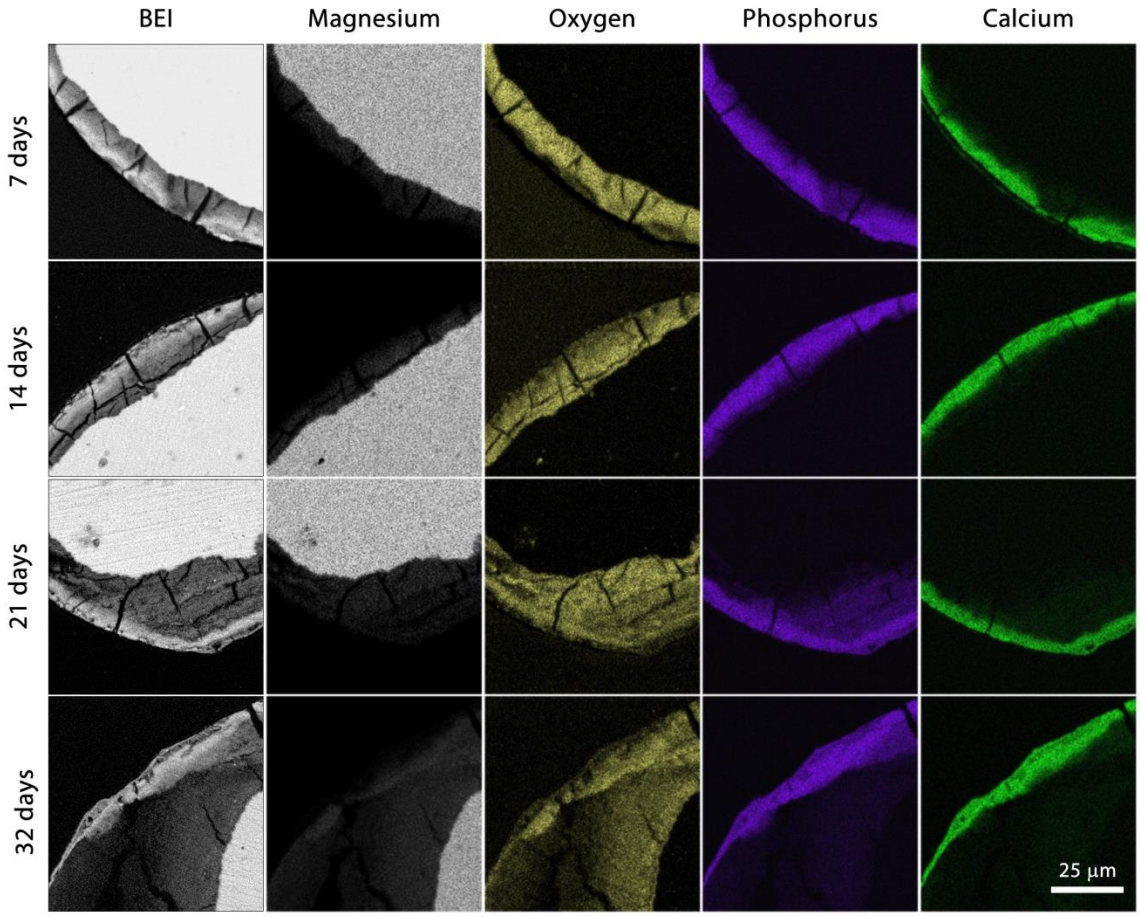

Figure 3.7 – Backscatter electron images and elemental (EDS) maps for 7, 14, 21, and 32 day time points at 1500× nominal magnification. Magnesium (gray), oxygen (yellow), phosphorus (purple), and calcium (green) maps are presented.

At 14 days, the EDS maps were qualitatively similar. The corrosion layer had thickened a bit and the products had become somewhat more segregated, with a more distinct Mg- and O-bearing layer near the wire center. Phosphorus, again, was present at a greater depth than the calcium, which was confined to a uniform layer at the surface. Magnesium seems to have been displaced almost completely by calcium near the surface, manifesting as a low X-ray signal from the outer region.

Later time points had elemental distributions that deviated from the compact, two-region structure at the 7 and 14 day time points. The primary difference was a loss of integrity of the inner corrosion layer, evidenced by regional loss of signal from magnesium and oxygen and their replacement with carbon and chlorine signals characteristic of epoxy (carbon and chlorine not shown in Figure 3.7). Phosphorus incorporation into the inner corrosion layer was more pronounced in some locations, and was accompanied by calcium more so than at earlier times. Trace element maps of sodium, chlorine, and carbon were also produced, but were of limited utility. Heavily brightness- and contrast-enhanced examples of these maps from the 14 day time point are included in Figure 3.8. The carbon [Figure 3.8(A)] signal was produced primarily from the surrounding epoxy or from locations where the epoxy had penetrated into the sample.

3.1.5 Discussion

3.1.5.1 Implications of surface imaging

Cells attached to the magnesium surface are thought to be responsible for the unexpected coloration observed in the 5 day sample (Figure 3.1). Later samples did not show

evidence of biological materials on the surface. The lack of apparent vascular cell attachment or matrix synthesis at the Mg-artery interface observed during surface analysis is a testament to magnesium's excellent biocompatibility. It also suggests that magnesium *per se* may not stimulate intimal hyperplasia of smooth muscle cells, which is the hallmark mode of failure for stented arteries [29]. However, injury from angioplasty and the placement of a magnesium stent has been observed experimentally [30] and clinically [9] to contribute to neointimal growth, spurring the more recent use of drug-eluting coatings on magnesium stents [10]. Further *in vivo* study of neointimal formation on magnesium is needed to parse the individual contributions of acute injury, chronic mechanical irritation, and material response in bioabsorbable implant systems.

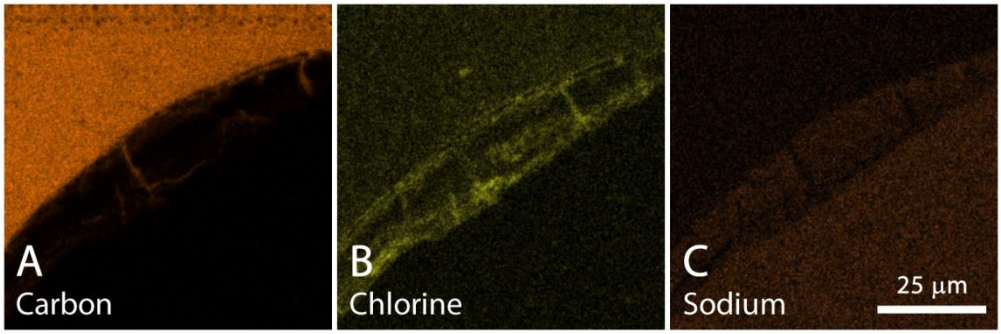

Figure 3.8 – Example of the trace element maps for carbon (A), chlorine (B), and sodium (C) from the 14 day magnesium wire section.

3.1.5.2 Interpretation of FT-IR spectra

FT-IR evaluation revealed a second-to-form, or "late stage," product (Figure 3.3 and Figure 3.5). The most probable structure of the second-to-form product, based on the characteristics of FT-IR data obtained by Knaack *et al*. for an explanted sample of

absorbable bone substitute material [31], is a carbonate-substituted hydroxyapatite (HAp) of physiologically preferred composition and structure. The broad IR absorption bands in Figure 3.3 are unlike the well-defined bands typical of synthetic, crystalline HAp or calcium phosphates [32]. Instead, the broad bands indicate a relatively large amount of vibrational freedom, and are representative of amorphous HAp variants like those prepared by Holt *et al.* [25].

Further information about the second-to-form product may be elucidated by comparing the substitution peak intensities (A:B ratio = I_{880}/I_{873}) reported in Figure 3.4 [23, 33]. The data suggest that the replacement of OH^- by carbonate remains consistent, but alternative substitution for PO_4^{3-} becomes increasingly unfavorable up to 29 days *in vivo*. An A:B ratio greater than unity signifies predominantly A-type substitutions; a quantity less than unity indicates that B-type substitutions dominate; and a ratio close to unity indicates that A- and B-type substitutions are equally prevalent, a so-called "AB-type" HAp. The peak ratios for the explanted magnesium after 12 days *in vivo* is ≈ 2.2, pointing to a primarily A-type HAp. By 29 days, the ratio climbs to a value of ≈ 9.9, showing that the surface has a tendency towards A-type substitution at times close to fragmentation. Therefore, it is determined that the second-to-form surface product is "A-type HAp."

The first-to-form product's spectrum lacks any sharp peaks, and so an amorphous structure is again suspected. The position and relative intensity of the dominant absorption bands are analogous to those observed by Suchanek *et al.* [34] and Cao and Harris [24] for heavily magnesium-substituted amorphous HAp. It is known that the

apatitic structure is not favored when magnesium is substituted in high concentrations, often forcing the HAp to assume an amorphous or poorly crystalline structure [35]. To partially relieve the size mismatch between Ca^{2+} and Mg^{2+} in the HAp lattice, carbonate groups are often incorporated [33]. Thus, it is then reasonable to identify the first-to-form product as a carbonate-substituted, amorphous, Mg-bearing species of hydroxyapatite, here designated "Mg/Ca HAp."

Identification of a dual-phase HAp surface layer is perhaps counterintuitive, as one might instead anticipate a homogenous calcium phosphate or a continuous compositional gradient of HAp at the surface. The duplex structure may be due to the gradual ionic exchange of magnesium for calcium from the arterial environment. Yasukawa *et al.* [36] studied the ion exchange in synthetic Mg/Ca HAp, reporting on the rapid replacement of incorporated Mg^{2+} with Ca^{2+} in several Ca-bearing exchange electrolytes. A tentative mechanism for this substitution was proposed as (i) dissolution of the Mg/Ca HAp and (ii) re-deposition of a more structurally favorable HAp. The re-deposited HAp contained about 60% of the nominal concentration of Mg^{2+} and remained amorphous. Yasukawa's ion exchange mechanism appears to explain the emergence of the duplex Mg/Ca HAp and A-type HAp surface layer. This mechanism was observed to be active in neutral-to-acidic exchange electrolytes. An increased pH at the surface, typical for Mg biomaterials [37], may account for the slow onset and progression of this transformation *in vivo*.

3.1.5.3 Interpretation of cross sectional analyses

From the backscattered electron images, the state of the explanted wire at 7 days was nearly identical to subsequent explants through ~14 days. This is reflected in BEIs at 7 days [Figure 3.6(A)] and 14 days [Figure 3.6(B)]. The remaining magnesium material at this stage was approximately circular, and the degradation fit the general definition of uniform corrosion [38]. At times through 14 days, the HAp layer was well integrated with the inner product, and a clear delineation was not evident in backscatter (Figure 3.6) or from EDS mapping (Figure 3.7). Beginning at ~17 days, however, a sharp boundary between the low- and high atomic number products was noted. The enhanced boundary lends credence to the hypothesized mode of ion exchange via gradual dissolution of the Mg/Ca HAp and re-precipitation of A-type HAp from the surroundings.

The inner corrosion product seemed to lose integrity at 29 and 32 days, with the appearance of diffuse "shadows" in backscatter contrast attributed to penetration by epoxy indicated by yellow arrows in Figure 3.6(D). These disintegrated regions seemed to be accompanied by overlaying HAp that was substantially thinned and/or locally absent. Examples of these regions were identified in each time point after 21 days, and examples from three separate samples are presented in Figure 3.9.

This phenomenon indicates that a loss of integrity of the outer layer by bioabsorption, spalling, etc. enables the arterial environment to penetrate and attack the inner product, accelerating dissolution of the implant. This observation is in agreement with the reported protective action of calcium phosphate formed on the surface of magnesium *in*

vitro [39]. If such a protective layer was disrupted, its corrosion-inhibiting properties would be bypassed and localized corrosion would ensue. Improving the durability of the surface HAp layer may therefore provide a promising route to enhance long-term corrosion performance of magnesium in the arterial environment.

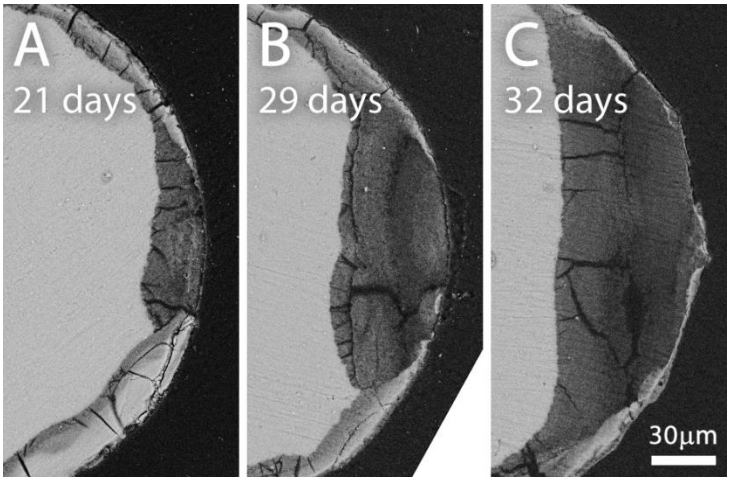

Figure 3.9 – Backscattered electron images of regions of sections that were attacked locally at points where a thin and/or disrupted HAp layer was present. Such points were visible in several instances at 21 (A), 29 (B), and 32 days (C). The 30μm scale bar applies to all panels.

The outer product does appear to have a weak carbon signature, which may be a combination of incorporated carbon (from carbonate, determined by μFT-IR) and epoxy that occupied surface defects. A carbon signal was not generated from the inner corrosion layer, suggesting that this layer did not contain significant quantities of carbonate. Chlorine [Figure 3.8(B)] is a constituent of the epoxy, and so is again present surrounding the wire section in low concentrations. A Cl signal was observed at some edge sites after the map contrast was enhanced. The mode of Cl incorporation in the corrosion layer is not evident from these data (e.g. $MgCl_2$ particulate or adsorbed

interfacial chloride ions), but it may be similar to the *in vitro* incorporation of chloride ions observed by Willumeit *et al.* [40]. Sufficed to say, Cl is a trace constituent to which the bulk analysis methods used here are not sensitive, and would require different methods of evaluation to describe completely. Sodium [Figure 3.8(C)] does not appear to be present in any detectable quantity, and the weak signal presented in this report originates from the tails of the magnesium K_α peak. Thus, sodium does not appear to be retained during the formation of physiological corrosion products on magnesium.

A compositional study of the inner, Mg-O corrosion layer was attempted using single-point energy dispersive spectroscopy. However, the small width of this corrosion layer at early times resulted in electron interaction with the outer corrosion layer and/or the magnesium core. Likewise, later infiltration of epoxy into the corrosion layer prevented accurate energy dispersive spectroscopy results from being obtained. Future work may utilize larger-geometry specimens or those that facilitate the growth of a thick calcium-phosphate overlayer to grow a suitably large, stable oxygen-containing layer. Careful X-ray microanalysis on such a product may reveal if the Mg:O ratio is closer to MgO (1:1), $Mg(OH)_2$ (1:2), $MgCO_3$ (1:3), or if it exhibits variations throughout the layer. The incorporation of carbonate is dubious because of the lack of a carbon signal from the inner corrosion layer (Figure 3.8). Alternatively, crystallographic methods such as X-ray diffraction in a Debye-Scherrer configuration or preparation of thin foils followed by TEM examination and electron diffraction may allow for the identification of a specific Mg-O(-C) phase.

3.1.5.4 Proposed long-term corrosion mechanism

Corrosion mechanisms for bioabsorbable materials have generally been formulated based on *in vitro* experiences [40-42], and typically deal only with early-stage corrosion behavior and surface modification. Attention has not been paid to mass transport phenomena in the quasi-steady state, nor has the issue of terminal breakdown of magnesium biomaterials been sufficiently discussed. Using the data presented in this contribution, aspects of the corrosion mechanism in the quasi-steady state and terminal stages may be elucidated. Phenomena of interest are depicted in Figure 3.10, and include mass transport in the corrosion layer and the ion exchange mechanism leading to HAp modification [Figure 3.10(A)], and destabilization of the inner corrosion layer in the terminal stages of corrosion [Figure 3.10(B)]. Vertical scales at the surface in Figure 3.10 are exaggerated for clarity.

In the established corrosion layer at 7–21 days, thickening of the inner corrosion layer is observed to progress slowly relative to that which occurred during the first week of residence. This time period comprises a quasi-steady state. The reason for the decrease in corrosion rate has much to do with the initial development of an apatitic overlayer [39] that provides protection for the inner layers. From observations made in this study—particularly the analysis of backscattered electron images (Figure 3.6)—it can be stated with confidence that voids are not present in the metallic magnesium core during the corrosion process. A lack of voids suggests that mass transport does not occur in great

amounts from the magnesium to the outer surface; such a phenomenon would be expected to produce vacancies that would coalesce to form microvoids.

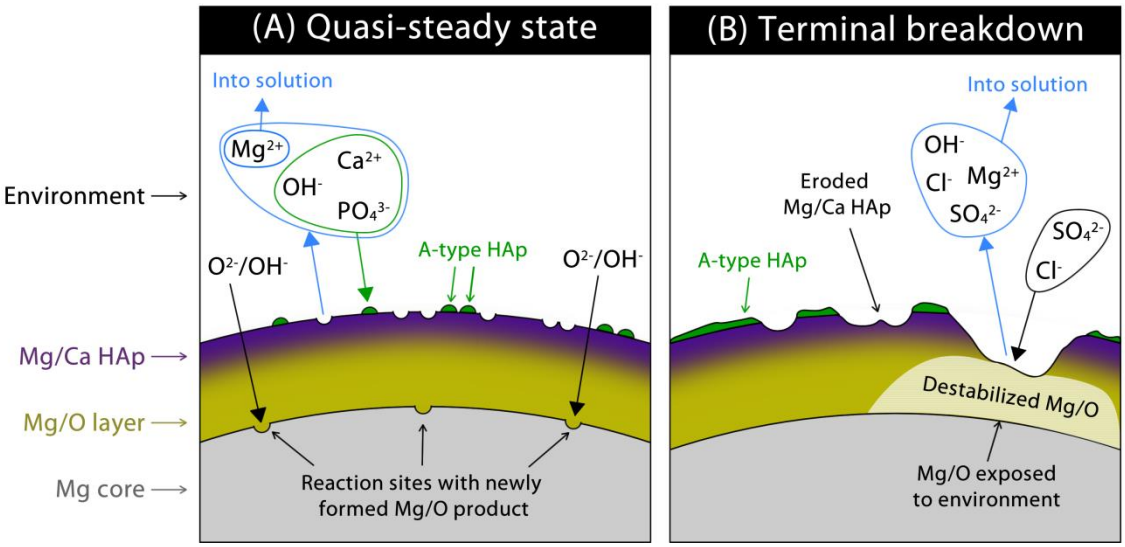

Figure 3.10 – Schematic showing transformations supposed to be taking place in the quasi-steady state (A), including apatitic ion exchange and reactions at the Mg-Mg/O interface, and during the terminal breakdown stage (B), dominated by dissolution of the Mg/O layer upon exposure to the arterial environment.

Mass transport from the outer surface towards the magnesium core is instead dominant. The ingress of oxygen/hydroxyl ions therefore controls the consumption of metallic magnesium in the quasi-steady state. As stated previously, the composition of the inner layer is unknown, and, therefore, it is not clear if mass transport is more likely to involve O^{2-} or OH^-. Incorporation of phosphorus in the corrosion layer may play a role in enhancing ionic transport by encouraging the development of oxygen/hydroxide vacancies. However, a specific point-defect relationship cannot be determined at this time because the mode of phosphorus incorporation (i.e. as phosphate, phosphate dibasic, phosphate monobasic, etc.) is undetermined.

Ion exchange between the Mg/Ca HAp and the surrounding environment is suspected to occur concurrently with the mass transport phenomenon. The schematic representation of the ion exchange process [Figure 3.10(A)] illustrates the dissolution of the Mg/Ca HAp and precipitation of the A-type HAp on the surface. A detailed discussion of this mechanism was previously presented and is therefore not reiterated here. The precipitated A-type HAp forms a distinct surface layer, as shown in Figure 3.7 and illustrated in Figure 3.10(B). Eventually, the consumption of Mg/Ca HAp is expected to thin the apatitic overlayer sufficiently to expose the inner corrosion layer to the arterial environment. Works on conventional magnesium corrosion reference the destabilization of $Mg(OH)_2$/MgO partially protective films by chloride [43-45] in a localized fashion [46]. The sulfate anion is also considered to be aggressive in this context [47]. The likely result of localized exposure of the inner corrosion layer to the biological environment is thus an underlying region of destabilized Mg/O product. Such a region is observed in Figure 3.9 and illustrated in Figure 3.10(B). An increase in the corrosion rate near the onset of "terminal breakdown" has also manifested itself in quantitative corrosion measurements (refer to Section 2.2).

3.1.6 Conclusions

Commercially pure magnesium wires were corroded in the arterial walls of Sprague-Dawley rats for up to 32 days, removed, and characterized. At the earliest (five day) time point, erythrocytes were adhered to explant surface. Surface analysis via μFT-IR revealed a first-to-form product consistent with a heavily magnesium-substituted

hydroxyapatite. Later specimen surfaces were consistent with a hydroxyapatite with A-type carbonate substitution. The two-phase hydroxyapatite layer was hypothesized to form by an ion exchange mechanism. Analysis of the bulk product via x-ray mapping revealed a Ca- and P-containing outer layer consistent with hydroxyapatite, in addition to an Mg- and O-bearing inner layer. Phosphorus was observed to penetrate the inner layer of corrosion, while there was a small amount of carbon observed in the same layer. A loss of integrity of the apatitic outer coating appeared to result in local growth of the inner Mg- and O-containing corrosion layer. Mechanisms related to ion exchange, mass transport in the quasi-steady state (~7 to 21 days), and the mode of terminal breakdown in the magnesium implants after ~21 days are suggested based on experimental observations.

3.1.7 Acknowledgements

PKB was supported by fellowship funds from the DeVlieg Foundation and subsequently by the American Heart Association during this work. Owen Mills and Felicia Nip of the Applied Chemical and Morphological Analysis Laboratory are acknowledged for their help in preparing samples for electron microscopy. Boyi Hao and Prof. Yoke Khin Yap from the Physics Department at Michigan Technological University are gratefully acknowledged for use of and assistance with the μFT-IR microscope. Thanks also to Adam Drelich for his assistance preparing wire cross sections and to Emily Shearier with her assistance in editing the manuscript.

3.1.8 References

[1] Mani G, Feldman MD, Patel D, Agrawal CM. Coronary stents: a materials perspective. Biomaterials 2007;28:1689-710.

[2] Kirkland NT, Birbilis N, Staiger MP. Assessing the corrosion of biodegradable magnesium implants: a critical review of current methodologies and their limitations. Acta Biomater 2012;8:925-36.

[3] Heublein B, Rohde R, Kaese V, Niemeyer M, Hartung W, Haverich A. Biocorrosion of magnesium alloys: a new principle in cardiovascular implant technology? Heart 2003;89:651-6.

[4] Waksman R, Pakala R, Kuchulakanti PK, Baffour R, Hellinga D, Seabron R, et al. Safety and efficacy of bioabsorbable magnesium alloy stents in porcine coronary arteries. Catheter Cardiovasc Interv 2006;68:607-17; discussion 18-9.

[5] Slottow TL, Pakala R, Okabe T, Hellinga D, Lovec RJ, Tio FO, et al. Optical coherence tomography and intravascular ultrasound imaging of bioabsorbable magnesium stent degradation in porcine coronary arteries. Cardiovasc Revasc Med 2008;9:248-54.

[6] Wittchow E, Adden N, Riedmuller J, Savard C, Waksman R, Braune M. Bioresorbable drug-eluting magnesium-alloy scaffold: design and feasibility in a porcine coronary model. EuroIntervention 2013;8:1441-50.

[7] Zartner P, Cesnjevar R, Singer H, Weyand M. First successful implantation of a biodegradable metal stent into the left pulmonary artery of a preterm baby. Catheter Cardiovasc Interv 2005;66:590-4.

[8] Erbel R, Di Mario C, Bartunek J, Bonnier J, de Bruyne B, Eberli FR, et al. Temporary scaffolding of coronary arteries with bioabsorbable magnesium stents: a prospective, non-randomised multicentre trial. Lancet 2007;369:1869-75.

[9] Waksman R, Erbel R, Di Mario C, Bartunek J, de Bruyne B, Eberli FR, et al. Early- and long-term intravascular ultrasound and angiographic findings after

bioabsorbable magnesium stent implantation in human coronary arteries. JACC Cardiovasc Interv 2009;2:312-20.

[10] Haude M, Erbel R, Erne P, Verheye S, Degen H, Bose D, et al. Safety and performance of the drug-eluting absorbable metal scaff old (DREAMS) in patients with de-novo coronary lesions: 12 month results of the prospective, multicentre, first-in-man BIOSOLVE-I trial. Lancet 2013;381:836-44.

[11] Peng Q, Li K, Han Z, Wang E, Xu Z, Liu R, et al. Degradable magnesium-based implant materials with anti-inflammatory activity. J Biomed Mater Res A 2013;101:1898-906.

[12] Xin Y, Hu T, Chu PK. *In vitro* studies of biomedical magnesium alloys in a simulated physiological environment: a review. Acta Biomater 2011;7:1452-9.

[13] Pierson D, Edick J, Tauscher A, Pokorney E, Bowen PK, Gelbaugh J, et al. A simplified *in vivo* approach for evaluating the bioabsorbable behavior of candidate stent materials. J Biomed Mater Res B 2012;100B:58-67.

[14] Bowen PK, Drelich J, Goldman J. Zinc exhibits ideal physiological corrosion behavior for bioabsorbable stents. Adv Mater 2013;25:2577-82.

[15] Bowen PK, Drelich J, Buxbaum RE, Rajachar RM, Goldman J. New approaches in evaluating metallic candidates for bioabsorbable stents. Emer Mater Res 2012;1:237-55.

[16] Bowen PK, Gelbaugh JA, Mercier PJ, Goldman J, Drelich J. Tensile testing as a novel method for quantitatively evaluating bioabsorbable material degradation. J Biomed Mater Res B 2012;100B:2101-13.

[17] Bowen PK, Drelich J, Goldman J. A new *in vitro-in vivo* correlation for bioabsorbable magnesium stents from mechanical behavior. Mater Sci Eng C 2013;33:5064-70.

[18] Hanawalt JD, Nelson CE, Peloubet JA. Corrosion studies of magnesium and its alloys. Trans AIME 1942;147:273-99.

[19] Liu M, Uggowitzer PJ, Nagasekhar A, Schmutz P, Easton M, Song G-L, et al. Calculated phase diagrams and the corrosion of die-cast Mg–Al alloys. Corros Sci 2009;51:602-19.

[20] Kristukat C. peak-o-mat. SourceForge; 2007.

[21] Gulliver G. Observations on the sizes and shapes of the red corpuscles of the blood of vertebrates, with drawings of them to a uniform scale, and extended and revised tables of measurements. P Zool Soc Lond 1875;1875:474-95.

[22] Stuart B. Infrared Spectroscopy: Fundamentals and Applications. Hoboken, NJ: Wiley; 2004.

[23] Gibson IR, Bonfield W. Preparation and characterization of magnesium/carbonate co-substituted hydroxyapatites. J Mater Sci Mater M 2002;13:685-93.

[24] Cao X, Harris W. Carbonate and magnesium interactive effect on calcium phosphate precipitation. Envir Sci Technol 2008;42:436-42.

[25] Holt C, van Kemenade MJJM, Harries JE, Nelson LS, Bailey RT, Hukins DWL, et al. Preparation of amorphous calcium-magnesium phosphates at pH 7 and characterization by x-ray absorption and fourier transform infrared spectroscopy. J Cryst Growth 1988;92:239-52.

[26] Frost RL, Martens W, Williams PA, Kloprogge JT. Raman and infrared spectroscopic study of the vivianite-group phosphates vivianite, baricite and bobierrite. Mineral Mag 2002;66:1063-73.

[27] Meejoo S, Maneeprakorn W, Winotai P. Phase and thermal stability of nanocrystalline hydroxyapatite prepared via microwave heating. Thermochim Acta 2006;447:115-20.

[28] Frost RL, Kloprogge JT. Infrared emission spectroscopic study of brucite. Spectrochim Acta A 1999;55:2195-205.

[29] Kastrati A, Schömig A, Elezi S, Schühlen H, Dirschinger J, Hadamitzky M, et al. Predictive factors of restenosis after coronary stent placement. J Am Coll Cardiol 1997;30:1428-36.

[30] Maeng M, Jensen LO, Falk E, Andersen HR, Thuesen L. Negative vascular remodelling after implantation of bioabsorbable magnesium alloy stents in porcine coronary arteries: a randomised comparison with bare-metal and sirolimus-eluting stents. Heart 2009;95:241-6.

[31] Knaack D, Goad MEP, Aiolova M, Rey C, Tofighi A, Chakravarthy P, et al. Resorbable calcium phosphate bone substitute. J Biomed Mater Res 1999;43:399-409.

[32] Berzina-Cimdina L, Borodajenko N. Research of calcium phosphates using Fourier transform infrared spectroscopy. In: Theophanides T, editor. Infrared Spectroscopy—materials science, engineering and technology. Rijeka: Intech; 2012.

[33] Gibson IR, Bonfield W. Novel synthesis and characterization of an AB-type carbonate-substituted hydroxyapatite. J Biomed Mater Res 2002;59:697-708.

[34] Suchanek WL, Byrappa K, Shuk P, Riman RE, Janas VF, TenHuisen KS. Preparation of magnesium-substituted hydroxyapatite powders by the mechanochemical-hydrothermal method. Biomaterials 2004;25:4647-57.

[35] Yasukawa A, Ouchi S, Kandori K, Ishikawa T. Preparation and characterization of magnesium-calcium hydroxyapatites. J Mater Chem 1996;6:1401-5.

[36] Yasukawa A, Yokoyama T, Kandori K, Ishikawa T. Ion-exchange property and mechanism of magnesium–calcium hydroxyapatite solid solutions. Colloid Surface A 2004;238:133-9.

[37] Song G. Control of biodegradation of biocompatable magnesium alloys. Corros Sci 2007;49:1696-701.

[38] Jones DA. Principles and prevention of corrosion. Englewood Cliffs, NJ: Prentice Hall; 1996.

[39] Wu G, Zhao Y, Zhang X, Ibrahim JM, Chu PK. Self-protection against corrosion of aged magnesium alloy in simulated physiological environment. Corros Sci 2013;68:279-85.

[40] Willumeit R, Fischer J, Feyerabend F, Hort N, Bismayer U, Heidrich S, et al. Chemical surface alteration of biodegradable magnesium exposed to corrosion media. Acta Biomater 2011;7:2704-15.

[41] Kalb H, Rzany A, Hensel B. Impact of microgalvanic corrosion on the degradation morphology of WE43 and pure magnesium under exposure to simulated body fluid. Corros Sci 2012;57:122-30.

[42] Kim W-C, Han K-H, Kim J-G, Yang S-J, Seok H-K, Han H-S, et al. Effect of surface area on corrosion properties of magnesium for biomaterials. Met Mater Int 2013;19:1131-7.

[43] Casey EJ, Bergeron RE. On the mechanism of the dissolution of magnesium in acidic salt solutions: I. Physical control by surface films. Can J Chem 1953;31:849-67.

[44] Robinson JL, King PF. Electrochemical behavior of the magnesium anode. J Electrochem Soc 1961;108:36-41.

[45] Song G, Atrens A, St. John D, Nairn J, Li Y. The electrochemical corrosion of pure magnesium in 1N NaCl. Corros Sci 1997;39:855-75.

[46] King PF. The role of the anion in the anodic dissolution of magnesium. J Electrochem Soc 1966;113:536-9.

[47] Xin Y, Huo K, Tao H, Tang G, Chu PK. Influence of aggressive ions on the degradation behavior of biomedical magnesium alloy in physiological environment. Acta Biomater 2008;4:2008-15.

3.2 FIB-TEM study of magnesium corrosion products after 14 days in the murine artery[6]

3.2.1 Abstract

After a decade of intensive research on magnesium biodegradation, the composition and structure of corrosion products formed during *in vivo* corrosion is still not precisely known. Focused ion beam (FIB) micromilling and transmission electron microscopy (TEM) were used to elucidate the nanostructure and crystallography of the corrosion products that form at or near the interface between the corrosion products and metallic magnesium. This study built upon previously reported scanning electron microscopy, infrared spectroscopy, and energy dispersive X-ray spectroscopy data. These prior results revealed a duplex corrosion layer comprising a calcium- and phosphorus-containing outer product (near the tissue interface) and a magnesium- and oxygen-containing inner product (near the metallic interface). A specimen that had resided in the murine arterial wall for 14 days was selected for FIB-TEM analysis. Highly oriented, nanocrystalline magnesium oxide was identified near the metallic magnesium, apparently without the co-occurrence of magnesium hydroxide or carbonates. The calcium- and

[6] The material in Section 3.2 was previously published in *ACS Biomaterials Science and Engineering* and is reproduced here with permission.

P. K. Bowen, C. T. McNamara, O. P. Mills, J. W. Drelich, and J. Goldman. "FIB-TEM study of magnesium corrosion products after 14 days in the murine artery." *ACS Biomater. Sci. Eng.* 1(10) 919-926 (2015), doi: 10.1021/acsbiomaterials.5b00044.

References in Section 3.2 follow the *ACS Biomaterials Science and Engineering* author guidelines.

phosphorous-containing surface layer was also examined, and was shown to be nearly amorphous.

3.2.2 Introduction

As a consequence of latent side effects associated with permanent endovascular stents, bioabsorbable metallic alternatives have been pursued over the past decade [1-4]. Metallic stents are considered to be superior to polymeric devices in terms of mechanical performance (i.e. elastic range [5]) and ease of translation to a clinical environment. The recent ABSORB II trial [6]—which evaluated the performance of a polymeric scaffold relative to a conventional, metallic, drug-eluting device—found poor post-intervention luminal gains when polymeric devices were employed. This was due, in part, to the reluctance of participating physicians to fully expand the brittle polymeric material [7]. Furthermore, a 10-year follow-up with patients that had received an Igaki-Tamai poly(L-lactic) acid (PLLA) coronary stent found poor tissue remodeling through histological analysis [8]. The area previously occupied by PLLA appeared to be filled with proteoglycan, a component of extracellular matrix, but was acellular.

Iron- [9-12], zinc- [13], and magnesium (Mg)-based [14-16] materials have been considered for this application due to these metals' biological role as essential trace elements . Previous work with pure iron identified seemingly biostable iron oxide in the murine artery after a residence of nine months [17], which indicated that this material was not fully degradable. Metallic zinc is a relatively new, but promising [13], candidate. Of the three metallic

material families, the most thoroughly investigated is Mg, which has been explored extensively in porcine arteries [16, 18-21], as well as in a clinical setting [15, 22-24]. Despite the large body of work addressing bioabsorbable Mg alloy development [25], degradable coating technologies [26], and *in vitro* corrosion testing [27], there has been a relative lack of attention paid to the *in vivo* corrosion kinetics and the identity of the generated products.

Characterization of wires corroded in the arteries of rats for up to 32 days has previously been carried out using optical microscopy, scanning electron microscopy, microscale Fourier transform infrared spectroscopy, and energy dispersive X-ray spectroscopy (EDS) mapping [28]. It was found in the course of these previous experiments that the corrosion of Mg appeared to occur in three stages [28, 29]:

1. rapid initial degradation and the formation of a semi-protective surface film;
2. a decrease in the corrosion rate corresponding to stabilization of the surface film, which was termed "quasi-steady state" degradation; and
3. thinning or disruption of the outermost corrosion product resulting in rapid, local degradation that promoted sample fragmentation, and was therefore called "terminal breakdown."

Corrosion products that formed on pure Mg implants were demonstrated to comprise two layers. The "outer corrosion product," which resides at the implant-arterial tissue interface, was distinguished by the presence of Ca and P. Two different phases within the Ca/P region were identified previously [28]: a heavily Mg-substituted hydroxyapatite (Mg/Ca HAp) that was present at early experimental time points, as well as a

hydroxyapatite with A-type carbonate substitution. The latter product was hypothesized to form on the surface of the former by an ion exchange mechanism [30]. A compositionally distinct product comprising Mg, O, and possibly C was identified between the Mg metal and outer corrosion product. This Mg-O(-C) phase comprises the "inner corrosion product," and has been suggested to include MgO, $Mg(OH)_2$, $MgCO_3$, hydrated carbonate variants, or a mixture thereof [21]. The inner corrosion product was not accessible to infrared spectroscopy, nor to single-point EDS due to its location within the corrosion layer and relatively small size. EDS mapping did not show significant amounts of carbon in the inner corrosion product, so it was concluded that it was unlikely to include carbonate anions in significant quantities [28].

The present study was designed to determine the composition and structure of the inner corrosion product. The 14-day time point was previously shown to be a critical, "transitional" time for this series of pure Mg wires [28, 29], at which the material was likely to exhibit characteristics of both quasi-steady state corrosion and terminal breakdown behavior. For this reason, the 14-day sample was selected for in-depth examination using focused ion beam (FIB) micro-milling and transmission electron microscopy (TEM). With these tools, both the nanostructure of the corrosion interface and the crystallographic structure of its constituent products were available for analysis.

3.2.3 Methods & Materials

3.2.3.1 *In vivo* corrosion protocol

Mg wires with 99.9% purity and 250 ± 25 μm diameter were acquired from Goodfellow (Coraopolis, Pennsylvania) and used in as-received condition. Per specification, typical impurities included < 1 ppm Ag, 10 ppm Ca, 5 ppm Cu, 100 ppm Fe, 300 ppm Mn, < 1 ppm Na, and 100 ppm Si. Prior to implantation, the Mg wires were briefly sanitized in 70% ethyl alcohol and irradiated with ultraviolet light. A surgical protocol previously used to implant samples in the arterial wall was utilized [17]. A 10 mm segment of wire—of the same microstructure and composition as used in previous reports [28, 29]—was implanted in the abdominal aorta of an adult Sprague-Dawley rat. During surgery, the Mg wire was used to puncture the adventitial layer, and was then led into or near the medial layer without damaging the endothelium. At the specified time point, the rat was euthanized and the Mg wire retrieved from the artery. During the removal procedure, it was confirmed by visual examination that the implant had not shifted to a position outside the arterial media or adventitia. After retrieval, the wire was stored in the low humidity environment of a desiccator.

The animal experiments were approved by the Michigan Technological University Institutional Animal Care and Use Committee (IACUC) and were conducted in accordance with the Panel on Euthanasia of the American Veterinary Medical Association.

3.2.3.2 Sample preparation

The wire was placed in plastic sample clips and mounted in two-part epoxy inside a silicone tube (~8 mm inner diameter). After curing, the mounted wires were removed from the silicone tubes. The ends of the corroded wires—deformed by cutting—were avoided for this analysis; sectioning began at a minimum distance of 0.5 mm from the end of the wire. Cross sections were prepared by grinding the exposed wire in a metallographic fashion with 600- and 800-grit SiC paper and alcohol-based lubricant and polishing with a 1 μm Al_2O_3 slurry on microfiber. The polished end was then cut with a fresh microtome blade to create a section of 0.8–1 mm thickness. The newly exposed surface was ground, polished, and cut as before to produce multiple sections. Embedded sections of wire were carbon-coated to improve conductivity and then imaged with a JEOL JSM-6400 scanning electron microscope (SEM) (Peabody, Massachusetts), using its backscattered electron detector to provide phase contrast. Detailed analyses of these sections have been carried out previously, including elemental mapping with EDS [28] and corrosion rate calculations [29].

A section from the 14-day transitional time point that had an intact corrosion layer with minimal cracking and possessed a typical amount and type of corrosion for the 14-day time point was selected for FIB micro-milling operations. Consistency with all other sections—10 from the 14-day time point and ~100 other sections overall—was confirmed by compiling and comparing all the respective backscattered electron images. A 30 kV Hitachi FB-2000A FIB (Hitachi High Technologies America; Pleasanton, California),

which uses high-energy gallium ions to perform milling operations, was used. The epoxy-mounted, carbon-coated section was held using a TEM-type goniometer. A protective tungsten mask was deposited on the region of interest. A section containing parts of the Mg metal, inner Mg-O(-C) corrosion layer, and outer Ca/P corrosion product was trimmed to a rectangular prism measuring roughly $15 \times 15 \times 2$ μm, which was subsequently extracted using the tungsten probe lift-out technique [31-33]. The rectangular prism of material was affixed to a TEM half grid, again using tungsten deposition. The specimen was thinned edge-on with progressively finer beams to achieve electron transparency. The final thickness of the foil was approximately 200 nm. This value was governed by residual stresses in the sample, which threatened to warp the sample severely if it were thinned further.

3.2.3.3 Electron microscopy

The final foil was examined briefly with a Hitachi S-4700 field emission scanning electron microscope (FE-SEM), operated at 5 kV accelerating voltage and 7.5 μA emission current, to identify the metal-product interface and confirm that both products were visible within the milled foil.

TEM examination was performed using a JEOL JEM-2010 high resolution TEM equipped with a high-brightness LaB_6 source and an Orius SC200 high-speed digital camera (Gatan, Inc.; Pleasanton, California). The microscope was operated with an accelerating voltage of 200 kV with a small condenser aperture to establish a nearly parallel beam. Bright field images, selected area electron diffraction (SAED) patterns,

and dark field images were acquired. SAED patterns were captured at camera lengths of 120–150 mm in order to scale the pattern to cover the charge-coupled device (CCD) sensor in the Orius camera. A beam blocker was also used to shield the CCD from the transmitted beam.

Neighboring bright field images were stitched under constant scale and planar translation conditions using the Microsoft Image Composite Editor. Measurement of SAED spot spacing, SAED angular relationships, and bright and dark field feature sizes were done with imageJ [34]. Peak indexing of metallic Mg utilized a custom MATLAB script capable of searching reciprocal space for families of indices that matched length ratio and angular relationship values within a specified tolerance.

Chemical composition of the foil was examined by means of SEM- EDS. A FEI Philips XL 40 tungsten-source Environmental SEM (Hillsboro, Oregon) equipped with an Oxford Instruments (Oxfordshire, United Kingdom) Inca EDS system based on a 30 mm Si(Li) detector. The SEM was operated at 15 kV, and a line scan was captured diagonally across the sample with a total dwell time of 40 ms per pixel at 30% nominal dead time. The SEM-EDS analysis was carried out after TEM evaluation; it did not affect the nanoscale structures observed in the main portion of this study.

3.2.4 Results

3.2.4.1 FESEM and SEM-EDS evaluation

The foil images acquired via FE-SEM examination are shown in Figure 3.11 in wide view (A) and a close-up of the metal-product interface (B). The outermost edge of the foil is observed to have buckled or folded from residual stresses. A large area in the center of the foil was suitable for TEM analysis. Within this area appropriate for TEM analysis, the Mg metal and products of biocorrosion are both present. The metal-product interface is observed to be rather jagged. Rounded, closed pores were observed in the outer corrosion product region.

To confirm that the compositions of the foil in this study matched that of the sections previously reported [28], SEM-EDS line scan results for Mg, O, C, Cl, P, and Ca are shown in Figure 3.11. The corresponding line along which the profile was acquired is shown as a solid white line in Figure 3.11(A). A profile for S was also acquired, but is not shown here due to a complete lack of S in the sample. Several different regions are observed moving from the beginning to the end of the line scan. The first is metallic magnesium, as evidenced by the intense ($> 10^4$ counts) magnesium signal. Moving down the line, the Mg signal decreased in intensity (to about 5×10^3 counts) and O increased ($> 2\times10^3$ counts) were observed in addition to lower-intensity C and Cl signals (~900 and ~700 counts, respectively) that presumably arose from epoxy infiltration. It should be noted that this evidence of epoxy infiltration was only observed in the lower part of the sample,

quite far away from the Figure 3.11(B) field of view and the region in which TEM analysis was conducted.

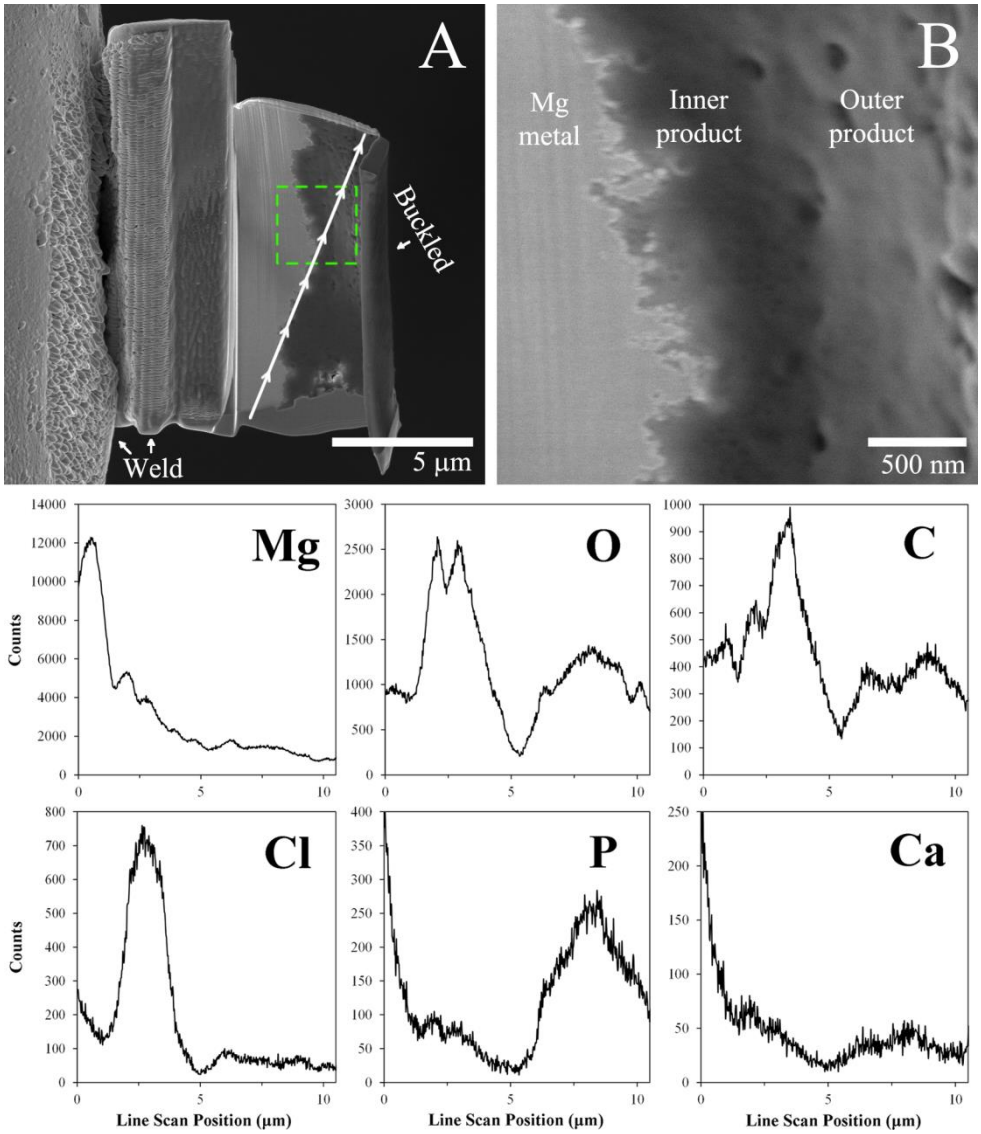

Figure 3.11 – FE-SEM secondary electron images of the milled foil at low magnification (A) and higher magnification (B) showing overall shape and fine surface detail, respectively. The dashed line in (A) outlines the field of view in (B). The EDS results for Mg, O, C, Cl, P, and Ca were taken along the solid white line in (A) in the direction indicated by the arrows.

Further down the line Mg (> 10^3 counts), O (> 10^3 counts), P (> 250 counts), and low levels of Ca (~50 counts) were observed. The progression shown in these SEM-EDS data from Mg, to Mg/O with epoxy, and finally to Mg/O/P/Ca was generally consistent with the elemental profile previously reported for this material [28].

3.2.4.2 Bright field imaging

Multiple bright field frames were acquired across the metal-corrosion product interface and stitched to give a more complete picture of the various phases present. This stitched image is presented as Figure 2. Three morphologically distinct layers were found. The metallic Mg exhibited shallow surface striations that remained from the FIB milling, but there were few other notable features. The inner Mg-O(-C) corrosion product was identified immediately adjacent to the outer Ca/P product and appeared to be very fine-grained. Variations in corrosion product thickness were observed for the inner corrosion product, anywhere from ~50 to 400 nm in the field of view shown in Figure 3.12. The outer Ca/P corrosion product had a globular morphology when viewed in transmission, with the largest structures measuring up to 400 nm in diameter. The smallest identifiable structures have dimensions comparable to the resolution of this micrograph, ~10 nm. Acquisition of higher-magnification bright field images of the two corrosion product phases was attempted, but failed due to the observation of TEM beam-induced transformations at higher magnification, particularly in the outer corrosion layer.

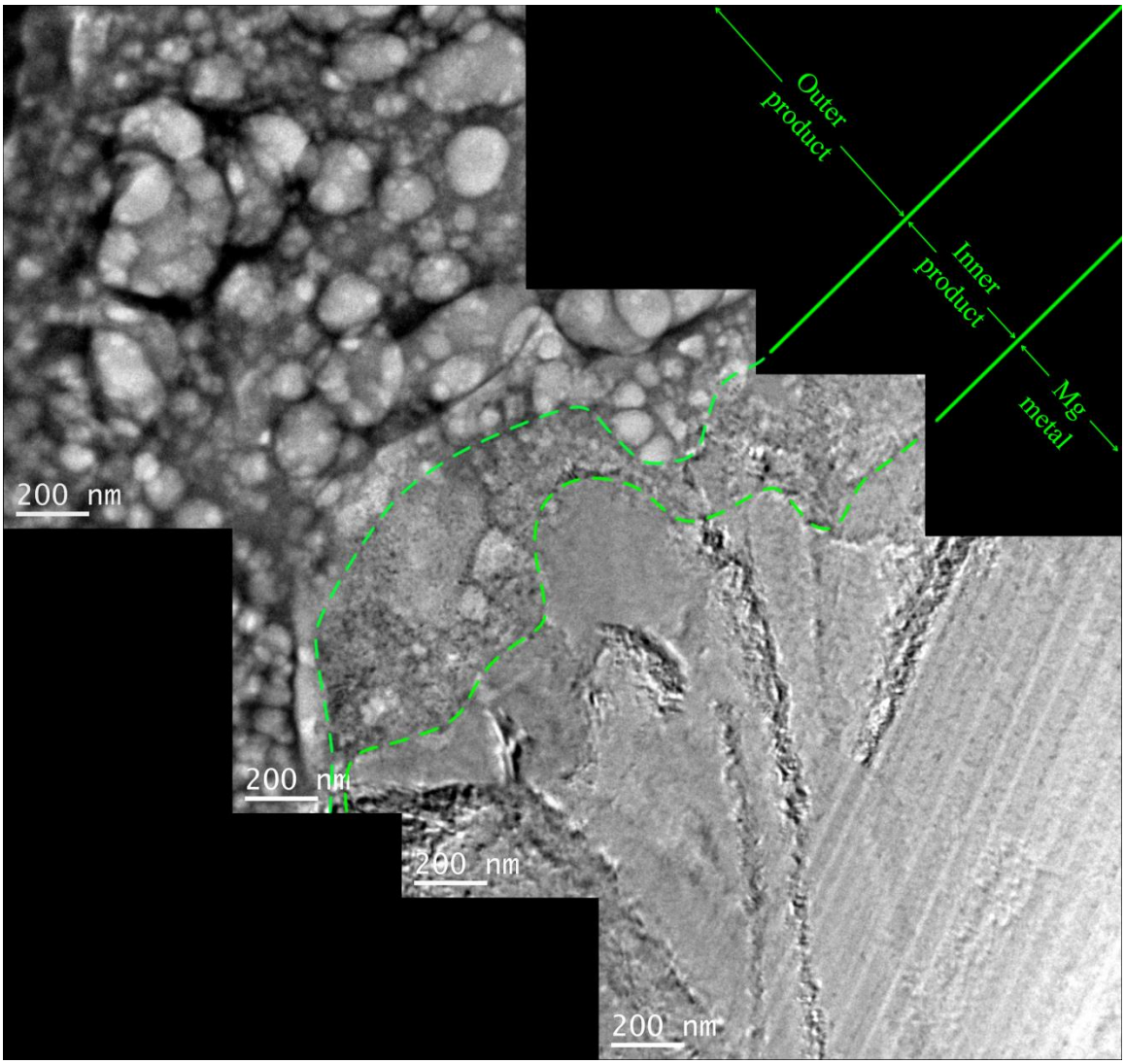

Figure 3.12 – Stitched series of bright field images spanning metallic magnesium, the inner product, and the outer product. Approximate boundaries between the regions are denoted by green dashed lines. The 200 nm scale bar is the same for each stitched frame.

3.2.4.3 SAED and indexing

Several grains of metallic Mg were subjected to SAED analysis until one was identified that lay close to a strongly diffracting pole. The corresponding SAED pattern is presented in Figure 3.13.

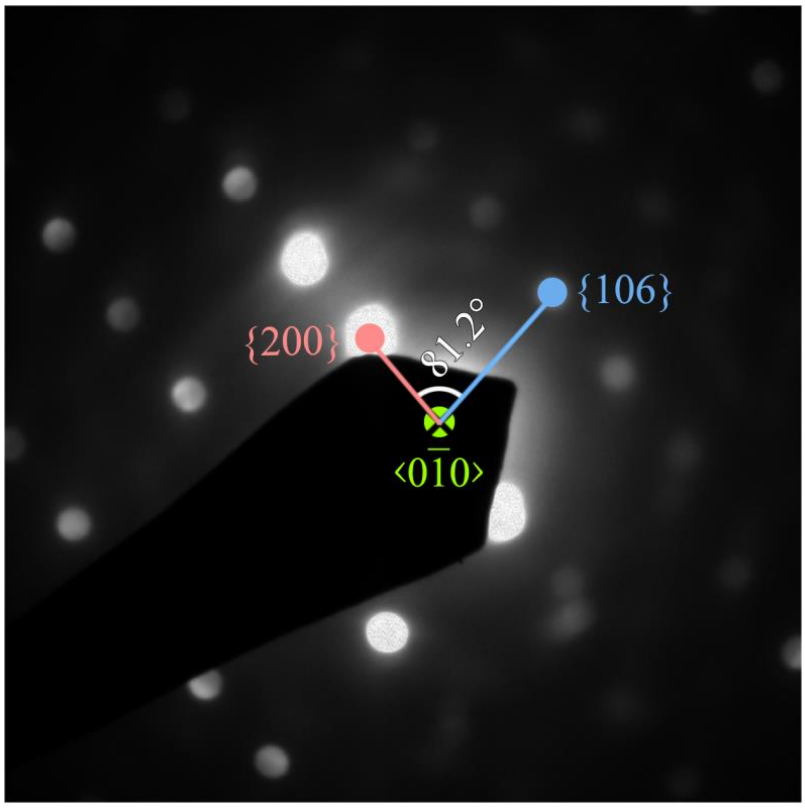

Figure 3.13 – SAED pattern of the metallic Mg along a $\langle 0\bar{1}0 \rangle$ pole.

ImageJ measurements showed that the angular relationship between the two sets of planes was 81.2 ± 0.3°, and the length ratio between the two reciprocal interplanar spacings was 1.69 ± 0.02. These data, together with the constraint that the sum of the two planes had to result in an allowed reflection, were used to search reciprocal space for a matching set of planes. It was determined that the planes belonged to the $\{200\}$ and $\{106\}$ families, which intersect at an angle of 81.4° and have a reciprocal interplanar spacing ratio of 1.677. The observed SAED pattern seems to have originated from near a HCP $\langle 0\bar{1}0 \rangle$ pole and, therefore, from the metallic Mg.

An SAED ring pattern was acquired from a patch of the inner, Mg-O(-C) corrosion product that appeared to be free from both elemental Mg and the outer corrosion product, and is presented in Figure 3.14. The ring pattern is a match to that expected from tabulated diffraction data for MgO (periclase), specifically Joint Center for Powder Diffraction Standards/International Center for Diffraction Data (JCPDS/ICDD) card file number 04-0829.

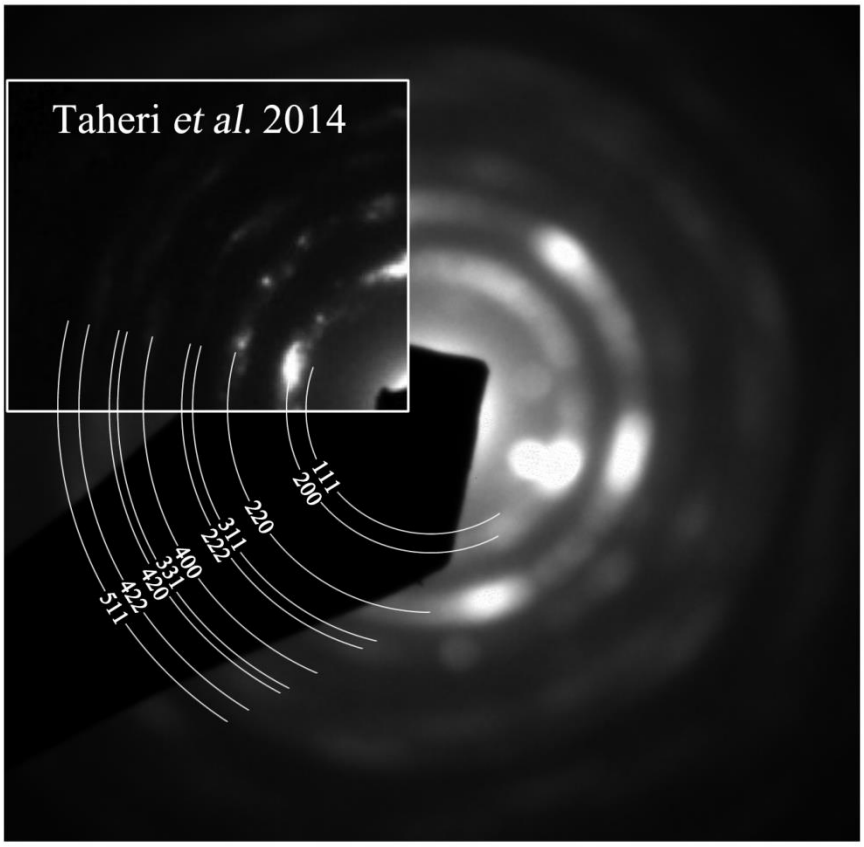

Figure 3.14 – SAED ring pattern from the inner corrosion product with indices shown corresponding to MgO. The inset shows a similar ring pattern from Taheri *et al.* [35].

The {200} and {220} ring structures are the brightest, consistent with the card file data, which specifies relative intensities of 100 and 52, respectively. This pattern is also compared to the ring pattern acquired by Taheri *et al.* (see Figure 3.14 inset) in their study of Mg corrosion in a 0.01 M NaCl solution [35]. The ring spacings and approximate intensities are, again, a match. In SAED patterns from two separate, non-Mg- or Ca/P-containing inner product regions, no extraneous ring structures that could be attributed to $Mg(OH)_2$ or Mg carbonates were observed. This does not necessarily exclude $Mg(OH)_2$ or carbonate from being present in this layer. For instance, the {001} ring structure for $Mg(OH)_2$, if present, may be obscured by the diffuse MgO {111} and {200} rings. However, the lack of other strong diffraction lines (i.e. $Mg(OH)_2$ {011}) does indicate that other species are unlikely to be present in the same quantity as MgO.

The SAED ring pattern for the outer corrosion product is presented in Figure 3.15. This phase was nearly amorphous with only very diffuse diffraction rings present. A contrast-enhanced comparison with the as-acquired image in Figure 3.15 highlights broad, diffuse diffraction rings that reside well away from the transmitted beam. The spacing of the diffuse diffraction rings in Figure 3.15 are compared with X-ray powder diffraction peaks reported by Suchanek *et al.* [36] for heavily substituted Mg/Ca HAp cross-referenced with JCPDS/ICDD card number 09-0432. Ring structures in Figure 3.15 are labeled with the most dominant reflection (i.e. {211} is the strongest member of a series of closely spaced reflections); not all allowed reflections are represented. Many higher-index peaks for Mg/Ca HAp were not readily available.

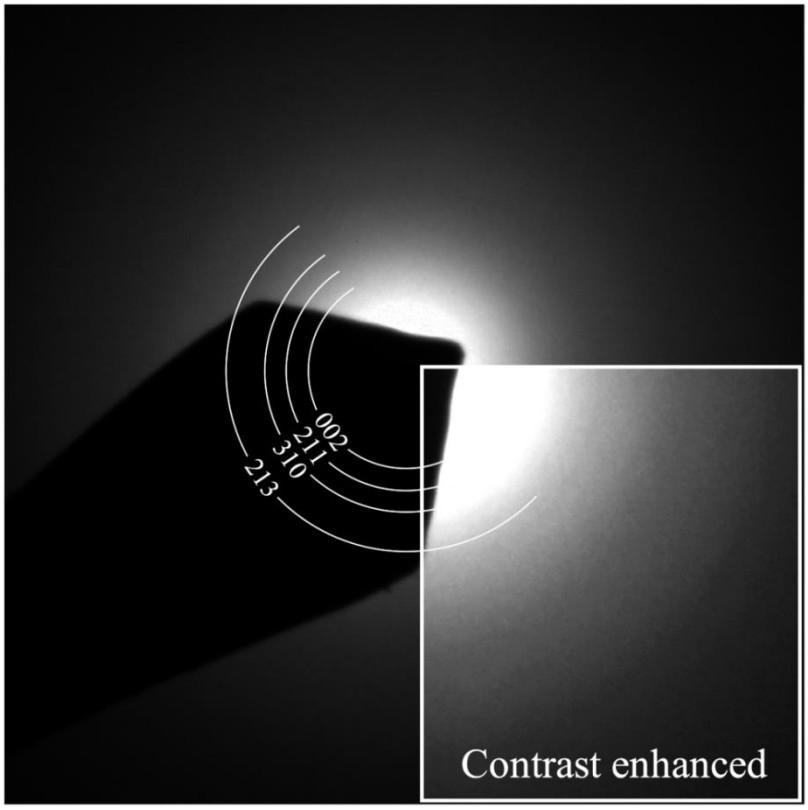

Figure 3.15 – A SAED ring pattern from the outer corrosion product showing poor crystallinity and a diffuse diffraction ring structure. Ring indices correspond to diffraction peaks reported for magnesium-substituted hydroxyapatite [36]. A contrast-enhanced inset is shown to better show some diffuse diffraction ring structures.

3.2.4.4 Dark field imaging

The sample was translated to a location where the inner corrosion product diffracted strongly from a set of basal planes. Using the TEM's objective aperture, the back focal plane was blocked save a single spot on the MgO {200} diffraction ring. This formed a dark field image of one member of the MgO {200} family of planes, which was captured and presented as Figure 3.16. This image contains the same three regions as the bright field image (Figure 3.12). The outer Ca/P corrosion product appears as a diffusely lit

gray area due to the overlap of its diffuse scattering (Figure 3.15) with the aperture-limited area. The metallic Mg appears dark due to a lack of overlap of the Mg and MgO SAED patterns at the chosen location. The diffracting areas comprise elongated structures that extend outward from the Mg metal towards the Ca/P product. The diffracting features in Figure 3.16 measure ~1 nm in width. Their morphology is similar to the MgO layer described by Taheri *et al.* [35].

3.2.5 Discussion

The natures of the outer and inner corrosion product layers agree with previously proposed compositional profiles. No inconsistencies were observed between the nanostructure and crystallography of the Mg/Ca HAp previously proposed [28]. It was noted that Suchanek *et al.* identified $Mg(OH)_2$ formation during mechanochemical–hydrothermal synthesis when Mg^{2+} had displaced > 20% of the Ca^{2+} in the hydroxyapatite structure [36]. However, no crystalline peaks—$Mg(OH)_2$ or otherwise—were observed with SAED for the outer corrosion product in this study. It is likely that hydroxide formation was simply a byproduct of the particular synthesis method used in that work and not a true co-occurring product. The results of Yasukawa *et al.* [37] support this supposition; they managed to synthesize a range of fully crystalline, nearly amorphous, and fully amorphous Mg-containing hydroxyapatites in an aqueous environment without the co-occurrence of $Mg(OH)_2$. The Mg/Ca HAp synthesized by Yasukawa *et al.* became nearly amorphous at approximately 23% Mg^{2+} substitution, and amorphous with ~38% Mg^{2+} substitution. Therefore, the presence of diffuse diffraction

rings in Figure 3.15 suggests that Mg^{2+} has likely replaced somewhere between 23% and 38% of Ca^{2+} ions in the hydroxyapatite structure.

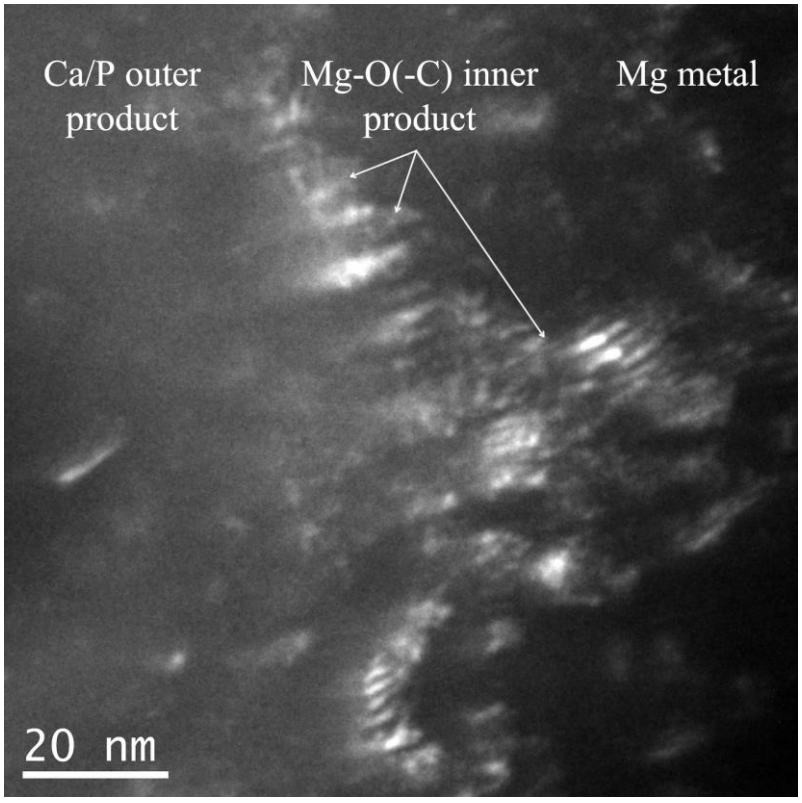

Figure 3.16 – MgO {200} dark field image showing elongated crystallites extending from the metallic magnesium (right) to the Ca/P product (left).

MgO crystallite orientations and their preferred growth directions were critically analyzed through analysis of the SAED pattern shown in Figure 3.14. It is first recognized that most of the ring patterns are diffuse, with low variations in intensity around their circumferences. This implies that the product comprises a multitude of nanoscale crystallites. However, the ring indexed as belonging to the {220} family of planes appears to have large variations in intensity that are regularly spaced. This

suggests that the growth of the crystallites captured in this SAED pattern has a dominant growth direction in plane with the {220} normal vectors. What's more, the crystallites are likely not rotated significantly with respect to one another about their growth axes, as the observed spots are discrete and not heavily broadened. These intensely diffracting {220} spots exhibit six-fold symmetry, indicating that these crystallites are being observed with the beam direction parallel to a $\langle 1\bar{1}1 \rangle$ axis since this is the only axis in the cubic MgO structure that would enable six-fold symmetry of {220} planes. A projection down a $\langle 1\bar{1}1 \rangle$-family axis is shown in Figure 3.17. Two simple growth modes can be proposed from this construction. They correspond to the cases where: (i) a {220} plane normal is parallel to the growth direction, or (ii) a {220} plane normal is misoriented 30° about a $\langle 1\bar{1}1 \rangle$ axis with respect to the growth direction. The first case corresponds to growth that occurs by stacking of {220} planes. The second case would result in both a {220}-family plane normal and a $\langle 1\bar{1}1 \rangle$ vector lying perpendicular to the growth direction, requiring that growth would occur by stacking of the $\{1\bar{1}\bar{2}\}$ family of planes. A continuum of other growth directions is possible; so long as the direction in question lays in-plane with the {220} family normal vectors, and is also normal to a body diagonal. It is not asserted here that all MgO crystallites grow in this manner *in vivo*—the growth direction is likely related to the orientation of the underlying Mg grain—but these results do demonstrate that the inner corrosion product forms as a collection of highly oriented, nanoscale MgO crystallites. It is also consistent with the dark field image (Figure 3.16), which was captured from a different field of view.

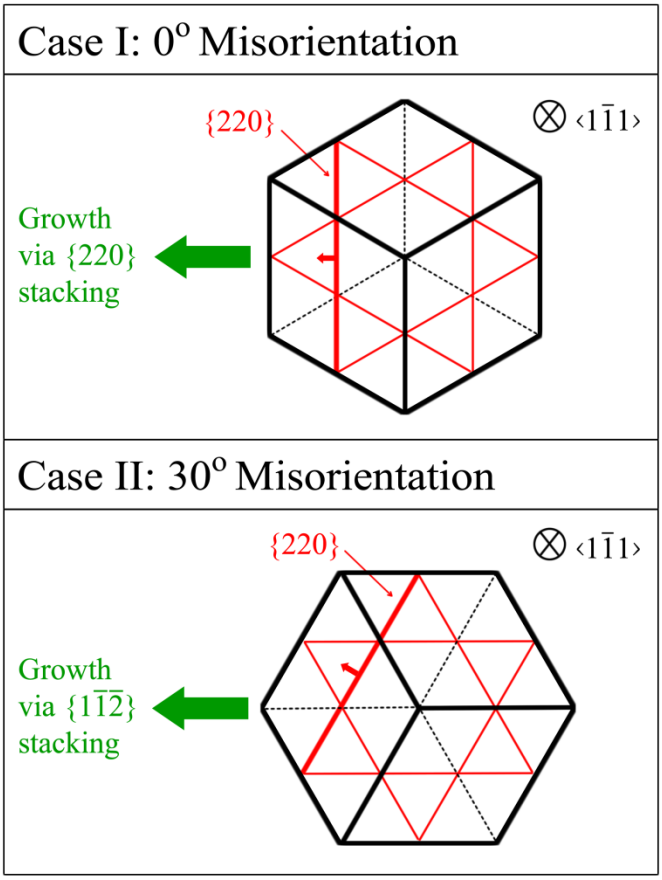

Figure 3.17 – Illustration of two simple MgO growth cases consistent with Figure 4, wherein the MgO {220} family of planes exhibits six-fold symmetry about a ⟨1$\bar{1}$1⟩ axis. The cubic unit cell is drawn in black with hidden edges shown as broken lines, the {220} planes are shown in red, and the growth direction is shown in green.

The apparent dominance of MgO in the inner corrosion product was surprising. Though the presence of MgO in conventional corrosion situations has been previously proven [35, 38], it occurs alongside $Mg(OH)_2$, which is generally considered to be the dominant product. Brady *et al.* [39] demonstrated using TEM analysis that a dense MgO layer underlies a coarse, porous, filamentous $Mg(OH)_2$ layer that was said to grow into the solution adjacent to the corroding implant, and noted that the net corrosion reaction was

reminiscent of high-temperature paralinear oxidation of SiC in a water-bearing atmosphere. OH^- is known to become increasingly prevalent in solution near the metallic interface as acidic groups are consumed in the hydrogen evolution reaction [40]; both the evolution of H_2 and the concomitant increase in pH have been a concern in Mg implant engineering [41]. From this examination of Mg corroded *in vivo*, two explanations present themselves to explain the apparent lack of $Mg(OH)_2$. The first possibility is that hydroxide ions are rapidly sequestered by the body's endogenous buffering mechanisms. It is known that physiological buffering mediated by ammonium, phosphate monobasic, and bicarbonate ions are able to precisely regulate pH [42], a fact that is regularly leveraged in *in vitro* corrosion studies [27]. However, it is not known at what rate these buffering systems may have when reacting to a degrading implant *in vivo*, nor how quickly they may be replenished in the arterial tissue. The second possibility is that the environmental composition itself precludes $Mg(OH)_2$ formation. The chloride anion content of human whole blood is approximately 142 mM [43], likely enough to significantly perturb any $Mg(OH)_2$ film that forms on the Mg surface [44]. Taheri *et al.* [35] reported only a small amount of localized $Mg(OH)_2$ formation in the presence of 10 mM NaCl, so it is reasonable to expect a further retardation of hydroxide reaction in the physiological environment.

The intimate contact between the Mg/Ca HAp and MgO corrosion products in Figure 3.12 implies Mg/Ca HAp forms by direct reaction with the aqueous environment, and that this conversion layer protects MgO from further erosion by the aqueous environment. If there is a lack of perfusion through the compact corrosion layers, then

the mechanism of quasi-steady state corrosion remains an open question. Egress of the metallic Mg appears unlikely, given the absence of voids in the metallic regions in Figure 3.11 and Figure 3.12, as well as in backscattered electron images previously reported [28]. Such voids would remain following the outward migration of Mg/Mg^{2+} from the metallic interface. Given this, solid-state mass transport of oxygen anions to the Mg-MgO interface is suspected to play a role in the growth of MgO and the gradual consumption of metallic Mg. If this is the case, microalloying may be a feasible route to reduce the number of O^{2-} vacancies in the MgO layer [45], and ultimately to "tune" the implant's corrosion rate.

3.2.6 Conclusions

FIB and TEM were used to evaluate the structure of corrosion products that developed on the surface of pure magnesium in the murine artery over the course of 14 days. Three layers were identified: metallic magnesium, an "inner product" consisting primarily of magnesium oxide, and a nearly amorphous "outer product" consistent with magnesium-substituted hydroxyapatite. Neither magnesium hydroxide nor magnesium carbonate was identified. Dark field imaging and selected area electron diffraction analysis indicated that the MgO layer formed as a nanocrystalline phase with a preferred orientation. The magnesium-substituted hydroxyapatite was shown to have a "globular" appearance and was prone to TEM beam damage. Its electron diffraction behavior indicated moderate magnesium substitution in which Mg^{2+} replaced ~23–38% of Ca^{2+} ions in the hydroxyapatite structure.

3.2.7 Acknowledgements

PKB was supported by an American Heart Association predoctoral research fellowship administered by the Midwest Division. The Michigan Initiative for Innovation and Entrepreneurship Technology Commercialization Fund is acknowledged for partial funding of this research. Mick Small from the Applied Chemical and Morphological Analysis Laboratory at Michigan Tech is gratefully acknowledged for his help with conductive coating of SEM specimens.

3.2.8 References

(1) Heublein, B.; Rohde, R.; Kaese, V.; Niemeyer, M.; Hartung, W.; Haverich, A., Biocorrosion of magnesium alloys: a new principle in cardiovascular implant technology? *Heart* **2003,** *89* (6), 651-656.

(2) Mani, G.; Feldman, M. D.; Patel, D.; Agrawal, C. M., Coronary stents: a materials perspective. *Biomaterials* **2007,** *28* (9), 1689-1710.

(3) Moravej, M.; Mantovani, D., Biodegradable metals for cardiovascular stent application: interests and new opportunities. *Int. J. Mol. Sci.* **2011,** *12* (7), 4250-4270.

(4) Zheng, Y. F.; Gu, X. N.; Witte, F., Biodegradable metals. *Mater. Sci. Eng. R* **2014,** *77*, 1-34.

(5) Poncin, P.; Proft, J., Stent tubing: understanding the desired attributes. In *Medical Device Materials: Proceedings of the Materials & Processes for Medical Devices Conference*; Shrivastava, S., Ed.; ASM International: Materials Park, OH, 2004; pp 253-259.

(6) Serruys, P. W.; Chevalier, B.; Dudek, D.; Cequier, A.; Carrié, D.; Iniguez, A.; Dominici, M.; van der Schaaf, R. J.; Haude, M.; Wasungu, L.; Veldhof, S.; Peng, L.; Staehr, P.; Grundeken, M. J.; Ishibashi, Y.; Garcia-Garcia, H. M.; Onuma, Y.,

A bioresorbable everolimus-eluting scaffold versus a metallic everolimus-eluting stent for ischaemic heart disease caused by de-novo native coronary artery lesions (ABSORB II): an interim 1-year analysis of clinical and procedural secondary outcomes from a randomised controlled trial. *Lancet* **2015,** *385* (9962), 43-54.

(7) Di Mario, C.; Caiazzo, G., Biodegradable stents: the golden future of angioplasty? *Lancet* **2015,** *385* (9962), 10-12.

(8) Nishio, S.; Kosuga, K.; Igaki, K.; Okada, M.; Kyo, E.; Tsuji, T.; Takeuchi, E.; Inuzuka, Y.; Takeda, S.; Hata, T.; Takeuchi, Y.; Kawada, Y.; Harita, T.; Seki, J.; Akamatsu, S.; Hasegawa, S.; Bruining, N.; Brugaletta, S.; de Winter, S.; Muramatsu, T.; Onuma, Y.; Serruys, P. W.; Ikeguchi, S., Long-Term (>10 Years) clinical outcomes of first-in-human biodegradable poly-l-lactic acid coronary stents: Igaki-Tamai stents. *Circulation* **2012,** *125* (19), 2343-2353.

(9) Hermawan, H.; Alamdari, H.; Mantovani, D.; Dubé, D., Iron–manganese: new class of metallic degradable biomaterials prepared by powder metallurgy. *Powder Metall.* **2008,** *51* (1), 38-45.

(10) Hermawan, H.; Dube, D.; Mantovani, D., Developments in metallic biodegradable stents. *Acta Biomater.* **2010,** *6* (5), 1693-1697.

(11) Hermawan, H.; Purnama, A.; Dube, D.; Couet, J.; Mantovani, D., Fe-Mn alloys for metallic biodegradable stents: degradation and cell viability studies. *Acta Biomater.* **2010,** *6* (5), 1852-1860.

(12) Hermawan, H., Biodegradable metals for cardiovascular applications. In *Biodegradable metals: from concept to applications*, Springer: Heidelberg, Germany, 2012; pp 23-37.

(13) Bowen, P. K.; Drelich, J.; Goldman, J., Zinc exhibits ideal physiological corrosion behavior for bioabsorbable stents. *Adv. Mater.* **2013,** *25* (18), 2577-82.

(14) Di Mario, C.; Griffiths, H.; Goktekin, O.; Peeters, N.; Verbist, J.; Bosiers, M.; Deloose, K.; Heublein, B.; ROHDE, R.; Kasese, V., Drug-eluting bioabsorbable magnesium stent. *J. Interv. Cardiol.* **2004,** *17* (6), 391-395.

(15) Zartner, P.; Cesnjevar, R.; Singer, H.; Weyand, M., First successful implantation of a biodegradable metal stent into the left pulmonary artery of a preterm baby. *Catheter. Cardiovasc. Interv.* **2005,** *66* (4), 590-594.

(16) Waksman, R.; Pakala, R.; Kuchulakanti, P. K.; Baffour, R.; Hellinga, D.; Seabron, R.; Tio, F. O.; Wittchow, E.; Hartwig, S.; Harder, C.; Rohde, R.; Heublein, B.; Andreae, A.; Waldmann, K. H.; Haverich, A., Safety and efficacy of bioabsorbable magnesium alloy stents in porcine coronary arteries. *Catheter. Cardiovasc. Interv.* **2006,** *68* (4), 607-619.

(17) Pierson, D.; Edick, J.; Tauscher, A.; Pokorney, E.; Bowen, P. K.; Gelbaugh, J.; Stinson, J.; Getty, H.; Lee, C. H.; Drelich, J.; Goldman, J., A simplified *in vivo* approach for evaluating the bioabsorbable behavior of candidate stent materials. *J. Biomed. Mater. Res. B* **2012,** *100B* (1), 58-67.

(18) Waksman, R.; Pakala, R.; Okabe, T.; Hellinga, D.; Chan, R.; Tio, M. O.; Wittchow, E.; Hartwig, S.; Waldmann, K. H.; Harder, C., Efficacy and safety of absorbable metallic stents with adjunct intracoronary beta radiation in porcine coronary arteries. *J. Interv. Cardiol.* **2007,** *20* (5), 367-372.

(19) Slottow, T. L.; Pakala, R.; Okabe, T.; Hellinga, D.; Lovec, R. J.; Tio, F. O.; Bui, A. B.; Waksman, R., Optical coherence tomography and intravascular ultrasound imaging of bioabsorbable magnesium stent degradation in porcine coronary arteries. *Cardiovasc. Revasc. Med.* **2008,** *9* (4), 248-254.

(20) Maeng, M.; Jensen, L. O.; Falk, E.; Andersen, H. R.; Thuesen, L., Negative vascular remodelling after implantation of bioabsorbable magnesium alloy stents in porcine coronary arteries: a randomised comparison with bare-metal and sirolimus-eluting stents. *Heart* **2009,** *95* (3), 241-246.

(21) Wittchow, E.; Adden, N.; Riedmuller, J.; Savard, C.; Waksman, R.; Braune, M., Bioresorbable drug-eluting magnesium-alloy scaffold: design and feasibility in a porcine coronary model. *EuroIntervention.* **2013,** *8* (12), 1441-1450.

(22) Erne, P.; Schier, M.; Resink, T. J., The road to bioabsorbable stents: reaching clinical reality? *Cardiovasc. Intervent. Radiol.* **2006,** *29* (1), 11-16.

(23) Erbel, R.; Di Mario, C.; Bartunek, J.; Bonnier, J.; de Bruyne, B.; Eberli, F. R.; Erne, P.; Haude, M.; Heublein, B.; Horrigan, M.; Ilsley, C.; Bose, D.; Koolen, J.; Luscher, T. F.; Weissman, N.; Waksman, R., Temporary scaffolding of coronary arteries with bioabsorbable magnesium stents: a prospective, non-randomised multicentre trial. *Lancet* **2007,** *369* (9576), 1869-1875.

(24) Waksman, R.; Erbel, R.; Di Mario, C.; Bartunek, J.; de Bruyne, B.; Eberli, F. R.; Erne, P.; Haude, M.; Horrigan, M.; Ilsley, C.; Bose, D.; Bonnier, H.; Koolen, J.; Luscher, T. F.; Weissman, N. J., Early- and long-term intravascular ultrasound and angiographic findings after bioabsorbable magnesium stent implantation in human coronary arteries. *JACC Cardiovasc. Interv.* **2009,** *2* (4), 312-320.

(25) Li, N.; Zheng, Y., Novel magnesium alloys developed for biomedical application: A review. *J. Mat. Sci. Technol.* **2013,** *29* (6), 489-502.

(26) Hornberger, H.; Virtanen, S.; Boccaccini, A. R., Biomedical coatings on magnesium alloys–a review. *Acta Biomater.* **2012,** *8* (7), 2442-2455.

(27) Kirkland, N. T.; Birbilis, N.; Staiger, M. P., Assessing the corrosion of biodegradable magnesium implants: a critical review of current methodologies and their limitations. *Acta Biomater.* **2012,** *8* (3), 925-936.

(28) Bowen, P. K.; Drelich, J.; Goldman, J., Magnesium in the murine artery: Probing the products of corrosion. *Acta Biomater.* **2014,** *10* (3), 1475-1483.

(29) Bowen, P. K.; Drelich, A.; Drelich, J.; Goldman, J., Rates of *in vivo* (arterial) and *in vitro* biocorrosion for pure magnesium. *J. Biomed. Mater. Res. A* **2015,** *103* (1), 341-349.

(30) Yasukawa, A.; Yokoyama, T.; Kandori, K.; Ishikawa, T., Ion-exchange property and mechanism of magnesium–calcium hydroxyapatite solid solutions. *Colloid Surface A* **2004,** *238* (1-3), 133-139.

(31) Giannuzzi, L. A.; Drown, J. L.; Brown, S. R.; Irwin, R. B.; Stevie, F. A., Focused ion beam milling and micromanipulation lift-out for site specific cross-section TEM specimen preparation. *Mater. Res. Soc. Symp. Proc.* **1997,** *480*, 285-290.

(32) Giannuzzi, L. A.; Drown, J. L.; Brown, S. R.; Irwin, R. B.; Stevie, F. A., Applications of the FIB lift-out technique for TEM specimen preparation. *Microsc. Res. Tech.* **1998,** *41* (4), 285-290.

(33) Kamino, T.; Yaguchi, T.; Hashimoto, T.; Ohnishi, T.; Umemura, K., A FIB micro-sampling technique and a site specific TEM specimen preparation method. In *Introduciton to Focused Ion Beams: Instrumentation, Theory, Techniques and Practice*, Giannuzzi, L. A.; Stevie, F. A., Eds.; Springer: New York, 2004; pp 229-245.

(34) Rasband, W. S. ImageJ. http://imagej.nih.gov/ij/.

(35) Taheri, M.; Kish, J. R.; Birbilis, N.; Danaie, M.; McNally, E. A.; McDermid, J. R., Towards a physical description for the origin of enhanced catalytic activity of corroding magnesium surfaces. *Electrochim. Acta* **2014,** *116*, 396-403.

(36) Suchanek, W. L.; Byrappa, K.; Shuk, P.; Riman, R. E.; Janas, V. F.; TenHuisen, K. S., Preparation of magnesium-substituted hydroxyapatite powders by the mechanochemical-hydrothermal method. *Biomaterials* **2004,** *25* (19), 4647-4657.

(37) Yasukawa, A.; Ouchi, S.; Kandori, K.; Ishikawa, T., Preparation and characterization of magnesium-calcium hydroxyapatites. *J. Mater. Chem.* **1996,** *6* (8), 1401-1405.

(38) Song, G.; Atrens, A., Corrosion mechanisms of magnesium alloys. *Adv. Eng. Mater.* **1999,** *1* (1), 11-33.

(39) Brady, M. P.; Rother, G.; Anovitz, L. M.; Littrell, K. C.; Unocic, K. A.; Elsentriecy, H. H.; Song, G. L.; Thomson, J. K.; Gallego, N. C.; Davis, B., Film Breakdown and Nano-Porous Mg(OH)2 Formation from Corrosion of Magnesium Alloys in Salt Solutions. *J. Electrochem. Soc.* **2015,** *162* (4), C140-C149.

(40) Makar, G. L.; Kruger, J., Corrosion of magnesium. *Int. Mater. Rev.* **1993,** *38* (3), 138-153.

(41) Song, G., Control of biodegradation of biocompatable magnesium alloys. *Corros. Sci.* **2007,** *49* (4), 1696-1701.

(42) *Anatomy & Physiology*. OpenStax College: Houston, TX, 2013.

(43) Black, J. *Biological Performance of Materials: Fundamentals of Biocompatibility*. 3rd ed.; Marcel Dekker: New York, 1999.

(44) Tunold, R.; Holtan, H.; Berge, M.-B. H.; Lasson, A.; Steen-Hansen, R., The corrosion of magnesium in aqueous solution containing chloride ions. *Corros. Sci.* **1977,** *17*, 353-365.

(45) Barsoum, M. W. *Fundamentals of Ceramics*. Taylor & Francis: New York, 2002.

Final Remarks

In this dissertation, data and analysis were presented related to the techniques used to evaluate, the kinetics of, and the mechanisms governing magnesium biocorrosion in model arterial environments. Both *in vivo* and *in vitro* techniques accessible to other researchers were emphasized in this work, which increases its potential impact and reach in industry and academia. It is hoped that the results presented in this dissertation will be utilized by researchers to intelligently design and evaluate magnesium alloys and processes.

Discussion and conclusions within individual parts of this dissertation have described the interconnectivity of the analysis methods, kinetic relationships, and the interpretation of degradation within the mechanistic framework presented. However, there are two overarching lessons from this work that merit mentioning, and not been explicitly stated previously in this work.

The first key takeaway is that magnesium biocorrosion is not informed entirely by experiences with automotive or maritime degradation. The inappropriate cross application of "conventional" (based on NaCl immersion or salt spray; non-pseudophysiological) corrosion mechanisms resulted in the widely held expectation that magnesium hydroxide played a major role in magnesium biocorrosion. In fact, the "inner corrosion product" examined in this dissertation by transmission electron microscopy appeared to comprise almost entirely magnesium oxide—not hydroxide. This outcome

draws into question other expectations that are based on conventional corrosion experiments—for instance, hard tolerance limits for iron, copper, and nickel cathodic impurities and microgalvanically-mediated corrosion initiation. These legacy assumptions should not be accepted uncritically; it must be confirmed that they still apply to *in vivo* biocorrosion.

A common ambition of *in vitro* method development is to reproduce the rate of *in vivo* biocorrosion on the benchtop. This is not realistic. In the view of the author, an *in vitro* model may be considered successful if the corrosion mechanism— mode/pattern of corrosion initiation, composition of products, rate-limiting aspects, failure conditions, etc.—are reproduced to a reasonable degree outside an animal. (Note that this necessitates *a priori* knowledge of the *in vivo* corrosion mechanism to which the *in vitro* model may be matched.) More often than not, researchers conflate kinetics, referring to corrosion rate, with thermodynamics, referring to mechanism. This work has shown that it is possible to reconcile kinetic differences *in vivo* and *in vitro* through development of a multiplier instead of through method development.